# Exploring the Remote Linkage of Tropical Variability to Polar Cold Air Mass and Cold Air Outbreak

PhD Thesis

# Exploring the Remote Linkage of Tropical Variability to Polar Cold Air Mass and Cold Air Outbreak

# 極域寒気および寒気流出と熱帯変動の遠隔連関に関する探究

Muhammad Rais Abdillah
(ムハンマド・ライス・アブディラー)

Department of Geophysics
Graduate School of Science
Tohoku University
September, 2018

PhD Thesis

# Exploring the Remote Linkage of Tropical Variability to Polar Cold Air Mass and Cold Air Outbreak

Muhammad Rais Abdillah

Department of Geophysics
Graduate School of Science
Tohoku University

Thesis Committee Members

Professor Takeshi Yamazaki (Chair, Supervisor)
Professor Tadahiro Hayasaka
Professor Shinji Morimoto
Associate Professor Hironobu Iwabuchi
Research Professor Toshiki Iwasaki

2018

博士論文

# 極域寒気および寒気流出と熱帯変動の遠隔連関に関する探究

東北大学大学院理学研究科
地球物理学専攻

ムハンマド・ライス・アブディラー

論文審査委員

| | |
|---|---|
| 山崎　剛 | 教授（指導教員・主査） |
| 早坂　忠裕 | 教 授 |
| 森本　真司 | 教 授 |
| 岩渕　弘信 | 准教授 |
| 岩崎　俊樹 | 特任教授 |

平成 30 年

# Abstract

Polar cold air mass (PCAM) builds up in winter and serves as an important climate component of Earth's lower troposphere in the extratropical regions. PCAM resides in polar cap and expands to midlatitudes. Under the influences of extratropical waves, PCAM occasionally releases cold air from high latitudes to lower latitudes. This outflow of PCAM is referred to as cold air outbreak (CAO) phenomenon. CAO transports cold air mass and affects heat, energy, and momentum balances of the atmosphere and can interact with ocean. CAOs can cause severe cold waves that are responsible for extreme cold events and snowstorms, which are harmful for society. Furthermore, CAOs sometimes penetrate deep into tropical regions. The strengthening of equatorward flow enhances moisture influx and potentially triggers some disturbances in the tropics. Therefore, PCAM and CAO are of great importance for weather and climate in both extratropics and tropics. On the other hand, large-scale organized convections over the tropics can influence extratropical atmosphere. Some major tropical phenomena, such as El Niño-Southern Oscillation (ENSO) and Madden-Julian Oscillation (MJO), are widely known to excite poleward-propagating planetary wave train that affects the extratropics. These tropical forcing may control the variability of PCAM/CAO. This thesis aims to identify and examine any interactions between the tropical variability and PCAM/CAO. The definitions of PCAM and CAO are based on a threshold potential temperature of 280 K. The use of isentropic coordinate allows us to perform objective and quantitative diagnosis of PCAM. The main results are shown in Chapters 3, 4, 5, and 6. Chapters 3 to 5 document the influences of tropical forcing on PCAM/CAO. Chapter 6 documents the impact of East Asian CAO on tropical disturbances.

Chapter 3 investigates the relationship between ENSO and PCAM in the Northern Hemisphere. We find that ENSO strongly controls interannual variability of total hemispheric PCAM amount. The correlation coefficient between PCAM and Nino-3.4 sea surface temperature (SST) index reaches -0.66. During El Niño, the total PCAM amount decreases significantly. This reduction is largely attributed to the decrease in residence time of PCAM. The residence time can be interpreted as the average time that is taken by high latitudes PCAM to outflow into low latitudes. The shorter residence time consequently indicates stronger cold air outbreak and increases some PCAM amount over midlatitudes. However, the outbreak of cold air is situated over the warm ocean of central North Pacific. The warm surface hinders PCAM development over midlatitude and therefore causes imbalance in total hemispheric PCAM amount. The anomalous PCAM circulation is driven by enhanced Aleutian Low associated with ENSO-induced Pacific/North American teleconnection pattern. This result reveals a robust impact of ENSO on polar region.

Chapter 4 examines the relationship between CAOs in East Asia and ENSO. We first discuss the interannual variability of East Asian cold air stream. An EOF analysis shows two interesting

leading modes of equatorward stream in East Asia. They are named as western CAO and eastern CAO. The separation between western and eastern types of CAOs reveals relative roles of extratropical forcing of Siberian High and Aleutian Low on development of equatorward cold air stream in East Asia. Interestingly, the two CAOs show opposite dipole pattern of tropical precipitation over the Maritime Continent and central Pacific. SST anomalies show cooling (western CAO) and warming (eastern CAO) over the eastern Pacific, suggesting the possible roles of ENSO. ENSO influences the East Asian CAOs by modulating tropical convection over the Maritime Continent and central Pacific associated with changes in zonal Walker Circulation. The convection anomalies excite poleward Rossby wave train and affect PCAM fluxes. This mechanism is then clarified by performing numerical experiments using a linearized global climate model (GCM). This chapter signifies the importance of ENSO on East Asian winter.

Chapter 5 explores the tropical influence on intraseasonal time scale. We show that some eastward-moving large-scale convergences appear accompanying the course of CAO evolution. It suggests the possible role of MJO. Observational analysis using MJO indices reveals the active roles of wave train on CAO evolution. The intraseasonal component of western CAO is preceded by wet MJO over the Maritime Continent, and the eastern CAO is induced by wet MJO over the western Pacific and dry MJO over the Indian Ocean. We also find that MJO affects the mean occurrences of short-term/synoptic-scale CAOs. We conducted some sensitivity experiments using GCM to investigate the mechanism in details.

Chapter 6 finally assesses the potential impact of extratropical CAO on tropical weather. The western CAO is typically strong and can penetrate into low latitudes. The result shown by regression analysis clarifies the appearance of significant signal of precipitation following the western CAO. However, the mean response seems weaker and more limited in region compared with previous studies on subtropical cold surges. We then explore the impact by investigating each individual CAO cases and find significant inhomogeneity among the cases, motivating us to perform some clustering analyses. We cluster CAOs that developed to northerly surge (CAO(NS)) and that developed to westerly surge (CAO(WS)). CAO(NS) clearly shows strong precipitation response while CAO(WS) does not show active precipitation response. Furthermore, the pathways of CAO(NS) in the subtropics can vary depending on the pre-existing synoptic conditions over the tropical regions. We identify four additional subtropical CAO(NS) pathways that produce different precipitation patterns. This result suggests us to add more criteria for monitoring CAO in addition to the magnitude of CAO index.

The results of this study improve our understanding on remote interactions between the tropics and the extratropics. The findings on MJO and ENSO influences on CAOs help to improve mid- and long-range forecasts of PCAM/CAO in the extratropics. On the other hand, the impact of CAO is crucial for weather forecasters over the tropical regions.

# Table of contents

# List of Figures

# List of Tables

# Acknowledgements

This thesis would not be finished without contributions from many parties. I would like to sincerely thank Prof. Toshiki Iwasaki (now retired) for his continuous patient, guidance, and encouragement since I started my study in Tohoku University in 2013. Through constructive discussions with him, I have gradually gained a better understanding on the atmospheric dynamics and how to conduct a good research. I would also like to sincerely thank Prof. Takeshi Yamazaki who always encourages and gives meaningful advices during the seminars and thesis consultations. I express many thanks to Dr. Yuki Kanno for being my best collaborator in the lab. He gave me a lot of inspirations and solved many problems while conducting the research. Invaluable supports were also given by other members of Atmospheric Science Laboratory. Dr. Guixing Chen, Dr. Ryuhei Yoshida, Prof. Weiming Sha, and Dr. Takahiro Sasai gave helpful advices to my study. Mr. Takamichi Shoji taught me how to construct lagged analysis of cold air outbreak. Dr. Indira Kadel always encouraged and gave meaningful suggestions. Dr. Shin Fukui, Mr. Kenji Aono, and other PC staffs helped me with computational problems. Mrs. Saeko Hasebe assisted me with my paperwork. A lot of thanks are given to Dr. Gonzalo Leonardini, Dr. Rochelle C. Coronel, Ms. Irina Melnikova, Ms. Madam Taqiyya, Mr. Terry Atalifo, and other former/current lab mates for their kind helps in many ways.

I am very grateful to many researchers: Dr. R. Kartika Lestari, Dr. Koutarou Takaya, Dr. Lin Wang, Dr. N. H. Saji, Dr. S.-P. Xie, Dr. Akira Yamazaki, Dr. N. J. Trilaksono, Dr. Jun Matsumoto, and other people that I met during their visits to Tohoku University or during international conferences. Suggestions from them were very helpful and excited a lot of insights. I am also thankful to Prof. Toshio Suga of Physical Oceanography Laboratory who taught me ocean dynamics that is helpful for ENSO research. I would like to thank IGPAS 2013 program committee and MEXT scholarship, which allowed me to pursue a higher education in Tohoku University. Many sincere thanks are expressed to my wife Nurfiena Sagita Putri who often helped me with ideas and English editing. Finally, I am very thankful to my family in Indonesia for their continuous supports.

In this thesis, I write the active subject of the author as “we” instead of “I” to highlight the invaluable contributions from the others.

# 1. General introduction

## 1.1 **Background**

Polar cold air mass (PCAM) appears largely in winter and serves as an important climate component of Earth's lower troposphere over the extratropics. The coverage of PCAM expands to midlatitudes, which in turn creates strong meridional temperature gradient over there. The temperature gradient forms baroclinic instability that is a major source of extratropical weather systems. PCAM is accumulated over the polar cap by radiative cooling. The built-up PCAM over high latitudes is intermittently transferred to middle and low latitudes by extratropical waves. This equatorward outflow of PCAM is often referred to as cold air outbreak (CAO) phenomenon. CAO significantly affects heat, energy, and momentum balances of the atmosphere and interacts with ocean (Mailler and Lott 2010; Garreaud 2001; Shoji et al. 2014). CAOs can excite severe cold waves that are responsible for extreme cold events and snowstorms, which are harmful for society (Cellitti et al. 2006). For example, in late January 2016, an extreme CAO event occurred in East Asia and caused a lot of damage (Figure 1.1), where at least 95 people died across East Asian and Southeast Asian countries (Holmes 2016). Furthermore, CAOs sometimes release equatorward flow that penetrates deep into tropical regions (Compo et al. 1999). The equatorward flow enhances moisture influx and triggers some disturbances, which can lead to several rainfall and flood events over the tropics (Tangang et al. 2008; Trilaksono et al. 2012; Lim et al. 2017). Considering their large roles and vast influences, PCAM and CAO are of great importance for weather and climate variability in both the extratropical and the tropical regions

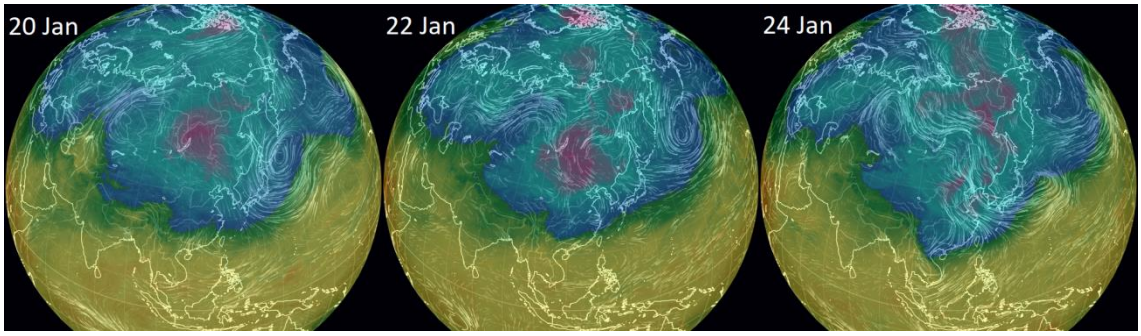


Figure 1.1 A sequence of daily weather patterns showing an extreme cold air outbreak (CAO) event occurred in late January 2016. From left to right: low-level atmospheric temperatures and circulation on 20, 22, and 24 January. Purple-blue colors denote cold areas. White contours denote low-level air flow (modified from Beccario (2018)).

The majority of studies utilize temperature and/or meridional wind at certain pressure levels to estimate the intensity of CAO. However, this approach raises questions about the accuracy because the mass of polar cold air is not explicitly incorporated. The use of parameters based on pressure levels, however, may include both warm and cold air fluxes. To avoid this problem, a recent study proposed a diagnosis method by using isentropic analysis (Iwasaki et al. 2014). It is conducted on the basis of potential temperature coordinates. Potential temperature indicates the temperature of an air parcel would have if the parcel is forcedly brought adiabatically to the reference level of 1000 hPa. Below a constant potential temperature surface, the hemispheric amount of PCAM is conserved under adiabatic conditions. Therefore, by designing a potential temperature threshold, isentropic analysis enables expressions of PCAM and CAO in an objective and quantitative way. Several studies have used this approach to document the climatology and variability of PCAM and CAO (Shoji et al. 2014; Kanno et al. 2015a,b; Kanno et al. 2016, 2017). Nevertheless, the impact of isentropic CAO on the tropical weather variability has not been investigated yet.

Tropical region is warmer than the polar region owing to the incoming energy from the sun. The equatorial belt exhibits a primary region of atmospheric convections as the response to large-scale low level convergence over the tropics. The moist convections release abundant latent heat and drive meridional overturning circulations, which distribute the excess of heat, energy, and momentum from the tropics to the extratropics (Lorenz 1967). The remote influence from the tropics is basically controlled by the intensity of zonal-mean meridional circulations. In a closer look, the tropical convections have strong regional variability due to the distribution of continents and oceans. The inhomogeneity of the Earth's surface causes "localized" convections over particular areas, which in turn affects the distribution of meridional direct cells and creates zonal Walker cells (Saha 2010). For example, the Maritime Continent and western Pacific exhibit more active convections relative to the Indian Ocean and eastern Pacific because of the "warm pool" over the western Pacific. This condition leads to strong Hadley circulation over East Asia and development of Walker circulation over the Pacific.

Furthermore, the variability of localized convections affects planetary waves over the tropics and the extratropics, which can disrupt weather and climate variability around the world. Two major tropical phenomena that significantly control the distribution of tropical convections are El Niño-Southern Oscillation (ENSO) (Walker and Bliss 1932; Bjerknes 1969; Trenberth et al. 1998) and Madden-Julian Oscillation (MJO) (Madden and Julian 1971; Wheeler and Hendon 2004). ENSO occurs at multi-annual time scale and is basically indicated by sea surface temperature fluctuations over the equatorial Pacific. Two typical ENSO phases, El Nino and La

Nina, strongly modulate precipitation anomalies over the Maritime Continent and the central Pacific. A well-known El Niño impact is shown in Figure 1.2. The surface ocean warming over the eastern Pacific associated with El Niño causes more rainfall over the central Pacific and triggers poleward stationary wave train approaching North America and Europe (Horel and Wallace 1981; Trenberth et al. 1998; Brönnimann 2007). On different time scale, MJO is one of the largest sources of tropical intraseasonal variability. It is often characterized by eastward propagating convection anomalies over the Indo-Pacific. The migration of MJO exerts wave trains that have impacts on weather variability over many areas of the tropics and the extratropics (Lin et al. 2010; Barrett et al. 2015; Vitart and Molteni 2010; Matthews et al. 2004). Although some studies have been done on the impact of ENSO and MJO, there is no study that specifically discusses the impacts on the frameworks of PCAM and CAO.


Figure 1.2 Schematic upper-tropospheric circulation anomalies during El Nino. Hatched region over the equator indicates active precipitation area. H and L symbols denote high and low pressure centers (modified from Horel and Wallace 1981).

## 1.2 **Objective of this study**

Previous studies of PCAM and CAO mainly discussed their climatology and basic variability. Here, the current study aims to identify and examine the possible relationships of PCAM and CAO to tropical climate and weather variability. We explore two-ways interactions between the tropics and the extratropics. On one way, the influences of ENSO and MJO to PCAM and CAO are investigated. On the other way, the impact of CAO on tropical weather variability is examined. This thesis consists of seven main chapters. Following the introduction,

Chapter 2 explains the basic frameworks of isentropic PCAM and CAO. This chapter also discusses the theory of atmospheric teleconnection from the tropics. The results are shown in Chapters 3-6. Chapter 3 shows the influence of ENSO on northern hemispheric PCAM. Chapters 4 and 5, respectively, investigate the roles of ENSO and MJO on CAO variability in East Asia. Chapter 6 assesses the impact of CAO on tropical precipitation over the Maritime Continent. Finally, Chapter 7 summarizes the key findings of this study and discusses some potential future works.

# 2. Basic frameworks of polar cold air mass and atmospheric teleconnection

## 2.1 Isentropic analysis of polar cold air mass and cold air outbreak

### 2.1.1 Polar cold air mass in isentropic coordinate

Isentropic analysis allows us to perform objective and quantitative diagnosis of PCAM and CAO. In the viewpoint of mass-weighted general circulation—zonal mean circulation calculated from isentropic surfaces, there is a thermally direct cell located over midlatitude (Figure 2.1). This extratropical direct (ETD) cell simply shows meridional heat transport over the extratropics and depicts the basic framework of PCAM where PCAM grows over high latitudes due to diabatic cooling, outflows equatorward over midlatitudes following the wave-mean flow, and then disappears over low latitudes due to diabatic heating. The center of ETD is located over midlatitude approximately at 45°N and 850 hPa. This location exhibits a turning point of PCAM from downward motion to equatorward motion at midlatitudes. The mass flux beneath this point can be shown as zonal mean cold air outbreak (Iwasaki and Mochizuki 2012).

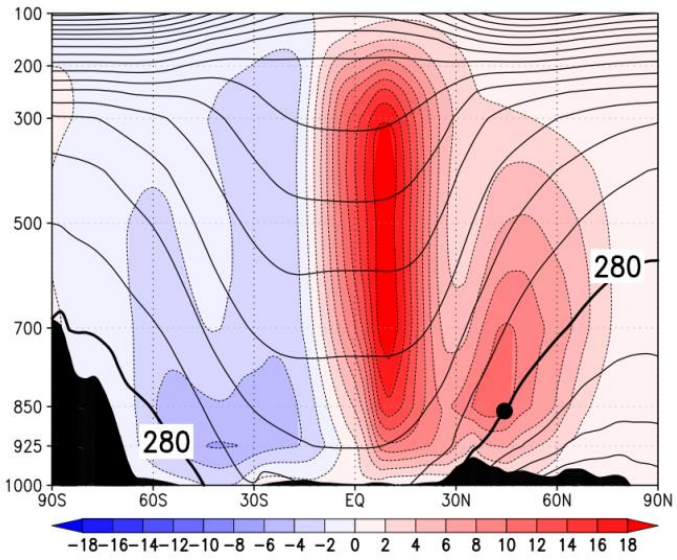


Figure 2.1 Mass-weighted isentropic zonal-mean depicting climatology of mass streamfunctions in boreal winter (DJF 1980/81–2009/10) (contour interval $2\times10^{10}$ kg $s^{-1}$). Red and blue shadings respectively show clockwise and anticlockwise circulation. Black contours indicate potential temperatures (contour interval 10 K). The black dot is at (45°N, 850 hPa) overlapped with 280 K (thick black contour). Black shadings indicate the zonally averaged topography (modified from Iwasaki et al. 2014).

A spatial diagnosis is critically needed because the actual geographical distributions of PCAM and its flux are greatly influenced by topography and land-sea thermal contrasts. To quantify PCAM amount at each grid point, we need a threshold potential temperature. Below a constant potential temperature surface, the hemispheric PCAM is conserved under adiabatic condition. What is the most appropriate threshold for PCAM/CAO diagnosis? This study uses 280 K as the main threshold. The reason is that the 280 K level appears to overlap with the turning point of ETD cell in Figure 2.1, suggesting the best threshold for delineating geographical PCAM that develops into CAO based on the thermodynamical sense of zonal-mean circulation. Using 280 K as a designated threshold, Iwasaki et al. (2014) formulated PCAM as followings. PCAM amount at each grid point ($DP$) is defined as the difference between pressure at the Earth's surface ($p_s$) and pressure at a threshold potential temperature surface $\left( p(\theta_T) \right)$, so that

$$DP \equiv p_s - p(\theta_T). \tag{2.1}$$

The tendency of $DP$ is controlled by the convergence of horizontal PCAM flux, $\mathbf{F}$, and the diabatic genesis/loss rate of PCAM, noted as $G(\theta_T)$,

$$\frac{\partial}{\partial t} DP = -\boldsymbol{\nabla} \cdot \mathbf{F} + G(\theta_T), \tag{2.2}$$

where $\mathbf{F}$ and $G(\theta_T)$ are respectively defined as

$$\mathbf{F} \equiv \int_{p(\theta_T)}^{p_s} \mathbf{v}\, dp, \tag{2.3}$$

$$G(\theta_T) \equiv \frac{\partial p}{\partial \theta} \dot{\theta} \Big|_{\theta_T}. \tag{2.4}$$

$\mathbf{v}$ denotes horizontal wind vector. $DP$ and $\mathbf{F}$ are directly calculated at each grid point. The tendency of $DP$ is estimated using the 6-hour JRA-55 reanalysis dataset. $G(\theta_T)$ is approximated from the residual of conservation relation in eq. (2.2).

Figure 2.2 shows the climatology of $DP$, $\mathbf{F}$, and $G(\theta_T)$. PCAM largely resides over the Arctic Circle and expands to midlatitudes. The distribution of PCAM flux is strongly influenced by stationary ultra-long waves owing to topography and land-sea thermal contrast. The climatology of PCAM flux reveals two major equatorward cold air streams in boreal winter: 1) East Asian (EA) stream and 2) North American (NA) stream. The former starts as westerly over central Eurasia, turns southeastward over Lake Baikal, and disappears over the Kuroshio Current in the North Pacific. The latter develops over the Arctic Ocean, moves to North America, and disappears over the Gulf Stream in the North Atlantic. These streams denote the

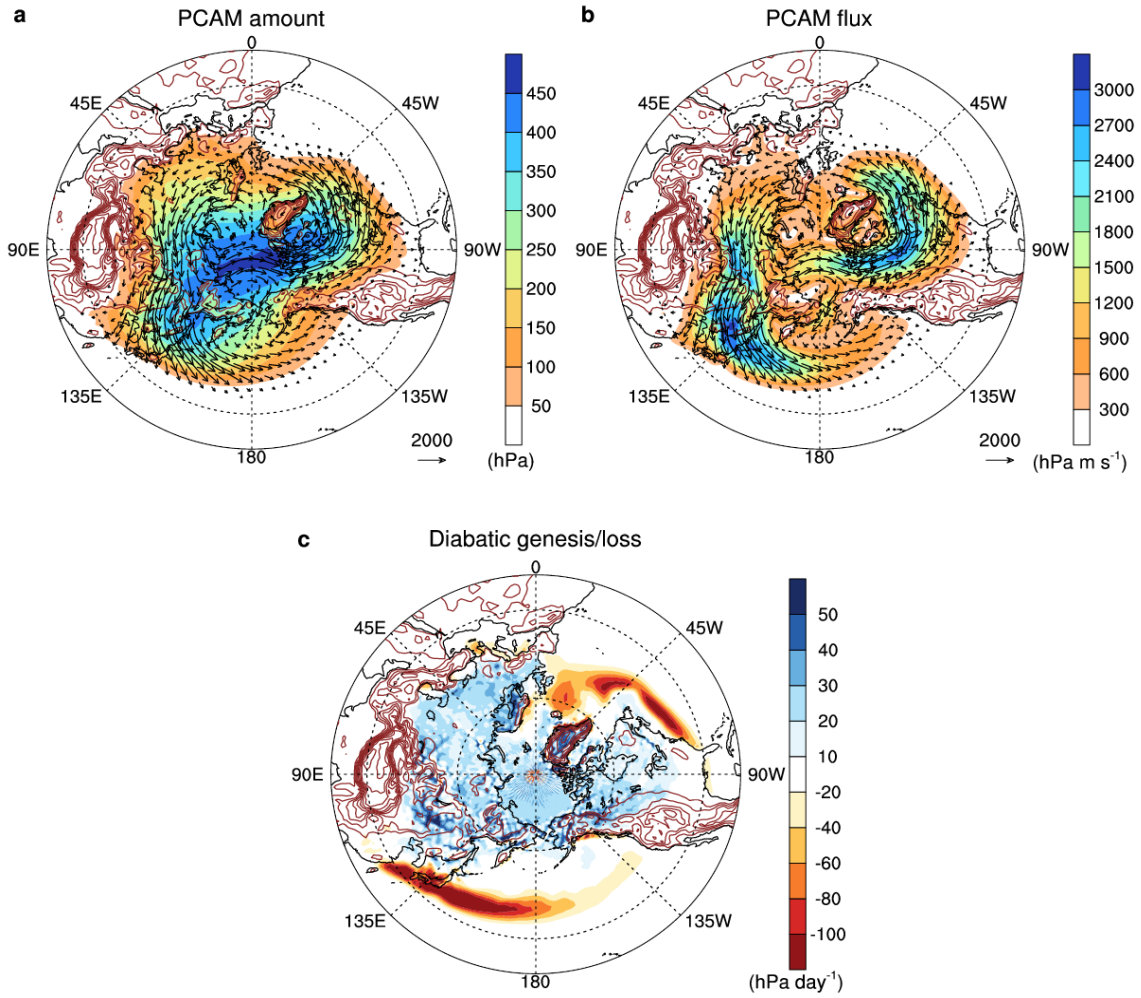


Figure 2.2 Climatology of (a) PCAM amount $DP$, (b) magnitude of PCAM flux $\mathbf{F}$, and (c) PCAM genesis/loss rate $G(\theta_T)$. Arrows in (a) and (b) denote vector field of PCAM flux. Brown contours denote topography (contour interval 500 m). Climate period is DJF 1981/82-2016/17.

primary pathways of intermittent CAO events in the Northern Hemisphere. The exit regions of these streams exhibit large diabatic losses of PCAM indicating the roles of diabatic heating associated with the warm ocean surfaces. The intrusion of PCAM over the ocean causes large heat release from the ocean and affects the ocean current.

### 2.1.2 Zonal-mean two-box model of polar cold air mass

The characteristics of the hemispheric PCAM can be explained by the charge-discharge theory in a zonal-mean two-box model that consists of a genesis box and a loss box (Kanno et al. 2015a) (Figure 2.3a). The genesis box is located at high latitudes where the PCAM is generated due to diabatic cooling (charge). The PCAM then moves equatorward (discharge) following the wave-mean flow interactions (Iwasaki and Mochizuki 2012). Finally, the loss box at low latitudes denotes the location where most of the PCAM disappears due to diabatic

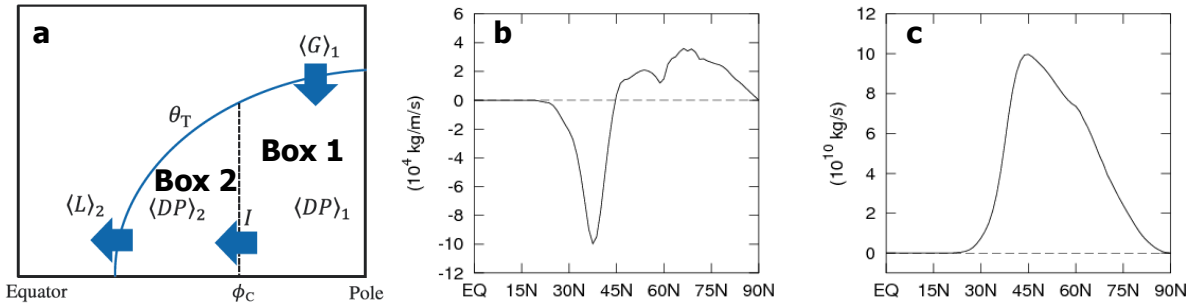


Figure 2.3 (a) Schematic representation of two-box model of hemispheric PCAM (modified from Kanno et al. (2015a)). (b) and (c) show climatology of zonally integrated PCAM genesis/loss rate and equatorward component of PCAM flux, respectively.

heating. The latitudinal boundary between these boxes (i.e., the critical latitude) is set to 45°N because 1) the northern hemispheric PCAM below 280 K tends to be generated north of 45°N and disappear south of 45°N and 2) the maximum intensity of equatorward outflow is located at 45°N (Kanno et al. 2015b) (Figure 2.3b,c).

The conservation rules of the PCAM in the genesis box and loss box are respectively

$$\frac{\partial}{\partial t}\langle DP \rangle_1 = -I + \langle G \rangle_1 \tag{2.5a}$$

and

$$\frac{\partial}{\partial t}\langle DP \rangle_2 = I - \langle L \rangle_2. \tag{2.5b}$$

The angle brackets denote the areal integrations of any variable A, and subscripts 1 and 2 denote integrations over the genesis box (45°-90°N) and loss box (EQ-45°N), respectively. $L$ indicates upward diabatic mass flux at 280 K ($L \equiv -G$). $I$ denotes the zonally integrated southward component of the PCAM flux at 45°N (as an indicator of zonal-mean cold air outflows). Kanno et al. (2015b) introduced two time parameters to represent the time constant of the PCAM in each box,

$$\tau_1 \equiv \frac{\langle DP \rangle_1}{I} \quad \text{and} \quad \tau_2 \equiv \frac{\langle DP \rangle_2}{\langle L \rangle_2}. \tag{2.6}$$

$\tau_1$ and $\tau_2$ are the residence time of the PCAM inside the genesis box and the life time of the PCAM inside the loss box, respectively. Considering a long-term temporal mean and substituting $I$ and $\langle L \rangle_2$ in equation (2.5), it can be shown that $\langle DP \rangle_1 = \tau_1 I \approx \tau_1 \langle G \rangle_1$ and $\langle DP \rangle_2 \approx \tau_2 I$. The sum of $\langle DP \rangle_1$ and $\langle DP \rangle_2$ yields a simple relation among the total hemispheric PCAM amount ($\langle DP \rangle$), the time constants, and the outflow as following

$$\langle DP \rangle \equiv \langle DP \rangle_1 + \langle DP \rangle_2 = (\tau_1 + \tau_2) I. \quad (2.7)$$

Kanno et al. (2015b) compared the climatological feature of PCAM in both winter hemispheres and found significant difference. Total PCAM amount in the Northern Hemisphere is much larger than total PCAM amount in the Southern Hemisphere. They concluded that the larger PCAM amount in the Northern Hemispher is caused by longer $\tau_1$. Huge mountains and distinct land-sea distribution cause the PCAM to stay longer. Another study by Kanno et al. (2015a) have shown the benefit of two-box model in demonstrating charge-discharge theory of PCAM. They explained daily evolution of hemispheric-scale cold air outbreak from its generation to its loss.

### 2.1.3 Cold air outbreaks in East Asia

CAO is basically a synoptic scale phenomenon. The mechanism of CAO is explained by topographically trapped extratropical waves due to large mountains. A schematic figure from Garreaud (2001) shows the major pathways of CAOs, which are located over the east of huge mountainous regions (Figure 2.4). In addition to the significant CAO impacts over the extratropics, CAOs sometimes can penetrate deep into tropical regions and cause tropical disturbances. Therefore, weather forecasters over the tropics also conduct regular monitoring on the CAOs. Nevertheless, most studies of CAO only used proxies such as changes in temperature or equatorward wind. Their CAO definitions may be not accurate and subject to regional dependencies.

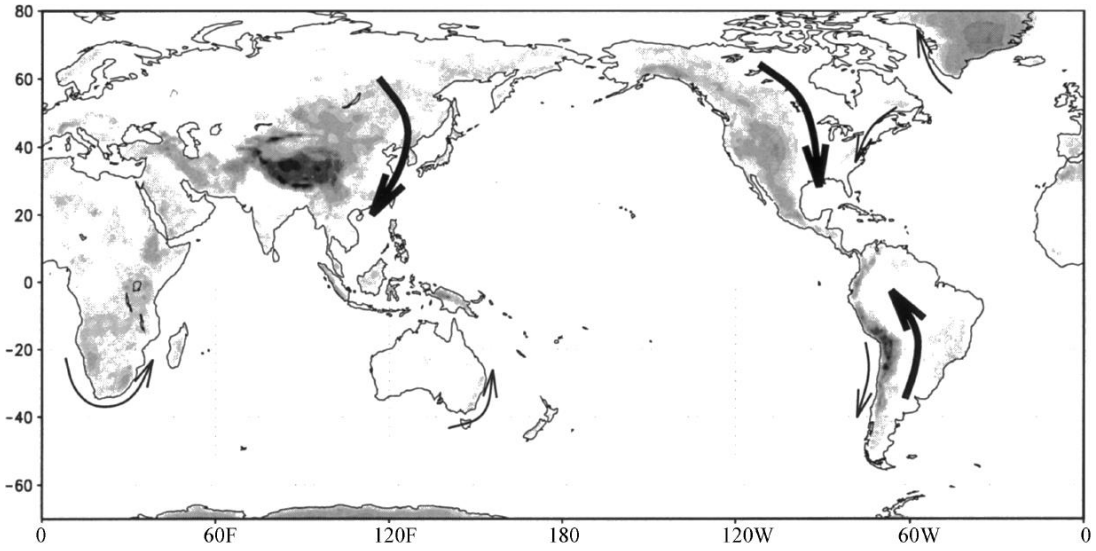


Figure 2.4 Thick arrows indicate the locations where CAOs frequently occur in boreal winter and austral winter (modified from Garreaud (2001)).

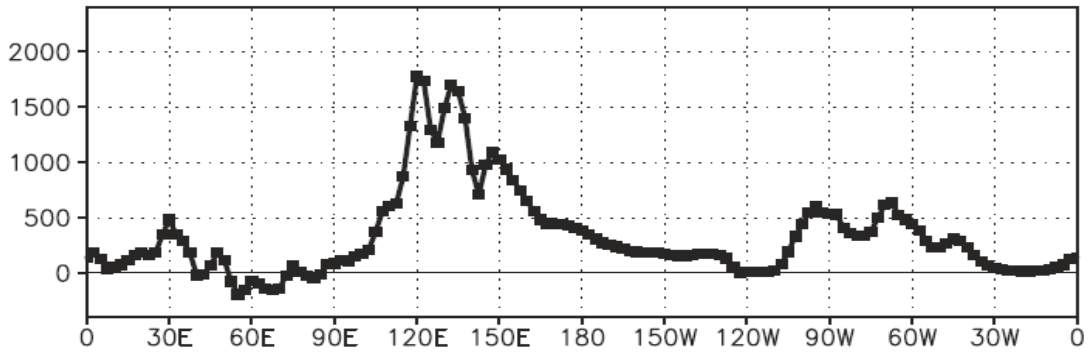


Figure 2.5 Equatorward component of PCAM flux (hPa m $s^{-1}$) along 45°N latitude (modified from Shoji et al. (2014)).

The equatorward cold air streams basically indicate the primary pathways of intermittent CAOs. The discovery of East Asian stream had inspired Shoji et al. (2014) to study cold air outbreaks in East Asia using a quantitative CAO index. Figure 2.5 shows that the maximum stream in East Asia is located at 45N. Shoji et al. introduced an East Asian CAO index (CAOI) by integrated equatorward mass flux over 90°E to 180°:

$$\text{CAOI} \equiv \int_{\lambda=90°\text{E}}^{\lambda=180°} -F_v \, d\lambda \Big|_{\phi=45°\text{N}} \tag{2.8}$$

where $F_v$ is the meridional component of PCAM flux below 280 K. $\lambda$ and $\phi$ are longitude and latitude, respectively. In practice, Shoji et al. multiplied the CAOI with a constant

$$const. = \frac{a \cos \phi}{g}$$

where $a$ and $g$ are Earth's radius and gravitational constant, respectively. In this way, the unit of CAOI will be in kg $s^{-1}$, which is same with the unit of mass streamfunction.

Furthermore, Shoji et al. argued that the index covers too wide area including East Asian continent and the western North Pacific. Therefore, they introduced two more CAO indices:

$$\text{W-CAOI} \equiv \int_{\lambda=90°\text{E}}^{\lambda=135°\text{E}} -F_v \, d\lambda \Big|_{\phi=45°\text{N}} \tag{2.9}$$

$$\text{E-CAOI} \equiv \int_{\lambda=135°\text{E}}^{\lambda=180°} -F_v \, d\lambda \Big|_{\phi=45°\text{N}} \tag{2.10}$$

The W-CAOI and E-CAOI denote CAO indices that specifically measure mass fluxes over the western region (90°E-135°E) and the eastern region (135°E-180°). These indices reveal some distinctions between continental CAO type and oceanic CAO type (Shoji et al. 2014).

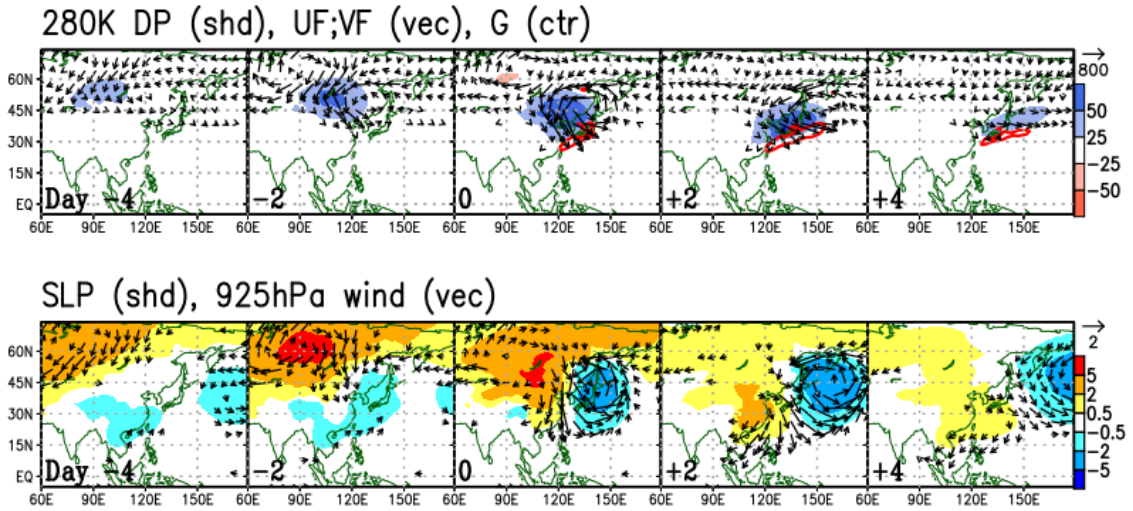


Figure 2.6 Evolution of western CAO event obtained by day-lagged regressions on W-CAO index from day -4 to day +4. Top panels show PCAM and flux anomalies. Bottom panels show sea level pressure and 925-hPa wind anomalies.

A typical evolution of CAO event in East Asia is shown in Figure 2.6. The evolution is depicted using W-CAOI. At day -4, positive anomalies of PCAM develop over inland Asia of Siberia and then grow bigger. At day 0 when CAO occurs, the developed PCAM arrives in East Asia along with enhanced equatorward mass flux. After the events (day +2, +4), the PCAM disappears over the ocean due to vertical heat diffusion from the warm ocean surface. This outbreak of PCAM is preconditioned by enhanced Siberian High (bottom panels of Figure 2.6). Interestingly at day 0 to day +4, the anomalous high pressure penetrates to lower latitudes and maintains the northerly wind anomalies toward the tropical regions although the PCAM already disappears over the subtropics. The enhanced northerlies may cause significant impact on tropical weather systems.

## 2.2 Atmospheric teleconnection caused by tropical convection

The remote influence of the tropical atmosphere over the extratropics is often explained by Rossby wave train theory (Trenberth et al. 1998). The wave train is excited by anomalous upper level divergence associated with large-scale organized convection over the tropics. The divergence is a balance to vertical atmospheric motion associated with latent heat released by moist convection. The resulting atmospheric teleconnection pattern is schematically shown in Figure 2.7. It shows northeastward propagation of wave train as a consequence of the upper level divergent wind confronting the background westerlies at higher latitudes which enable dispersion of Rossby wave energy.

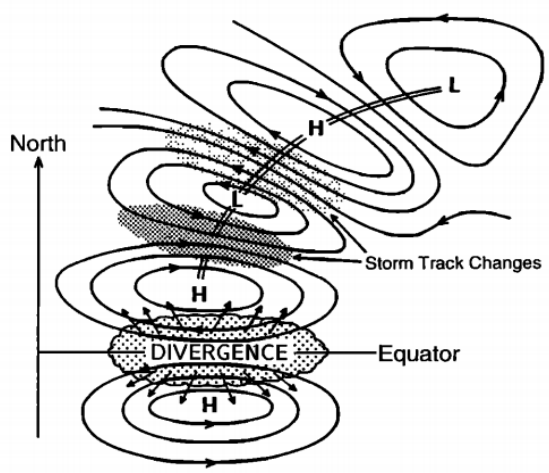


Figure 2.7 Schematic figure of poleward-propagating stationary Rossby wave train as a reponse of upper tropospheric divergence over the tropics. H and L symbols denote high and low pressure centers (modified from Trenberth et al. (1998)).

To demonstrate the global influence of tropical diabatic heating, we perform a numerical experiment using a linearized global climate model (GCM) namely Linear Baroclinic Model (LBM; Watanabe and Kimoto 2000). The LBM uses predefined basic state and forcing. An idealized constant heating is placed over 180° longitude at the equator to mimic the tropical convection (shown by red area in Figure 2.8).The vertical profile of the heating follows a sinusoidal pattern as in Figure 2.9 with its peak at sigma level of 0.37. The maximum temperature rate anomaly at the heating center is approximately 4 K $day^{-1}$. The column average is 2.1 K $day^{-1}$ or corresponds to precipitation rate of 80 mm $day^{-1}$ assuming a relation in Jin and Hoskins (1995). The simulation is conducted using a zonally-symmetric wintertime basic state (DJF climate). A time integration method is used to show the evolution of atmosphere responding to the prescribed heating. At day 3, tropical circulation anomalies start to develop (Figure 2.8). In the western side of heating center, we observe a couple of anticyclone indicating a Rossby wave response. In the eastern side of heating center, anomalous height rapidly propagates to the east indicating a Kelvin wave response. At day 6, the extratropical response is already organized. The anomalous height shows poleward-eastward wave train which controls pressure perturbations over the extratropics. This pattern is consistent with simulation results from previous studies that demonstrated the extratropical response to tropical diabatic heating (Jin and Hoskins 1995; Seo and Son 2012).

How does the wave train develop such kind of pattern? We can understand that by looking at Rossby wave source ($S$) budget that is derived from a barotropic vorticity equation by Sardeshmukh and Hoskins (1988):

$$S' = -\mathbf{v}_\chi{}' \cdot \nabla\bar{\zeta}_a - \bar{\zeta}_a \nabla \cdot \mathbf{v}_\chi{}' - \overline{\mathbf{v}_\chi} \cdot \nabla\zeta_a{}' - \zeta_a{}' \nabla \cdot \overline{\mathbf{v}_\chi} \quad (2.11)$$

where $\mathbf{v}_\chi$ and $\zeta_a$ indicate divergent wind vector and absolute vorticity. Upper bar ( $\bar{}$ ) and comma ( $'$ ) denote winter climate mean and daily deviation from the mean (i.e., anomaly). by Sardeshmukh and Hoskins (1988) showed that the first two terms on the right hand side, which involve anomalous divergent wind, appear to be important terms. The first one is vorticity advection by divergent wind anomaly ($-\mathbf{v}_\chi{}' \cdot \nabla\bar{\zeta}_a$). This term particularly plays large role on the development of subtropical anticyclone located just north of heating center. The southerly anomalies from upper-level divergence come from background easterlies in the tropics and expand to the subtropics where the westerlies start to appear and provide positive gradient of absolute vorticity. This condition yields a negative value on the advection term, causing anticyclone tendency. Whereas the second term is divergence due to divergent wind anomaly ($\bar{\zeta}_a \nabla \cdot \mathbf{v}_\chi{}'$). This term has a strong impact on the downward branch of local Hadley Cell where the entrance of jet stream is usually located. An anomalous upper level convergence yields a positive value on the second term, causing cyclone tendency in the downstream of the former anticyclone at the midlatitude. The disturbances of the vorticity trigger Rossby wave propagation since they are situated in the background westerlies.

The extratropical responses are sensitive to the location of heating and background condition (Trenberth et al. 1998). The responses are more apparent on winter hemisphere than summer hemisphere due to stronger westerly jet during winter. The zonal asymmetry of westerlies in the extratropics, which are controlled by mountains and land-sea distribution, causes variations in the wave train response.

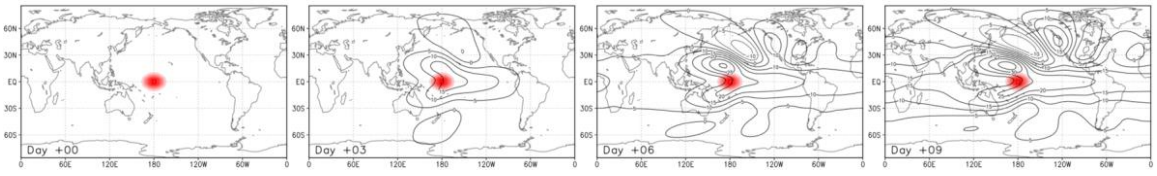


Figure 2.8 A numerical experiment using a linearized global climate model (GCM). Red colors indicate a presribed idealized constant heating centered at 180°E equator (colors greater than 1 K day$^{-1}$ anomaly). The black contours show 200-hPa geopotential height responses to the heating at day +3, +6, and +9 of integration times.

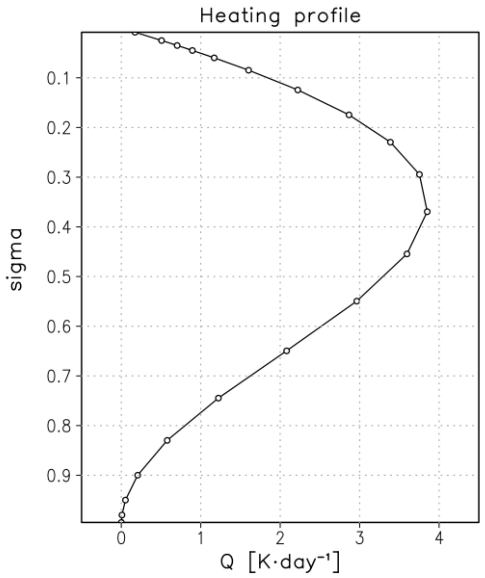


Figure 2.9 Vertical profile of prescribed heating anomaly in the model. The heating follows a sinusoidal pattern $(1 - \sigma) \sin[\pi(1-\sigma)]$ as in Seo and Son (2012).

# 3. Significant roles of El Niño Southern Oscillation on polar cold air mass in the Northern Hemisphere

## 3.1 **Introduction**

Total hemispheric polar cold air mass (total PCAM) amount below a threshold potential temperature is conserved under an adiabatic condition. Any changes in total PCAM amount reflect variability of low-level temperatures in the polar region; therefore total PCAM amount serves as a useful indicator for polar warming, which is as important as an indicator based on surface air temperatures. In the "global" warming framework (IPCC 2013), the total amount of air mass below a particular threshold may become a more meaningful indicator rather than the surface condition alone. The total PCAM amount should consistently decrease under the global warming condition. Kanno et al. (2016) found significant long-term decreasing trend of total PCAM amount in the Northern Hemisphere, which is attributed to global warming and polar amplification (Screen and Simmonds 2010). Nevertheless, the total northern hemispheric PCAM amount exhibits clear interannual variability, which raises questions about the forcing behind it.

This chapter explores the potential influences of tropical forcing on the interannual variability of the northern hemispheric PCAM. Our particular attention is the major tropical climate phenomenon of ENSO, which is known as one of the largest sources of weather/climate variability that can lead to significant societal and economic impacts around the world (Alexander et al. 2002; Brönnimann 2007; Trenberth et al. 1998). Here we reveal the connection of ENSO with hemispheric PCAM. The changes in the total PCAM amount are assessed by a budget analysis using the zonal-mean two-box model. The mechanism of the connection is then clarified by examining the geographical distribution of PCAM anomalies.

---

Contents of this chapter have been published in M. R. Abdillah, Y. Kanno, and T. Iwasaki, 2018a: Strong Linkage of El Niño-Southern Oscillation to the Polar Cold Air Mass in the Northern Hemisphere. *Geophys. Res. Lett.*, 45, 5643–5652, doi:10.1029/2018GL077612.

## 3.2 **Data and method**

We utilize atmospheric variables from the Japanese 55-year Reanalysis (JRA-55) (Kobayashi et al. 2015) during a study period from 1981/82 to 2016/17 (Dec-Feb). The JRA-55 has a 6-hour temporal resolution, 1.25° horizontal resolution, and 37 vertical pressure levels. To represent ENSO variability, we use a sea surface temperature (SST) anomaly index in the Niño-3.4 region (Trenberth, 1997). In addition, we also use an Arctic Oscillation (AO) index for a comparative analysis.

This study particularly discusses the possible influence of ENSO on variability of total PCAM amount ($\langle DP \rangle$). To quantify seasonal changes in $\langle DP \rangle$, we introduce a budget analysis of total PCAM on the basis of zonal-mean two box model (Kanno et al. 2015b). The two-box model framework is explained in Chapter 2.1.2, which shows that the long-term mean (e.g., seasonal time scale and beyond) of total PCAM amount ($\langle DP \rangle$) is nearly balanced with the two time constants ($\tau_1$ and $\tau_2$) and zonal mean equatorward outflow at 45°N ($I$):

$$\langle DP \rangle = (\tau_1 + \tau_2) I$$

By considering that a seasonal variable can be decomposed into a seasonal anomaly (denoted by a delta) and a climate mean (denoted by an over-bar), for example

$$A = \bar{A} + \Delta A,$$

we obtain that the seasonal anomaly of $\langle DP \rangle$ is controlled by four budget terms as shown in the right-hand side of the following equation:

$$\Delta\langle DP \rangle = \Delta I(\bar{\tau_1} + \bar{\tau_2}) + \Delta(\tau_1 + \tau_2)\bar{I} + \Delta(\tau_1 + \tau_2)\Delta I - \overline{\Delta(\tau_1 + \tau_2)\Delta I}\,. \qquad (3.1)$$

Figure 3.1 shows time series of the four terms over recent 36 winters. The first two terms in the right-hand side of equation 3.1 clearly play the primary roles whereas the effects of other two terms in the right-hand side (i.e., residual terms) are very minor and thus negligible.

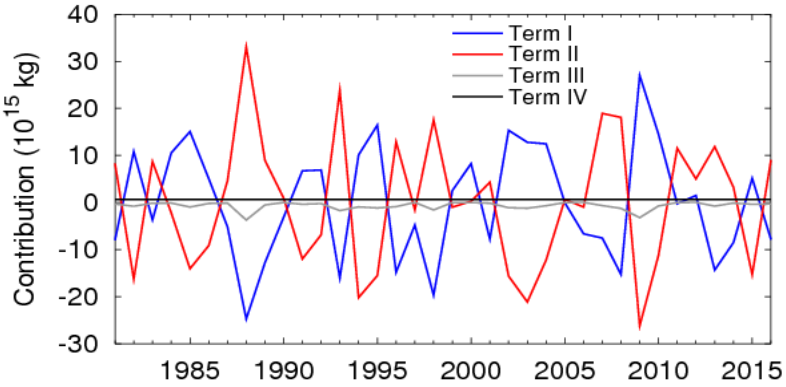


Figure 3.1 Interannual variation of four budget terms in the right-hand side of equation 3.1.

By removing the "weak" terms, decomposing term 2 into two time constant terms, and normalizing with the climate mean of $\langle DP \rangle$, we obtain three terms that control $\langle DP \rangle$ anomalies:

$$\frac{\Delta\langle DP\rangle}{\overline{\langle DP\rangle}} \approx \frac{\Delta I}{\bar{I}} + \frac{\Delta\tau_1}{(\overline{\tau_1}+\overline{\tau_2})} + \frac{\Delta\tau_2}{(\overline{\tau_1}+\overline{\tau_2})}. \tag{3.2}$$

Therefore, changes in the total PCAM amount can arise due to: 1) changes in equatorward cold air outflow at 45°N, 2) changes in the residence time of PCAM at high latitudes, and 3) changes in the life time of PCAM at low latitudes. To represent the roles of ENSO, we perform linear regressions with the Niño-3.4 SST index. The statistical significant levels are calculated based on a two-sided Student's *t* test.

The following Chapter 3.3 reveals significant association between ENSO and total PCAM variability and explains the reason using the budget equation. After obtaining the budget terms that appear to be important, Chapter 3.4 shows a geographical analysis of PCAM distribution and its controlling variables to clarify the mechanisms. The geographical distribution of PCAM and its flux anomalies are also expected to provide useful information about regional changes that may have significant impacts on the associated regions. In that chapter, we conduct an additional budget analysis to quantify physical mechanisms that play roles on regional PCAM anomalies. Chapter 3.5 discusses the relationship with surface air temperature, the possible role of Arctic Oscillation (AO), and the sensitivity of results to PCAM threshold. The key findings are summarized in Chapter 3.6.

## 3.3 Interannual variability of total PCAM amount associated with ENSO

The first series in Figure 3.2 shows the seasonal means of $\langle DP \rangle$ over 36 recent winters. The variation exhibits an obvious negative trend due to warming in the polar region (Kanno et al. 2016). The second series denotes the winter Niño-3.4 SST index. Surprisingly, the variations

of $\langle DP \rangle$ and Niño-3.4 SST exhibit a clear out-of-phase relationship. The lowest value of $\langle DP \rangle$ occurs concurrently with the recent extreme 2015/16 El Niño (L'Heureux et al. 2017). The correlation coefficients between the two series are -0.49 (unfiltered) and -0.66 (detrended), exceeding the statistically significant levels of 1% and 0.1%, respectively. The long-term trend of $\langle DP \rangle$ is quite significant (Kanno et al. 2016). Here the trend explains approximately 35% of the total variance of $\langle DP \rangle$ during the study period. To focus our attention on interannual variability, we employ the detrended data for the rest of our analysis. The standard deviation of detrended $\langle DP \rangle$ is $5.61 \times 10^{15}$ kg or approximately 2.5% of its climatology. A correlation/regression map between $\langle DP \rangle$ and tropical SST anomalies shows a tongue-like SST pattern over the eastern Pacific—suggesting the association with canonical ENSO events—with the center of anomalies appearing over the Niño-3.4 region (Figure 3.3). The strong ENSO-PCAM relationship suggests a significant role of ENSO, where the negative correlation means that El Niño reduces the total PCAM amount, and La Niña increases the amount. The decreasing or increasing PCAM may imply warmer or colder extratropical air temperatures, respectively.

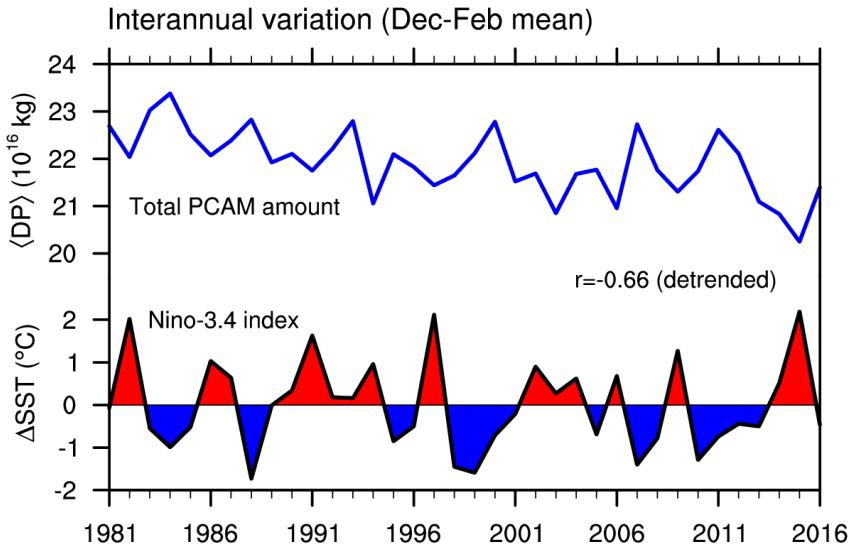


Figure 3.2 Interannual variations of the total hemispheric PCAM amount in the Northern Hemisphere (blue line) and the Niño-3.4 SST anomaly index (black line). Here, the winter of 1981 denotes the 1981/82 winter.

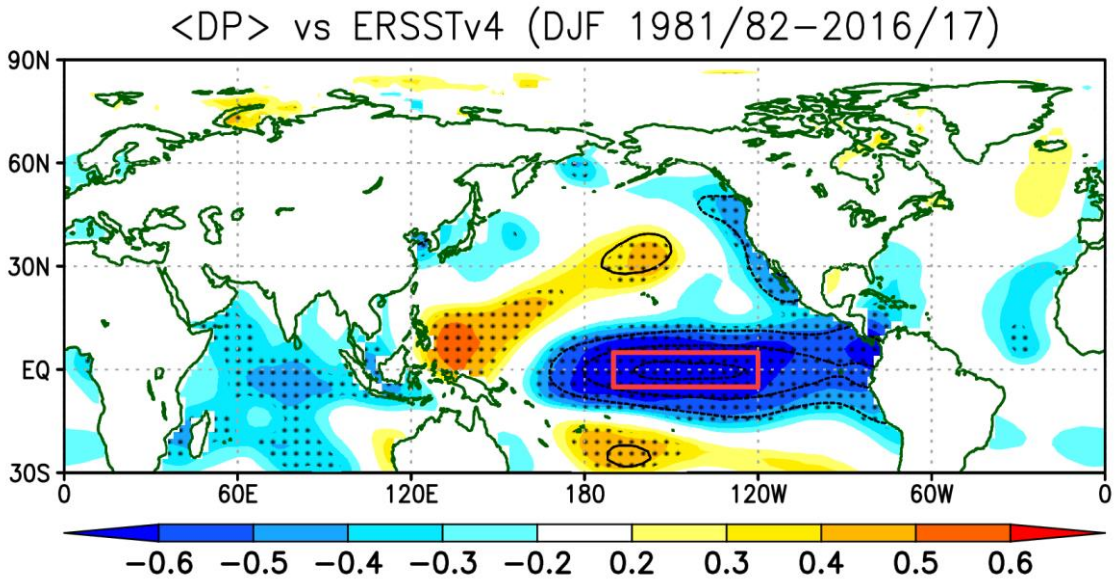


Figure 3.3 Interannual correlation/regression between the detrended total northern hemispheric PCAM ($\langle DP \rangle$) and sea surface temperature anomalies during boreal winter. The shaded areas denote correlation coefficients and the black contours denote regression coefficients (contour interval: 0.3°C; zero contours omitted). Dotted areas satisfy statistical significance at 5%. Red box represents the Niño-3.4 region.

Table 3.1 summarizes the linear impacts of ENSO explained by the two-box model. The presented anomalies indicate the average changes that would occur if the Niño-3.4 SST anomaly reaches +1 standard deviation, resembling El Niño conditions. One of the interesting features is that the equatorward cold air outflow $I$ is significantly increased. The strengthening of $I$ indicates an increase in zonal-mean cold air outbreaks and has implications for a decrease in the PCAM in the genesis box and an increase in the PCAM in the loss box (Kanno et al. 2015a). The decrease in the genesis box (high latitude) is characterized by a decrease in the PCAM residence time $\tau_1$. According to the budget equation of $\langle DP \rangle$, the changes in $I$ and $\tau_1$ contribute to an increase of 1.84% and a decrease of 3.13% in $\langle DP \rangle$, respectively. The negative effect of $\Delta\tau_1$ is stronger than the positive effect of $\Delta I$, implying that the amount of the PCAM decrease at high latitudes is larger than the amount of the PCAM transferred across mid-latitudes through cold air outbreaks. Furthermore, the lifetime of PCAM in the loss box $\tau_2$ is also shorter, but it contributes very little to the change in $\langle DP \rangle$ (only 0.48% decrease).

Table 3.1 Influences of ENSO on the total hemispheric PCAM amount ($\langle DP \rangle$) explained in the zonal-mean two-box model. Percentage values are relative to the climatology of $\langle DP \rangle$. Single (*) and double (**) asterisks denote statistically significant changes at 5% and 0.1%,

| Two-box model parameter | Linear change during El Niño | Contribution to total hemispheric PCAM change |
|---|---|---|
| Equatorward cold air outflow at 45°N ($I$) | $+1.83\times10^9$ kg $s^{-1}$* | +1.84%** |
| Residence time in genesis box ($\tau_1$) | -0.80 day** | -3.13%** |
| Life time in loss box ($\tau_2$) | -0.12 day** | -0.48% |
| Net change in total PCAM amount ($\Delta\langle DP \rangle$) | | -1.77%** |

Combining all of these factors, the estimated net change in $\langle DP \rangle$ during El Niño is approximately -1.77% with the primary contribution coming from the influence of $\Delta\tau_1$. This estimation is not much different from the $\Delta\langle DP \rangle$ calculated directly from the regression (-1.69%). In the seasonal mean, the change in $I$ should be similar to the changes in $\langle G \rangle_1$ and $\langle L \rangle_2$ because the temporal means of the tendency terms in equation (2.5) are nearly zero, such that $\Delta I \approx \Delta\langle G \rangle_1 \approx \Delta\langle L \rangle_2$. Some differences among these parameters may arise due to calculation errors and non-steady effects. By calculating the differences among $\Delta I, \Delta\langle G \rangle_1$, and $\Delta\langle L \rangle_2$, we estimate that the errors in the steady-state assumption are quite small (approximately ±0.2% of the climatology of $I$).

## 3.4 Geographical patterns of ENSO influence

During El Niño, why does $\tau_1$ decrease significantly and have a large contribution to $\langle DP \rangle$? To answer this question, it is essential to reveal the geographical distribution of PCAM anomalies and associated controlling variables because $\tau_1$ is affected by land-sea distribution and topography (Kanno et al. 2015b). Figure 3.4 shows the correlations and regressions of several climate variables with the Niño-3.4 index. The distribution of PCAM anomalies varies regionally (Figure 3.4a). The largest reduction in PCAM amount is found over North America spanning from the eastern North Pacific, Alaska, and Canada, to the northern continental U.S. A reduction in the PCAM amount is also observed over Eurasia, elongating from the east of the Caspian Sea to Japan, although its magnitude is relatively weaker than that in the western hemisphere. Meanwhile, positive PCAM anomalies appear over the central North Pacific. The distribution of PCAM anomalies is similar to that of surface air temperature anomalies in mid- to high latitudes, where a decrease (increase) in the PCAM indicates warming (cooling) of the

surface air (Figure 3.4e). The negative anomalies of the PCAM over North America, particularly over the northwestern part, are consistent with the surface warming that has been commonly observed in previous studies (Diaz et al., 2001; Hoerling et al., 1997; Horel & Wallace, 1981; Trenberth et al., 1998; Walker & Bliss, 1932). Slight differences between PCAM anomalies and temperature anomalies may appear because the definition of the PCAM does not consider temperature variations beneath the threshold potential temperature (Iwasaki et al. 2014).

The geographical patterns of PCAM flux anomalies agree well with the geostrophic constraint associated with mean sea level pressure changes (Figure 3.4b,d). In the northeastern Pacific, a negative pressure anomaly indicates the strengthening of the Aleutian Low. The anomalous cyclonic circulation causes anomalous PCAM migration from North America to the central North Pacific. In the east of the cyclonic anomaly center, poleward flux anomalies emerge that span from off the coast of western North America to inland North America.

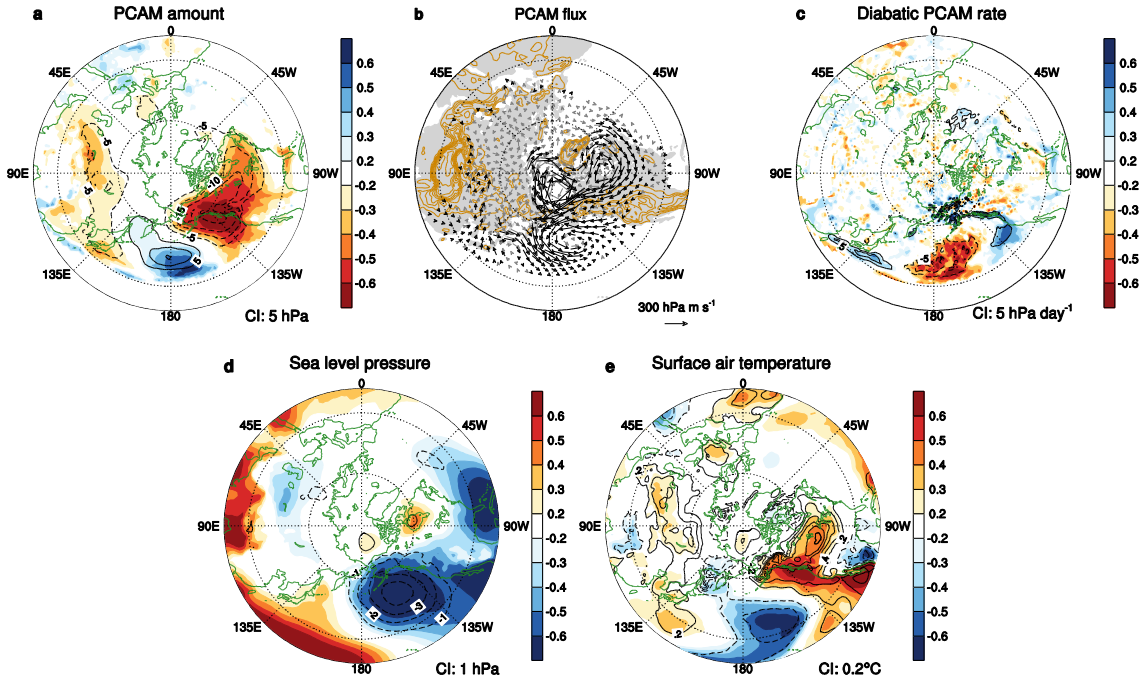


Figure 3.4 Interannual correlations and regressions of several detrended several climate variables with the Niño-3.4 index. The panels show (a) PCAM amount, (b) PCAM flux, (c) diabatic genesis/loss rate of PCAM, (d) mean sea level pressure, and (e) surface air temperature at 2 m. The shadings denote the correlation coefficients. The black contours and vector fields denote climate anomalies inferred from a linear regression with the standardized Niño-3.4 index. Zero contours are omitted. In (b), the black vectors denote correlation coefficients of the zonal or meridional component higher that are higher than 0.3; orange contours indicate topography at 500 m interval. The contour interval (CI) or reference vector is shown in the bottom-right of each panel.

In the east of the Rocky Mountains, the poleward flux anomalies are situated over the climatological North American stream, indicating the decrease in equatorward advection of the PCAM and consequently causing a reduction in the PCAM amount (e.g., Kanno et al. 2017). In Alaska, westward flux anomalies prevail and also cause a significant PCAM reduction. This reduction due to zonal flux anomalies can be explained by changes in the zonal advection of the PCAM (further discussed in the last paragraphs of this section). In the central North Pacific, equatorward flux anomalies appear (Figure 3.4b,d). The anomalous equatorward flow extends to mid-latitudes and ultimately represents the increase in zonal-mean cold air outflows at the critical latitude of two-box model (Table 3.1). Despite a vivid and wide spread of equatorward flux anomalies in the North Pacific, the magnitude and coverage of positive PCAM anomalies are quite small in comparison to those of negative anomalies over North America. This large difference arises because the anomalous equatorward flux is situated over the warm ocean, which enhances the loss rate of the PCAM due to diabatic heating (Figure 3.4c), hence suppressing the PCAM development downstream of equatorward flux anomalies.

The anomalous transport of the PCAM from the high latitudes of North America to the midlatitudes of the North Pacific is the main reason for the shorter $\tau_1$. The PCAM decrease at high latitudes is not fully compensated by the PCAM increase at lower latitudes due to equatorward outflow situated over the warm ocean, resulting in a significant negative anomaly of $\langle DP \rangle$.

The pressure anomalies that drive the circulation in the North Pacific and North American sectors resemble the surface signatures of a positive phase of Pacific-North American (PNA) teleconnection pattern (Wallace and Gutzler 1981). The phases of the PNA pattern are often modulated by ENSO-induced convection anomalies over the central Pacific (Trenberth et al., 1998).

Some notable features appear over Eurasia although their signals are relatively weaker than those over North America and the North Pacific (Figure 3.4). In East Asia, poleward flux anomalies emerge due to the development of a high-pressure anomaly over the western North Pacific and contribute to the weakening of the western part of East Asian stream and the reduction in the PCAM. This reduction is consistent with the general agreement stating that El Niño causes warm winters or weak winter monsoons in East Asia (Chang et al. 2006). A detailed discussion on the impact of ENSO on the East Asian PCAM is documented in next Chapter 4, which shows that the Rossby wave train excited by ENSO-induced convection anomalies over the Maritime Continent/western Pacific plays a role in constructing circulation anomalies over East Asia that affect PCAM advection(Abdillah et al. 2017; Zheng et al. 2013).

Furthermore, Figure 3.4a shows negative PCAM anomalies extending toward inland Eurasia. This reduction, however, is difficult to explain by the anomalous PCAM advection alone since the anomalous flux is rather unclear over inland areas (Figure 3.4b) and thus requires further investigation.

Budget analysis on local PCAM amount

To provide physical evidences on PCAM anomalies at each grid point, we conduct an additional budget analysis to quantify the factors that contribute to seasonal changes in regional PCAM amount. The conservation rule of PCAM at each grid point is shown in equation (2.2). In seasonal time scale, the tendency term is practically very small. Thus the divergence of horizontal PCAM flux, $\mathbf{F}$, is nearly balanced with the diabatic genesis rate of PCAM, $G$ (Iwasaki et al. 2014),

$$\boldsymbol{\nabla} \cdot \mathbf{F} \approx G. \tag{3.3}$$

In equation (3.3)., the role of wind field acting on PCAM amount is implicitly shown in $\mathbf{F}$. To quantify contributions associated with the wind field, we introduce a vector field variable, $\mathbf{v}_m$, defined as a division between PCAM flux and PCAM amount ($\mathbf{v}_m \equiv \mathbf{F}/DP$). Therefore $\mathbf{v}_m$ can be interpreted as *mean* horizontal wind below threshold $\theta_T$. Here, $\mathbf{v}_m$ is calculated on seasonal basis, which depends on seasonal means of PCAM state. Equation (3.3) is then modified to

$$\boldsymbol{\nabla} \cdot (\mathbf{v}_m DP) = G. \tag{3.4}$$

As in the previous two-box model framework, each seasonal quantity can be considered to include both a climate mean (denoted by an over bar) and interannual variability (denoted by a delta). Applying this rule on equation (3.4) yields

$$\boldsymbol{\nabla} \cdot (\overline{\mathbf{v}_m}\,\overline{DP}) + \boldsymbol{\nabla} \cdot (\overline{\mathbf{v}_m}\Delta DP) + \boldsymbol{\nabla} \cdot (\Delta\mathbf{v}_m\,\overline{DP}) + \boldsymbol{\nabla} \cdot (\Delta\mathbf{v}_m \Delta DP) = \bar{G} + \Delta G. \tag{3.5}$$

Because the climate mean of PCAM is also balanced as shown by $\boldsymbol{\nabla} \cdot (\overline{\mathbf{v}_m DP}) = \bar{G}$, or in a longer form

$$\boldsymbol{\nabla} \cdot (\overline{\mathbf{v}_m}\,\overline{DP}) + \boldsymbol{\nabla} \cdot (\overline{\Delta\mathbf{v}_m \Delta DP}) = \bar{G}, \tag{3.6}$$

we can eliminate climate mean terms in equation 3.6 and obtain

$$\boldsymbol{\nabla} \cdot (\overline{\mathbf{v}_m}\Delta DP) + \boldsymbol{\nabla} \cdot (\Delta\mathbf{v}_m\,\overline{DP}) + \boldsymbol{\nabla} \cdot (\Delta\mathbf{v}_m \Delta DP) - \boldsymbol{\nabla} \cdot (\overline{\Delta\mathbf{v}_m \Delta DP}) = \Delta G. \tag{3.7}$$

Separating the first divergence term into $\overline{\mathbf{v}_m} \cdot \boldsymbol{\nabla}\Delta DP + \Delta DP\boldsymbol{\nabla} \cdot \overline{\mathbf{v}_m}$ and the second divergence term into $\Delta\mathbf{v}_m \cdot \boldsymbol{\nabla}\overline{DP} + \overline{DP}\boldsymbol{\nabla} \cdot \Delta\mathbf{v}_m$, we finally obtain a simple approximation of PCAM change

$$\Delta DP = \frac{1}{\boldsymbol{\nabla} \cdot \overline{\mathbf{v}_m}}(-\Delta\mathbf{v}_m \cdot \boldsymbol{\nabla}\overline{DP} - \overline{DP}\boldsymbol{\nabla} \cdot \Delta\mathbf{v}_m + \Delta G + \mathrm{Res}), \tag{3.8a}$$

where Res is considered as a residual or balancing term that contains the following terms:

$$\mathrm{Res} = -\overline{\mathbf{v}_m} \cdot \boldsymbol{\nabla}\Delta DP - \boldsymbol{\nabla} \cdot (\Delta\mathbf{v}_m\Delta DP) + \boldsymbol{\nabla} \cdot (\overline{\Delta\mathbf{v}_m\Delta DP}). \tag{3.8b}$$

Equation (3.8) indicates how anomalies in PCAM amount arise from anomalies in wind field and diabatic change rate. Description of all contributing terms on the right-hand side of equation (3.8) is shown in the following points. Note that, the contributing terms depend on the inverse of background wind divergence ($\frac{1}{\boldsymbol{\nabla} \cdot \overline{\mathbf{v}_m}}$). To simplify the explanation, the following description assumes the condition of $\boldsymbol{\nabla} \cdot \overline{\mathbf{v}_m} > 0$ (which is actually true in most regions; see Figure 3.5).

1. $-\Delta\mathbf{v}_m \cdot \boldsymbol{\nabla}\overline{DP}$ : This term represents the advection of background PCAM amount by wind anomalies (hereafter "advection term"). We later find that this is the most influential term. Southerly anomalies usually cause PCAM reduction since the meridional gradient $\frac{\partial\overline{DP}}{\partial y}$ is positive in almost all areas.

2. $-\overline{DP}\boldsymbol{\nabla} \cdot \Delta\mathbf{v}_m$ : This term represents the influence of divergence of wind anomalies (hereafter "divergence term"). The influence largely depends on the background PCAM amount**.**

3. $\Delta G$ : This term represents the only diabatic-related term (hereafter "diabatic term"). The positive change in $\Delta G$ indicates diabatic PCAM genesis due to anomalous diabatic cooling, vice versa for the negative change. This term is expected to be large over the mid-latitude ocean and the coastal areas.

4. Res : This term summarizes residual terms that act to balance the contributions from the aforementioned first three terms. It is a combination of the followings.

    a. $-\overline{\mathbf{v}_m} \cdot \boldsymbol{\nabla}\Delta DP$ : This term shows the advection of PCAM anomalies by background wind. This term appears to consolidate $\boldsymbol{\nabla} \cdot (\overline{\mathbf{v}_m}\Delta DP)$ in equation (3.7)**.** As shown in the comparison figure later, this term is relatively unimportant over the centers of PCAM anomalies (small $\boldsymbol{\nabla}\Delta DP$ area). This term

apparently acts to balance any "excessive" anomalies that are produced by other terms between the centers of PCAM anomalies (large $\nabla\Delta DP$ area).

b. $-\nabla\cdot(\Delta\mathbf{v}_m\Delta DP)$ : This term represents wind anomalies acting on PCAM anomalies. The effect of this term (and the following term) is quite smaller than other climate-containing terms because the anomalies are generally much smaller than their climate mean parts.

c. $\nabla\cdot(\overline{\Delta\mathbf{v}_m\Delta DP})$ : This term is a constant denoting the mean product of wind and PCAM anomalies. At last, this term simply arises to consolidate all climate mean terms in equation (3.6) into a single 'background' field.

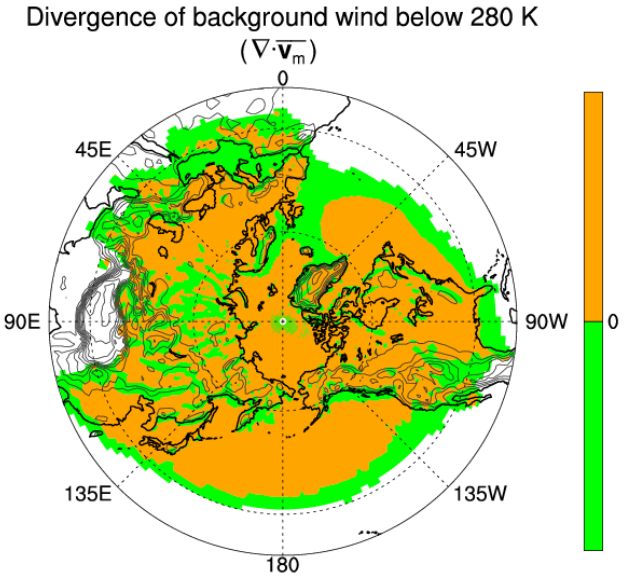


Figure 3.5 Divergence of background wind below 280 K ($\nabla\cdot\overline{\mathbf{v}_m}$). Orange and green shadings indicate regions of positive and negative divergence, respectively. Black contours denote topography with a 500 m contour interval.

All source terms in the right-hand side of equation 3.8 are then calculated at each year along the study period using central finite difference method. To diagnose the influence of ENSO, here we assume a linear ENSO effect using regressions with standardized Nino-3.4 index. It should be noted that the source terms in equation 3.8 depend on the inverse of divergence of background wind ($\frac{1}{\nabla\cdot\overline{\mathbf{v}_m}}$). To avoid unrealistic results, zero or near zero values of $\nabla\cdot\overline{\mathbf{v}_m}$ are adjusted as followings.

If $\nabla \cdot \overline{\mathbf{v}_m} \geq 0$ and $\nabla \cdot \overline{\mathbf{v}_m} < 10^{-6}\mathrm{s}^{-1}$, then $\nabla \cdot \overline{\mathbf{v}_m} = 10^{-6}\mathrm{s}^{-1}$,

If $\nabla \cdot \overline{\mathbf{v}_m} < 0$ and $\nabla \cdot \overline{\mathbf{v}_m} > -10^{-6}\mathrm{s}^{-1}$, then $\nabla \cdot \overline{\mathbf{v}_m} = -10^{-6}\mathrm{s}^{-1}$.

Slight different choice of divergence limit (here $\pm 10^{-6}\mathrm{s}^{-1}$) does not affect the main feature of estimated PCAM anomalies. The important part is the mathematical sign of $\nabla \cdot \overline{\mathbf{v}_m}$. The contribution of each source term will be positive or negative depending on the sign. To reduce the effect of discretization, a nine-point local smoothing is applied to the estimated terms.

Figure 3.6 shows the results. Sum of all terms in the right-hand side of equation (3.8a) (Figure 3.6a) is very consistent with anomalous PCAM amount from the regression in Figure 3.4. The pattern shows strong PCAM reduction in North America, increasing in the North Pacific, and slight reduction in Asia. Minor differences between those calculated from budget analysis and those from regression may appear due to the limitation of budget calculation.

The relative contributions from the first three source terms (advection, divergence, and diabatic terms) are shown in Figure 3.6b-d, while the residuals are shown in Figure 3.8. The effect of cyclonic circulation anomaly in the Northeastern Pacific is quite clear, which is mainly manifested in the advection term, $-\Delta\mathbf{v}_m \cdot \nabla\overline{DP}$. The eastern and northern side of anomalous cyclone causes reduction of PCAM anomaly because of the appearance of southerly and easterly anomalies, respectively; while the western side causes an increase of PCAM amount because northerly anomalies appear near the date line. In addition, anomalous westward advection over the Alaska and Bering Strait also has substantial impact on PCAM reduction owing to the negative zonal gradient of background PCAM (Figure 3.7a,c). Furthermore in East Asia, we also observe the effect of anomalous poleward advection to the reduction of PCAM. These results clarify physical processes presented on the main paper which shows the importance of advection by anomalous flux over North America, North Pacific, and East Asia. Comparison based on area-averaged terms gives a clear picture of the major role of advection term (Figure 3.6e).

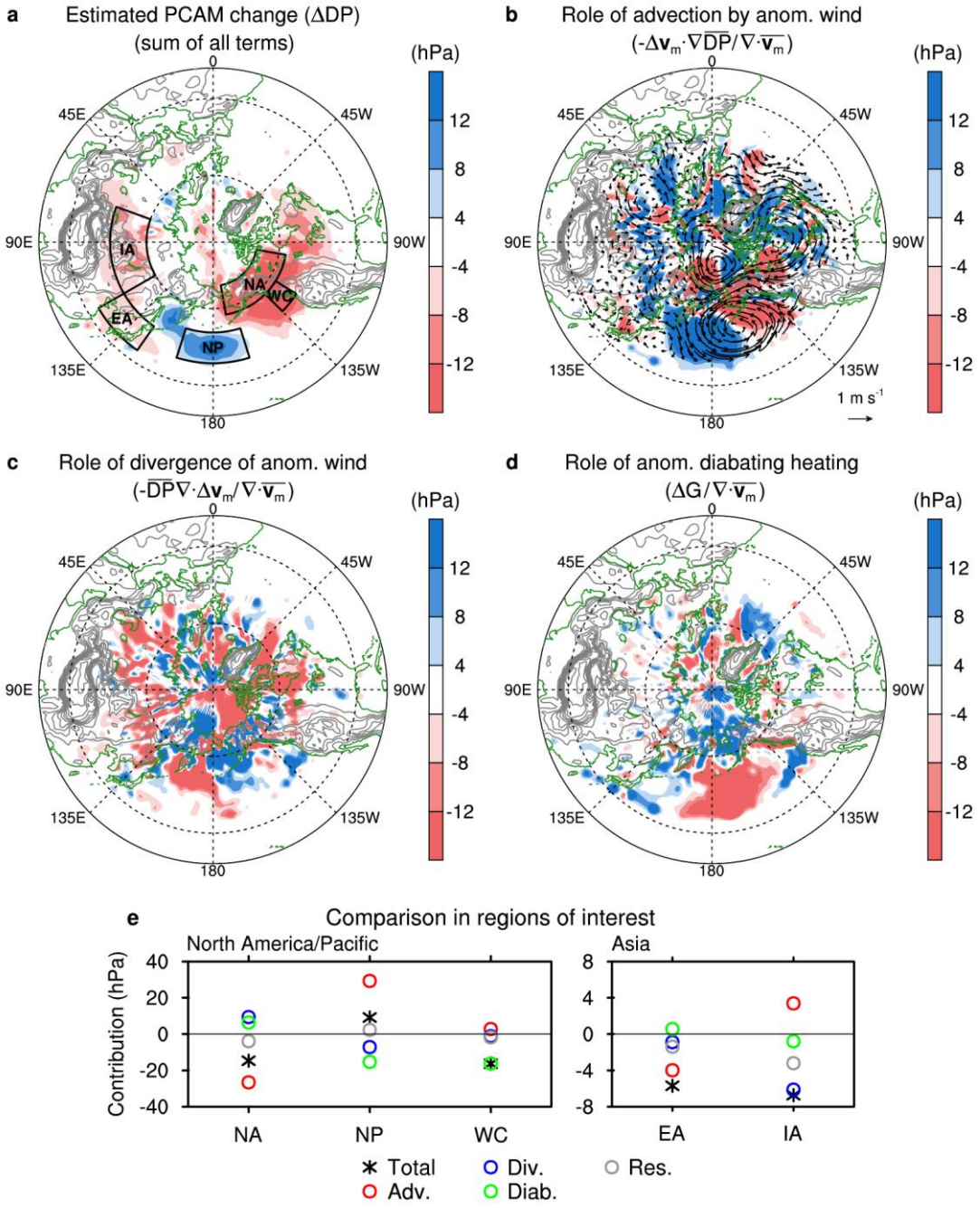


Figure 3.6 Decomposition of physical processes behind PCAM anomalies (hPa) associated with ENSO. The values are obtained from regression of the contributing terms onto Nino-3.4 index. (a) Sum of all terms. (b-d) Contribution of advection term (Adv.), divergence term (Div.), and diabatic term (Diab.), respectively. (e) Comparison of different terms in several selected regions denoted by black boxes in (a). NA, NP, WC, EA, and IA stand for North America, North Pacific, western Coast, East Asia, and inland Asia, respectively. Residual term (Res.) is shown in Fig. S4. S4. Grey contours denote topography with a 500 m contour interval.

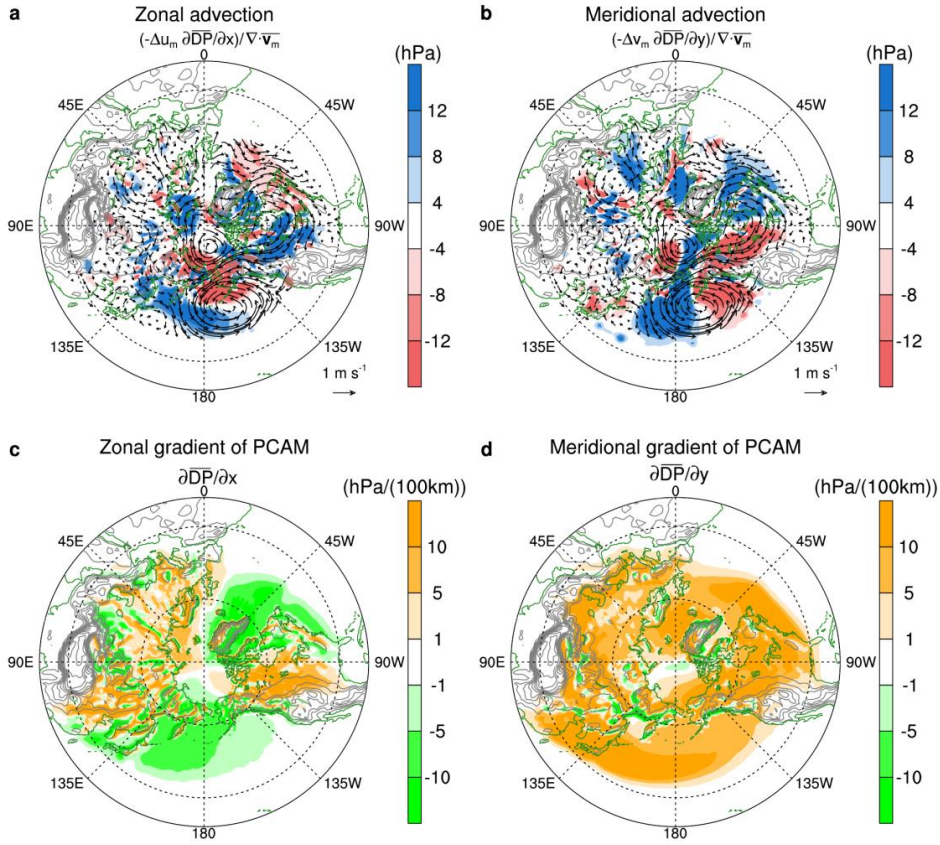


Figure 3.7 Decomposition of advection term. (a) and (b) show the relative contributions of advection by anomalous zonal wind and anomalous meridional wind (hPa), respectively. Sum of (a) and (b) is identical to Fig. S2b. (c) and (d) show zonal gradient and meridional gradient of background PCAM amount (hPa/100 km), respectively.

The second contributor is divergence term, $-\overline{DP}\nabla \cdot \Delta \mathbf{v}_m$ (Figure 3.6c). Its amplitude is relatively low over mid/low latitude regions. Although this term seems strong in high latitudes, most of its signals are apparently compensated by other terms and do not appear prominently in the net PCAM change. A notable influence of this term appears over inland central Asia and turns out as the largest contributor for PCAM reduction over there (Figure 3.6c,e). The result provides a physical reason for PCAM reduction over inland Eurasia that is presented on the main paper. Divergence of wind anomalies that contribute to this term are possibly the results of interactions between anomalous wind and topography north of Tibetan plateau.

The third contribution comes from diabatic term, $\Delta G$ (Figure 3.6d). The pattern of anomalous diabatic PCAM change rate has been discussed on the main paper. In the North Pacific, a wide area of diabatic heating anomalies appears and effectively suppresses the development of PCAM amount during the course of southward advection (Figure 3.6b), leaving only a relatively small increase of PCAM in the North Pacific. Over Kuroshio Current south of

Japan, some diabatic cooling anomalies associated with the weakening of East Asian equatorward flux contribute to PCAM increase. Yet, its increase is nearly balanced with the residual $-\overline{\mathbf{v}_m} \cdot \boldsymbol{\nabla}\Delta DP$ (Figure 3.8a). One of significant and interesting influences of diabatic term is found around the western Coast of Canada (Figure 3.6d,e). In this area, the effect of advection term is very small due to the hindrance of topography. This area is located over negative-divergence of background wind which states that, according to the budget equation, positive $\Delta G$ will cause negative $\Delta DP$.

The residual term is shown in Figure 3.8. The influence of background wind acting on PCAM anomalies, $-\overline{\mathbf{v}_m} \cdot \boldsymbol{\nabla}\Delta DP$, appears over the large gradient of $\Delta DP$ (Figure 3.8a). This term apparently acts to balance any "excessive" anomalies that are produced by other terms between the centers of PCAM anomalies. On the other hand, the influence of anomalies terms $(-\boldsymbol{\nabla} \cdot (\Delta\mathbf{v}_m \Delta DP) + \boldsymbol{\nabla} \cdot (\overline{\Delta\mathbf{v}_m \Delta DP}))$ is very small (Figure 3.8b). The general feature of PCAM anomalies is still unchanged when this term is neglected.

Therefore, according to the above result, we find that the important source terms for local PCAM amount are: 1) advection of the background PCAM by wind anomalies (advection term), 2) divergence of wind anomalies acting on the background PCAM (divergence term), and 3) changes related to diabatic cooling/heating (diabatic term) (Figure 3.6). The advection term has major effects on PCAM anomalies over North America, the North Pacific, and East Asia, which are consistent with the aforementioned results. It turns out that the reduction in the inland Eurasia is dominated by the divergence term which seems to be associated with the interactions of mass flux and topography. On the other hand, the diabatic term is necessary over the North Pacific where the anomalous diabatic heating hinders the development of PCAM over the ocean.

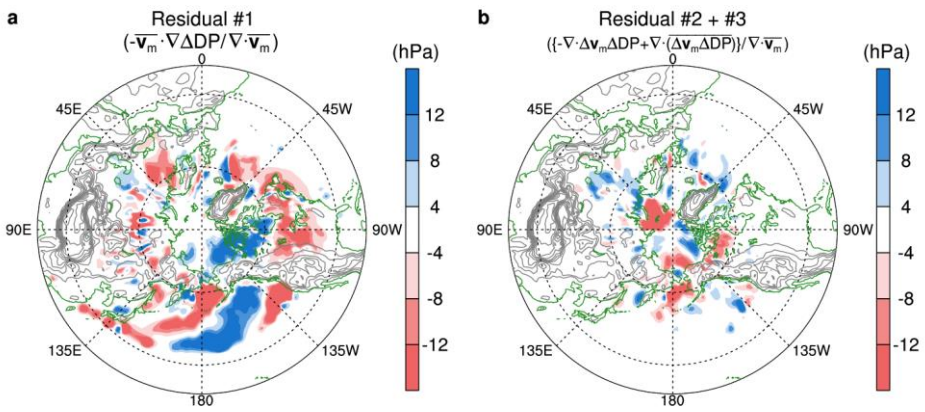


Figure 3.8 Effect of residual terms (hPa). (a) Contribution from the background wind acting on PCAM anomalies $(-\overline{\mathbf{v}_m} \cdot \boldsymbol{\nabla}\Delta DP)$. (b) Contribution from the anomalies terms $\left(-\boldsymbol{\nabla} \cdot (\Delta\mathbf{v}_m \Delta DP) + \boldsymbol{\nabla} \cdot (\overline{\Delta\mathbf{v}_m \Delta DP})\right)$. Grey contours denote topography with a 500 m contour interval.

## 3.5 Discussion

### 3.5.1 Relationship between PCAM and surface air temperature

In the extratropics, the surface air temperature (SAT) has also a good relationship with ENSO through the signature of PCAM anomalies (Figure 3.4a,e). Previous studies showed that the increase or decrease in the PCAM amount indicates cooling or warming of the SAT, respectively (Kanno et al. 2015a; Shoji et al. 2014). Here, we will quantify the robustness of their relationship. Figure 3.9 shows the grid-by-grid interannual correlation between the detrended PCAM and SAT. The correlation coefficients are stronger than -0.8 over a large portion of the northern extratropics, including East Asia and North America where cold air outbreaks frequently occur (Garreaud 2001). However, the relationship is relatively weak in some regions, especially over the Arctic Circle, where the background PCAM is very thick, and over some seas or straits. The prevalence of strong surface-based temperature inversions at the high latitudes (Kahl et al. 1992) and other diabatic processes beneath 280 K could be the reasons for the imperfect relationship between PCAM and SAT. These factors may explain the difference between the ENSO responses of PCAM and SAT.

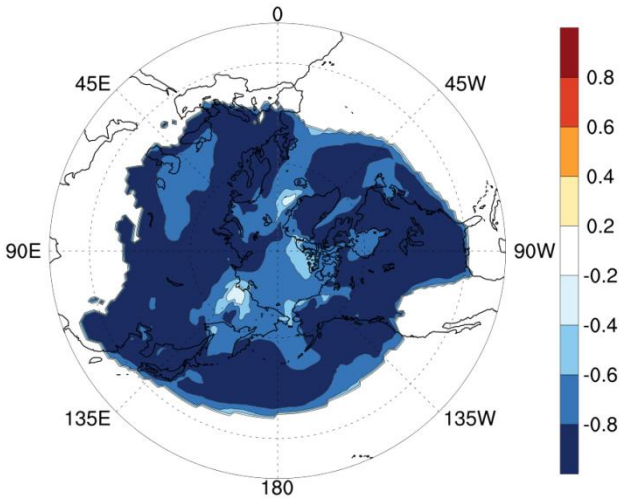


Figure 3.9 Interannual correlation coefficients between the detrended PCAM amount and surface air temperature at 2 m.

### 3.5.2 Does Arctic Oscillation play any role?

The remarkable correlation between $\langle DP \rangle$ and ENSO raises questions about the influence of extratropical variability on the PCAM. Here, we briefly discuss the possible role of Arctic Oscillation (AO) since AO is one of the largest modes of extratropical climate variability (Thompson and Wallace 1998). However, it turns out that the AO index shows almost zero correlation with the variation of $\langle DP \rangle$ ($r$ = -0.05). To reveal the reasons for this finding, we

calculate the $\langle DP \rangle$ budget and spatial correlation/regression analyses on the AO index (Figure 3.10). The positive phase of the AO indicates a strengthening of the polar vortex, which hinders the outflows of the PCAM at mid-latitudes. It is evident that the zonal-mean cold air outflow at 45°N decreases significantly (Figure 3.10a). The decrease in outflow is associated with an increase in the PCAM in the genesis box and thus results in the lengthening of the PCAM residence time. According to the budget equation, the weaker outflow contributes to the decrease of 3.31% in $\langle DP \rangle$ and the longer residence time contributes to the increase of 3.04% in $\langle DP \rangle$. Their effects are almost balanced. Meanwhile, the influence of the anomalous PCAM life time in the loss box is still very minor (0.11%). By combining all budget terms, the AO results in only a 0.16% change in $\langle DP \rangle$, which is nonsignificant and much smaller than the influence of ENSO. Therefore, the AO has no correlation with $\langle DP \rangle$ because of the balance between the effects of equatorward outflow and residence time.

It should be noted that AO does have a strong influences on the PCAM distribution although its influence on the total hemispheric PCAM amount is not apparent. The positive phase of the AO enhances the circumpolar westerly PCAM flux and causes PCAM anomalies across the extratropics (Figs. S9b,c). In a general view, the same seesaw pattern of the PCAM anomalies between the western and eastern hemispheres is the reason for nonsignificant influence of the AO on the total hemispheric PCAM amount. The cold air along the North American stream seems to outbreak earlier at approximately 60°N,90°W and then turns eastward toward the North Atlantic and Europe. This condition causes an increase in the PCAM over northeastern Canada and the northern North Atlantic. The outbreak at high latitude causes lesser outflow over mid-latitude North America and therefore, the PCAM over the eastern U.S. decreases. In Asia, the East Asian stream at mid-latitude weakens and causes negative PCAM anomalies. It appears that the anomalous zonal-mean PCAM outflow at 45°N is dominated by meridional PCAM fluxes over the continents. This is quite different from that shown by ENSO where the change in mid-latitude outflow is dominated by the flux over the North Pacific. The strong ocean feedback through diabatic heating is not apparent during the AO, which could be the reason for the balance in the budget analysis.

**a** Influence of AO on two-box model

| Variable name | Linear change during positive AO phase | Contribution to PCAM change |
|---|---|---|
| Cold air outflow at 45°N | -3.28x10$^{9}$ kg s$^{-1}$ | -7.26x10$^{15}$ kg (-3.31%) |
| Residence time in genesis box | +0.77 day | +6.66x10$^{15}$ kg (+3.04%) |
| Life time in loss box | +0.02 day | +0.25x10$^{15}$ kg (+0.11%) |
| Net PCAM change | | -0.36x10$^{15}$ kg (-0.16%) |

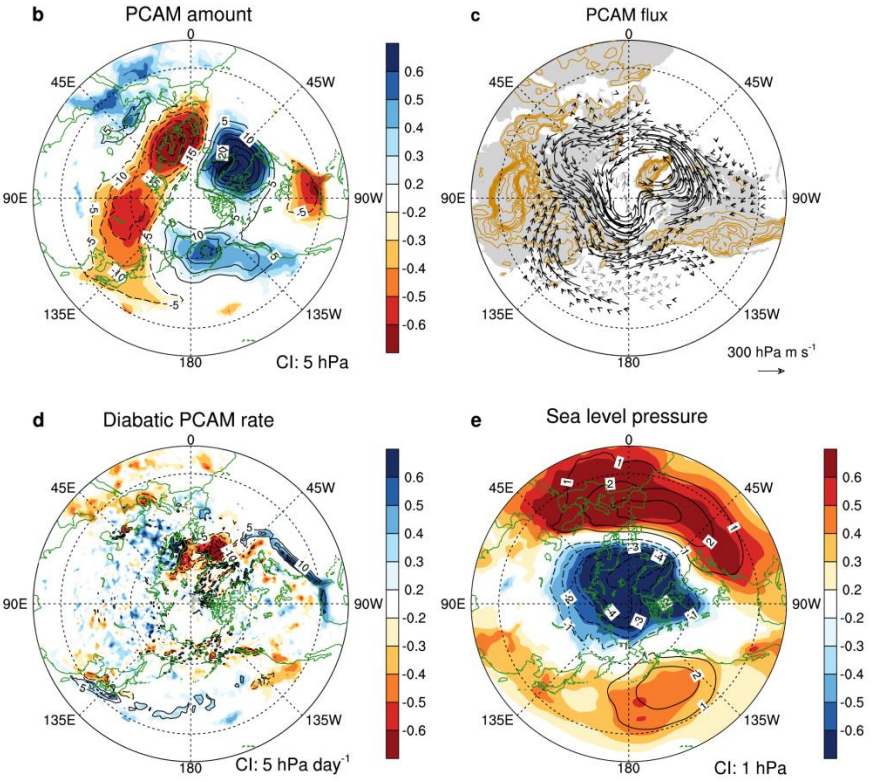


Figure 3.10 Influence of Arctic Oscillation on the northern hemispheric PCAM. (a) Influence of AO explained by the two-box model. (b-d) As in Figs. 2a-c, but using AO index. See Section 4.2 of the main paper for discussion.

### 3.5.3 Sensitivity to threshold potential temperature

Here, we discuss the sensitivity of our main result to the threshold potential temperature of PCAM. Two colder thresholds (270 and 275 K) and one warmer threshold (285 K) are assessed. Changes in the correlation between ENSO and total PCAM amount are shown in the second column of Table 3.2. Our choice (280 K) shows the strongest correlation ($r$ = -0.66) among the selected thresholds. The correlation slightly weakens when the threshold is changed to 275 K or 285 K ($r$ ~ -0.58). A much colder threshold of 270 K largely decreases the correlation although it is still statistically significant at 5% ($r$ = -0.39).

The change in the threshold consequently affects the distribution of background PCAM (Iwasaki et al. 2014). Kanno et al. (2015b) showed that, in the two-box model, the boundary between the genesis box and the loss box (i.e., a critical latitude where the climatology of zonal-mean outflow is maximum) is rather sensitive to the threshold. A colder threshold exhibits poleward shift in the critical latitude and *vice versa* for a warmer threshold (the 3rd column of Table 3.2). This change in the critical latitude may cause dissimilarity in the two-box model diagnosis. The right columns of Table 3.2 summarize the budget analysis of $\langle DP \rangle$ for each threshold (for a better comparison, here the percentages are the anomalies normalized by standard deviation of the corresponding $\langle DP \rangle$). For 275 and 285 K thresholds, the largest contributor for PCAM reduction comes from the changes in the residence time (Term 2). These are consistent with that shown by 280 K. Nevertheless, the 270 K shows a distinct pattern. The residence time lengthens and yields a positive effect while the equatorward outflow (Term 1) weakens and causes a negative effect. Regardless, Term 1 outweighs Term 2 and eventually also results in the same pattern with the other thresholds: a significant negative $\langle DP \rangle$ anomaly.

The reason for these differences in the budget analysis can be identified by investigating their PCAM patterns (Figure 3.11). For 275 K, the critical latitude shifts northward to 53.75°N. At this latitude, the effect of enhanced Aleutian Low is weakly observed (Figure 3.11, middle). Therefore, the term relating to the equatorward ouflow for 275 K shows only 2% increase. For the 270 K, the critical latitude moves further north at 60°N. In the North Pacific, PCAM flux anomalies are not clear at all (Figure 3.11, top). Therefore, at this critical latitude, the anomalies of equatorward ouflow are mainly attributed by southerly anomalies in the east of Rockies which explain the negative contribution of equatorward outflow in Table 3.2.

In summary, we conclude that the impact of ENSO and its mechanism is not sensitive to threshold change within +/- 5 K. Our threshold choice (280 K) appears to be the best one that is associated with ENSO. For a -10 K difference, ENSO still exhibits negative correlation with the total PCAM although the mechanism derived from the two-box model is rather different due to the large shift in the critical latitude.

Table 3.2 Sensitivity to several threshold potential temperatures. The 2nd column shows correlation coefficients between Niño-3.4 index and $\langle DP \rangle$. The 3rd column shows the critical latitude used in two-box model. The 4th-6th columns show the first three terms of $\langle DP \rangle$ budget normalized by standard deviation of $\langle DP \rangle$. The 7th column shows the summation of the three terms. See Text S2 for further explanation.

| Threshold theta | *r*(Nino-3.4 and $\langle DP \rangle$) | Critical latitude[1] | *Term 1* $\Delta I$ | *Term 2* $\Delta\tau_1$ | *Term 3* $\Delta\tau_2$ | *Total (1+2+3)* |
|---|---|---|---|---|---|---|
| **270 K** | -0.391* | 60°N | -39% | +14% | -16% | -41% |
| **275 K** | -0.586** | 53.75°N | +2% | -34% | -26% | -59% |
| **280 K** | -0.660** | 45°N | +73% | -123% | -19% | -69% |
| **285 K** | -0.581** | 41.25°N | +97% | -144% | -14% | -61% |

*Significant at 5%, **Significant at 0.1%,

[1]Critical latitude is a boundary between the genesis box and the loss box following the definition given in Kanno et al. (2015b).

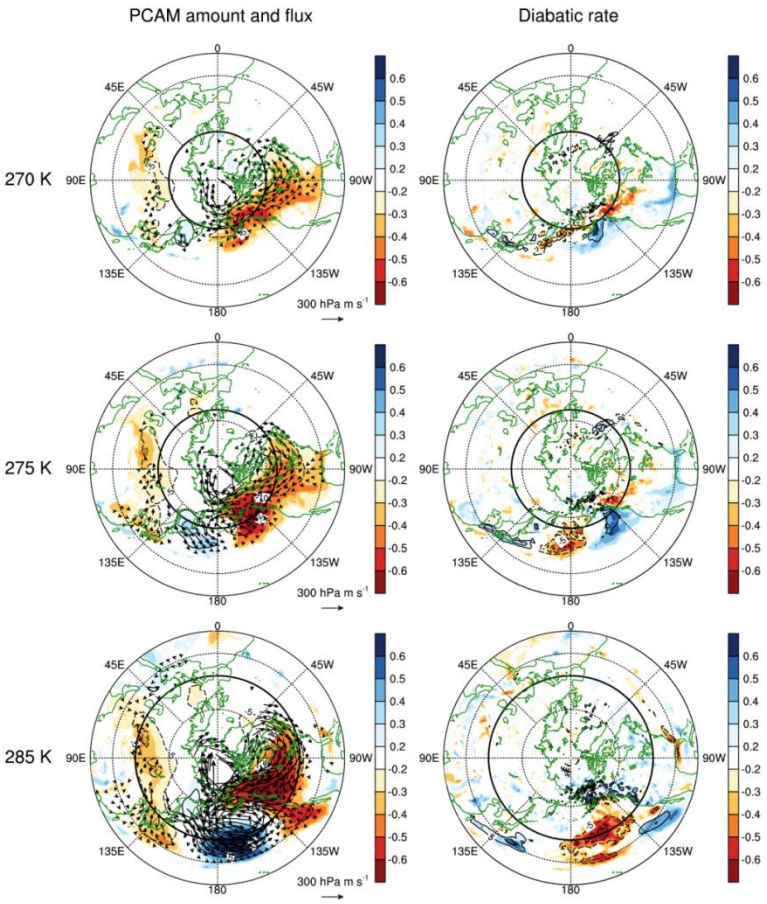


Figure 3.11 ENSO-induced PCAM patterns for three additional thresholds (270 K, 275 K, and 285 K) assessed in Text S2. The panels show correlations/regressions of PCAM amount, flux and diabatic rate with Niño-3.4 index. They are comparable with Figs. 2a-c in the main paper. Thick circumpolar lines denote the critical latitudes of the two-box model. See Text S2 for further explanation.

## 3.6 **Conclusion**

This chapter documents a strong connection between the total hemispheric PCAM amount and ENSO. The correlation coefficient between the detrended total PCAM and Nino-3.4 index reaches -0.66 over 36 recent winters. According to the zonal-mean two-box model, the primary reason for the smaller PCAM amount during El Niño events is due to the shorter PCAM residence time in the genesis box. The geographical patterns reveal that the reduction in residence time is mainly caused by the migration of the PCAM from North America to the North Pacific, which is controlled by the intensified Aleutian Low associated with PNA-like patterns. Due to the migration, the equatorward outflow of the PCAM intensifies over the North Pacific and increases the oceanic PCAM amount. However, the increase in the PCAM is quite small because the equatorward flux anomaly is situated over the warm ocean. In summary, the migration of the PCAM during El Niño causes rapid disappearance of the PCAM and eventually the imbalance in the total hemispheric PCAM amount. The resemblance between PCAM pattern and surface air temperature pattern indicates the notable impact of PCAM anomalies on the surface.

PCAM anomalies are sensitive to the ENSO teleconnection patterns that control the direction and location of PCAM fluxes. Some studies documented that ENSO teleconnection patterns have evolved and changed over decadal/multidecadal time scales (Diaz et al., 2001; Kodera, 2010; Trenberth & Hurrell, 1994) and thus may affect the long-term ENSO-PCAM relationship. The influence of nonlinearity between El Niño and La Niña teleconnections (Diaz et al., 2001; Hoerling et al., 1997) on the PCAM distribution is also of interest for future research. The potential role of the stratosphere in the polar climate response to ENSO (Ineson & Scaife, 2009) is also worth exploring. Lastly, potential connections between the PCAM and other modes of variability in the tropics and extratropics should be examined to better understand the variability of the northern hemispheric PCAM.

We show that the utilization of isentropic coordinates to diagnose the PCAM is quite simple yet it reveals a substantial impact of ENSO on the polar climate. The variation of the PCAM amount affects extratropical surface air temperatures (Abdillah et al., 2017, 2018; Kanno et al., 2017; Shoji et al., 2014). The variation of the equatorward PCAM flux potentially indicates changes in cold air outbreak events (Abdillah et al., 2017, 2018; Kanno et al., 2017) and may play an important role in wintertime weather and climate in the associated regions. As our result highlights the significant remote impact of ENSO, climate modelers can use PCAM amounts and its associated variables to better evaluate the performance of global climate models when simulating tropical-polar teleconnections.

# 4. Influence of El Nino Southern Oscillation on interannual variability of East Asian cold air outbreak

## 4.1 **Introduction**

The Northern Hemisphere exhibits two cold air streams: East Asian (EA) stream and North American (NA) stream (Figure 2.2b; Iwasaki et al. 2014). These streams indicate major pathways of equatorward outflow of PCAM. Under the influences of stationary ultra-long waves induced, the primary outflows occur over the east of Tibetan Plateau and the east of Rocky Mountains. The magnitudes of the streams are associated with composites of many cold air outbreaks (CAOs) that frequently occur on those regions (Garreaud 2001; Shoji et al. 2014). The CAOs release cold waves and can induce severe wintertime weather that are harmful for society (Cellitti et al. 2006).

Changes in the streams potentially affect the behaviour of CAOs. This chapter documents the variability of EA stream on interannual time scale and its association with ENSO. Previous studies have investigated that ENSO plays a role on East Asian winter, where the El Nino tends to cause warm winter and La Nina causes cold winter (e.g., Wang et al. 2000). However, they mostly discussed the impact on surface air temperatures. Here, we present the association between ENSO and the leading modes of East Asian stream/CAO. Exploring the impact of ENSO on several modes of variability is expected to improve our understanding on ENSO roles over East Asia. As an additional reference, the variability of NA stream has been discussed in a separated study by Kanno et al. (2017) .

## 4.2 **Data and method**

We use atmospheric variables from the Japanese 55-year Reanalysis (JRA-55) dataset, which has 6-hourly time resolution, 1.25°×1.25° horizontal resolution and 37 vertical pressure levels (Kobayashi et al. 2015). The monthly precipitation data is the Global Precipitation Climatology Project (GPCP) dataset provided by NOAA/OAR/ESRL PSD, which has 2.5°×2.5°

Contents of this chapter have been published in M. R. Abdillah, Y. Kanno, T. Iwasaki, 2017: Tropical–Extratropical Interactions Associated with East Asian Cold Air Outbreaks. Part I: Interannual Variability. *J. Clim.*, **30**, 2989–3007, doi:10.1175/JCLI-D-16-0152.1.

resolution and spans from 1979 to the present (Adler et al. 2003). We use the Met Office Hadley Centre Sea Ice and Sea Surface Temperature (HadISST1; Rayner et al. 2003) as the oceanic dataset, which has 1°×1° resolution and extends from 1870 to the present. We also use several climate indices: Siberian high (SH; Gong et al. 2001), Aleutian low (AL; Overland et al. 1999), and several teleconnection patterns: Eurasian (EU; Wallace and Gutzler 1981), Western Pacific (WP; Wallace and Gutzler 1981; Linkin and Nigam 2008), and Pacific North America (PNA; Wallace and Gutzler 1981). The indices are derived from reanalysis. Artic Oscillation (AO; Thompson and Wallace 1998) index is obtained from NOAA/NCEP/CPC webpage (http://www.cpc.ncep.noaa.gov/). We average the data from December to February (DJF) to obtain winter mean. The analysis period covers 56 boreal winters from 1958 to 2013, except that analysis involving precipitation only covers 35 winters from 1979. Despite the difference in data period, we confirm that the results are consistent for both periods. The winter of 1958 refers to the DJF 1958/59.

The EA stream covers large area of East Asia and nearby ocean elongating from inland Eurasia to the North Pacific in midlatitudes (Figure 2.2b). To quantify the magnitude of EA stream, it is convenient to consider the region of maximum equatorward PCAM flux that seems to be located at 45°N, 90°-180°E (Figure 4.1a; Shoji et al. 2014). We first discuss the primary modes of EA stream by applying Empirical Orthogonal Function (EOF) technique on seasonal means equatorward PCAM flux over the mentioned region (Chapter 4.3). In the following chapter, we show that two leading EOF modes indicate two different CAO pathways, western CAO and eastern CAO, which correspond well with the previous simple CAO separation of Shoji et al. (2014) (see Chapter 2.1.3). This finding motivates us to use the previous CAO indices that are calculated from integrations of PCAM flux over two designated regions. Chapter 4.4 clarifies that the variation of seasonal mean CAO index reflects the variability of synoptic-scale CAO events. Linear regression and correlation are then used to identify climate patterns, including ENSO, that are associated with CAOs variability (Chapter 4.5). The confidence levels for correlation coefficient are calculated based on a two-sided Student's *t* test. In Chapter 4.6, we perform numerical simulation using a simple linear atmospheric model to provide dynamical evidence. Model description and configuration are shown in the corresponding section.

## 4.3 Two distinct modes of East Asian stream: western and eastern CAOs

Figure 4.1b exhibits three leading EOF modes of seasonal mean East Asian equatorward PCAM fluxes. The remarkable features are quasi-monopole structure of EOF1 and EOF2 that are located in the eastern and western side of climatological EA stream, respectively.

The intersection point between these two modes is approximately located at 135°E. The contribution of EOF1 and EOF2 is quite balance. Their explained variances are 31.1% and 28.8%, while EOF3 has only 15.6%. The rest of analysis focuses on the two leading EOF patterns.

Low-level circulation anomalies associated with EOF1 and EOF2 are shown in Figure 4.2. In extratropical region, EOF1 is characterized by negative pressure anomalies over the North Pacific (Figure 4.2a). Oceanic northerly anomalies appear over the western North Pacific to the coast of eastern Eurasian continent and sharply turn eastward north of 30°N. This pattern clearly indicates that EOF1 is controlled largely by enhanced Aleutian Low pressure system located over the North Pacific. On the other hand, EOF2 shows positive pressure anomaly over the northern Eurasian continent which is associated with developing Siberian High (Figure 4.2b). It couples with relatively small negative pressure anomaly centered at 150°E, which is located rather to the west of climatological mean of Aleutian Low. Such the eastward pressure gradient forcing leads to anomalous strong continental equatorward flux east of Tibetan plateau. In tropical region, both EOF1 and EOF2 show significant signals, but quite opposite to each other.

EOF1 and EOF2 clearly indicate two distinct pathways of East Asian CAOs located in the eastern and western sides, respectively. It suggests that the variability of EOF modes is likely represented by variations of mass fluxes integrated over the western and eastern regions, namely the western CAO (W-CAO) index and eastern CAO (E-CAO) index (equations (2.9) and (2.10)). Figure 4.3a and 4.3b show relationship between EOF2 index and W-CAO index and relationship between EOF1 index and E-CAO index, respectively. Their correlation coefficients are very high (0.95 for EOF2/W-CAO and 0.97 for EOF1/E-CAO). These indicate that both E-CAO and W-CAO indices are very accurate to represent the variability of the first two modes of East Asian stream. This finding clarifies the existence of western and eastern CAOs that were suggested by Shoji et al. (2014). Because of this consistency with the previous study, the rest of analysis uses the integrated-based CAO indices instead of the EOF-based indices. A merit of the integrated-based indices is that we are able to utilize the indices regardless of time scales. For example, the CAO indices are useful when analyzing synoptic evolution of CAO or even analyzing decadal variability of CAO.

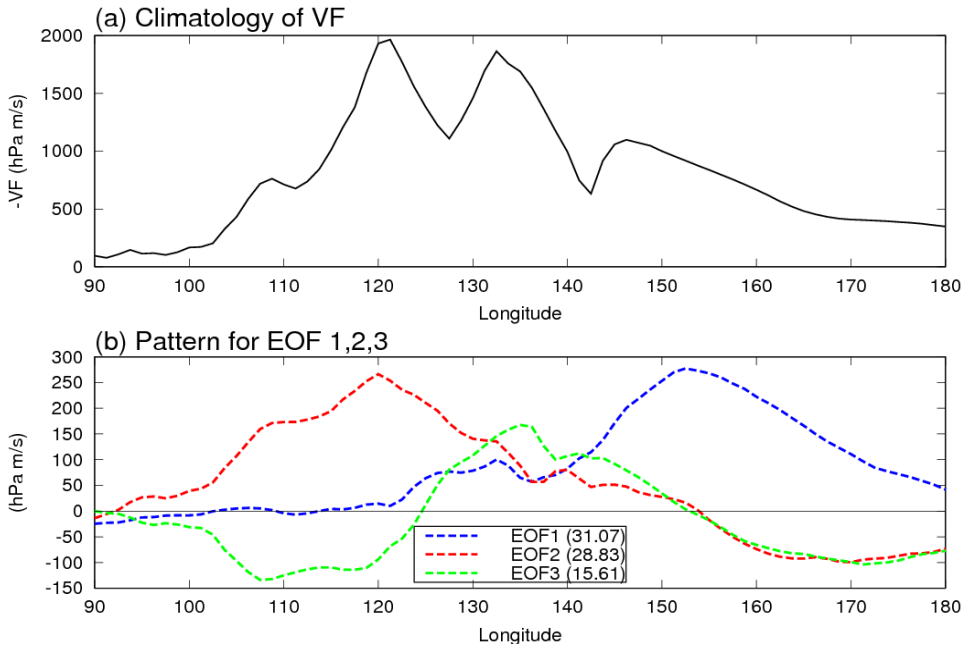


Figure 4.1 (a) Climatology of equatorward PCAM flux (unit: hPa m $s^{-1}$) along 45°N latitude. (b) Three leading EOF patterns depicted as regression coefficients of equatorward PCAM flux anomalies and the principal component indices. Blue, red, and green lines denote EOF1, EOF2, and EOF3, respectively. Percentages of explained variance for each EOF are shown in the legend.

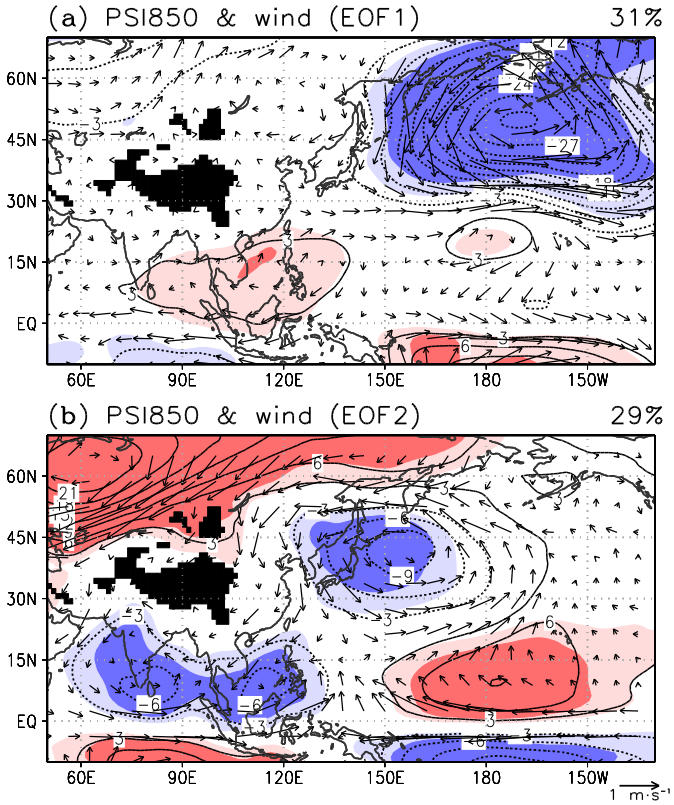


Figure 4.2 Lower tropospheric circulation anomalies associated with (a) first and (b) second EOF modes. Black contours denote regression coefficients between streamfunction at 850 hPa (PSI850) and the EOF indices ($3\times10^5$ $m^2$ $s^{-1}$ interval without zero contour). Red and blue shadings denote positive and negative correlation of PSI850, respectively. Light and dark shadings exceed 90% and 99% confidence levels of the correlation coefficients. Vector field denotes regression with anomalous horizontal wind at 850 hPa (unit: m $s^{-1}$). Black shadings indicate area where the mean surface pressure is lower than 850 hPa.

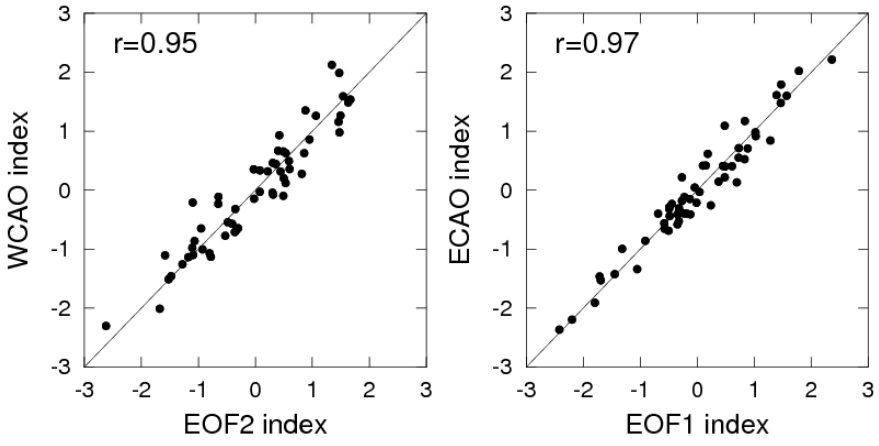


Figure 4.3 Scatterplot distribution between EOF-based indices (x-axis) and integration-based CAO indices (y-axis). Left panel shows relationship between EOF2 and W-CAO index. Right panel shows relationship between EOF1 and E-CAO index.

## 4.4 Association between seasonal mean index and CAO event occurrences

CAO event is basically a synoptic-scale phenomenon (Shoji et al. 2014). Time-averaging a CAO index in a whole winter may raise a question whether it can represent the annual frequency of the individual CAO events. Before going further into climate pattern analysis, we assess the reliability of seasonal mean CAO index in association with the CAO events.

To clarify the association, we count the number of individual CAO events in each winter (i.e., CAO frequency) and correlate it with the seasonal mean CAO index. The CAO events are identified based on local maxima of daily series of CAO index that are greater than (or equal to) 1.5 standard deviation (period 1958-2013). We find 234 W-CAO type events (annual rate 4.2 event/winter) and 207 E-CAO type events (annual rate 3.7 event/winter). To show the robustness of the CAO definition, we calculate day-lagged composite anomalies of pressure, temperature, and wind from all identified events (Figure 4.4). The lagged composites of W-CAO and E-CAO events are very consistent with the typical CAO evolution presented by lagged regressions in Shoji et al. (2014). On one hand, the W-CAO is controlled by developing Siberian High which penetrates to lower latitudes and causes significant damages over the East Asian continent. On the other hand, the E-CAO is controlled by stationary Aleutian Low that causes CAOs over the ocean. Therefore, identification of individual CAO events based on local maxima successfully depicts the typical evolution of synoptic scale CAO events

Figure 4.5 exhibits time series of frequency of CAO events and seasonal mean CAO index. Both W-CAO and E-CAO show close relationships between their individual CAO frequency and seasonal mean indices with correlation coefficients exceeding 0.75. This result confirms the association between synoptic scale CAO event and seasonal mean index. High and low winter mean CAO index indicates, respectively, more and less frequent synoptic scale CAO events. This relationship is easily achieved because the CAO definition and seasonal mean index basically uses same quantitative parameter denoted by equatorward PCAM fluxes.

.

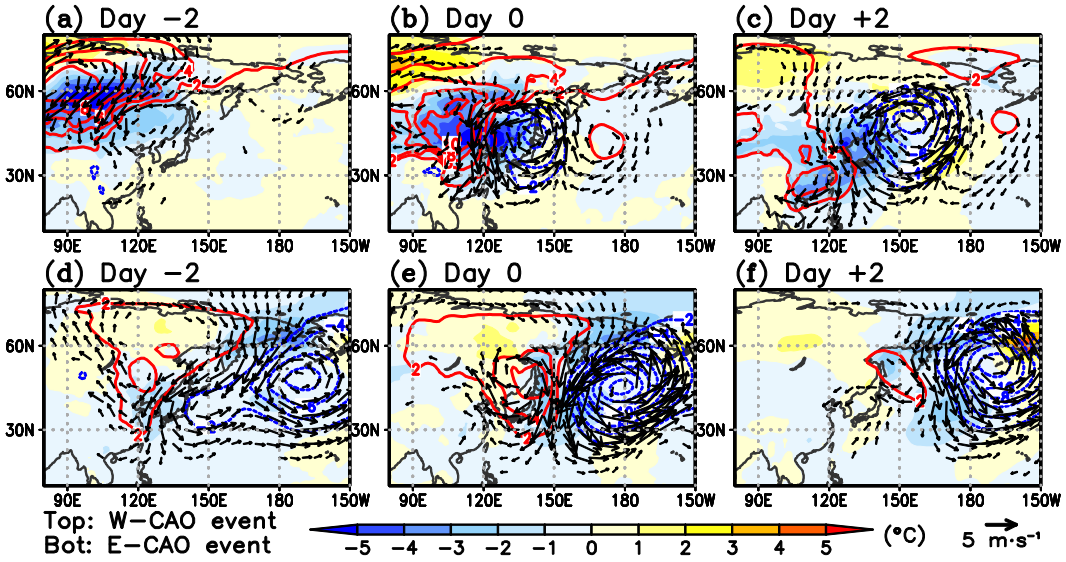


Figure 4.4 Synoptic conditions during (a-c) W-CAO event and (d-f) E-CAO event based on day-lagged composite analysis of 234 W-CAO events and 207 E-CAO events, respectively. Atmospheric field anomalies on (a,d) day -2, (b,e) day 0, and (c,f) day +2 are shown. Shaded areas denote surface air temperature (at 2 m) anomalies. Red and blue contour lines denote positive and negative anomalies of sea level pressure (2 hPa interval omitting zero contour), respectively. Vector field denotes anomalous wind field at 850 hPa level greater than 1 m $s^{-1}$.

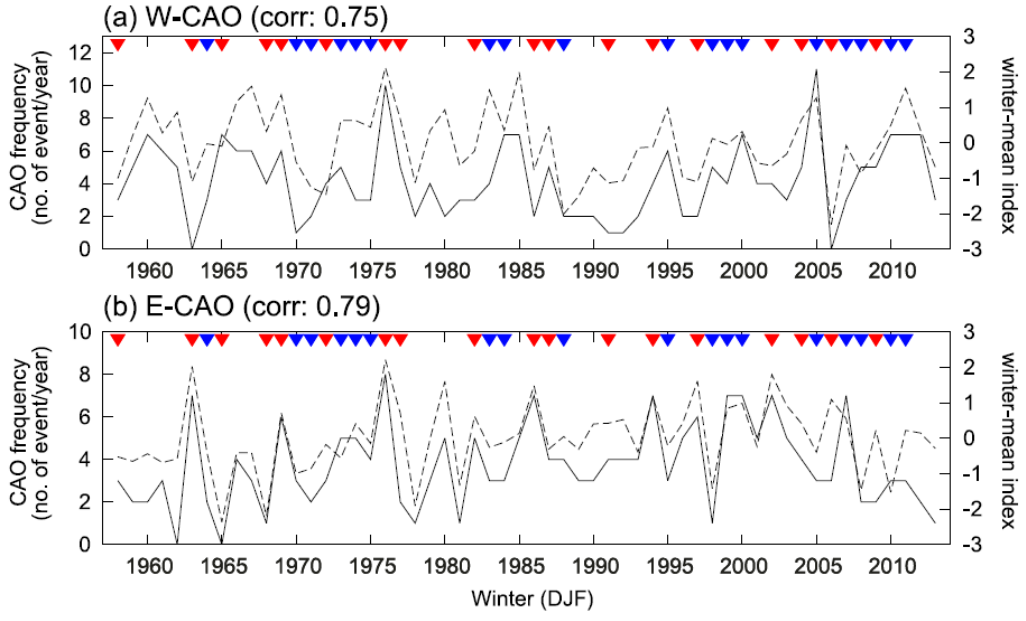


Figure 4.5 Interannual variability of annual frequency of CAO event (solid line; left axis) and normalized winter-mean CAO index (dashed line; right axis) for (a) W-CAO and (b) E-CAO. Correlation coefficients between the corresponding time series are shown in the label of each panel. Red and blue triangles indicate El Niño and La Niña events according to the definition of CPC/NOAA, respectively.

## 4.5 Climate anomalies and signatures of ENSO

### 4.5.1 Climate anomalies linked to western CAO

Figure 4.6a shows anomalies of PCAM amount and PCAM flux regressed with seasonal mean W-CAOI. The anomalous PCAM flux in Northern Eurasia resembles a large anticyclonic circulation anomaly. The flux is dammed up by Tibetan plateau, yielding significant northerly and northwesterly flux anomaly in East Asia. This equatorward flow results in a meridional contrast of PCAM amount across East Asia. Decreasing PCAM extends along the Ural Mountains and Eastern Siberia to the north of Eurasian continent, while increasing PCAM exists from the South of Siberia to Southern China and Japan. The negative PCAM anomaly over northern Siberian seems weaker compared to positive PCAM anomalies exerted in mid-latitude East Asia, indicating a great diversity in the origin of cold air mass in the CAO events.

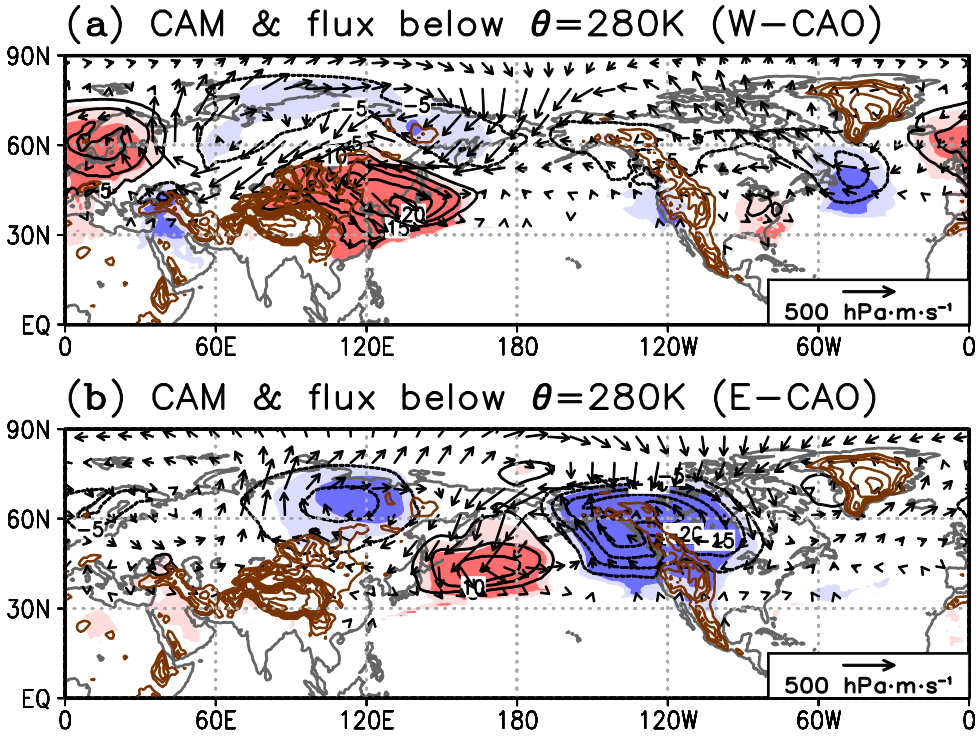


Figure 4.6 Interannual variability of northern hemispheric PCAM associated with (a) W-CAO and (b) E-CAO. Black contours depict regression coefficients of PCAM amount and the CAO indices (contour interval 5 hPa; zero line omitted). Light and dark shadings exceed 90% and 99% confidence levels of correlation coefficient of PCAM. Arrows indicate regression coefficients of PCAM flux anomaly (hPa m $s^{-1}$). Brown contours denote the topography higher than 1000 m with 500 m interval.

The signatures of W-CAO on sea level pressure (SLP), surface air temperature (SAT), 500 hPa geopotential height (Z500), and precipitation field are shown in Figure 4.7. Correlation coefficients between W-CAOI and selected climate indices are shown in Table 4.1. The strengthened Siberian high (SH) is evident (Figure 4.7a). The anomalous high pattern is geostrophically consistent with anomalous PCAM fluxes in previous figure. Correlation coefficient between interannual variability of W-CAO and SH index is 0.79, far exceeding 99.9% confidence level. Strong W-CAO winter shows significant drop of SAT from mid-latitude to subtropical East Asia and the western North Pacific (Figure 4.7b). In the middle troposphere, the negative anomaly of East Asian trough is shown, and some extratropical teleconnections are clearly observed (Figure 4.7c). The W-CAO shows wave train-like height anomaly stretching from Europe to East Asia, resembling positive phase of Eurasian teleconnection pattern (EU; Wallace and Gutzler 1981). Meridional dipole-like anomaly between Eastern Siberian and North Pacific resembles negative phase of western Pacific teleconnection pattern (WP; Linkin and Nigam 2008). Correlation coefficient between W-CAO and EU/WP index is 0.75/-0.45, exceeding 99.9% confidence level. Arctic Oscillation (AO; Thompson and Wallace 1998), as one of the strongest variability in the north pole, also has significant relationship with W-CAO ($r$ = -0.47). The correspondence of W-CAO features with EU, WP, and AO signals indicates the contributions of extratropical variabilities to W-CAO.

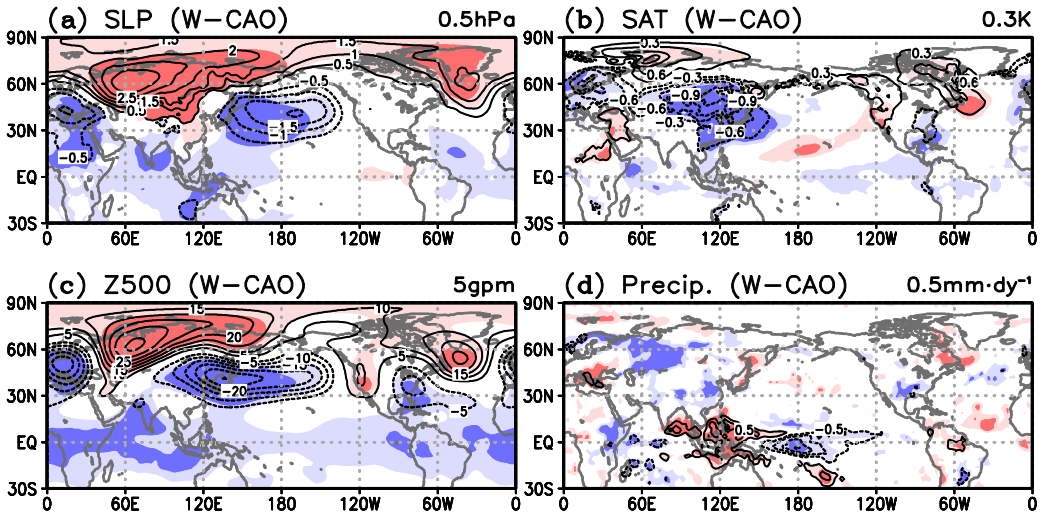


Figure 4.7 Anomalies of (a) sea level pressure (SLP), (b) surface air temperature (SAT; at 2 m), (c) mid-tropospheric geopotential height (Z500), and (d) precipitation associated with W-CAO. Black contours are regression coefficient between W-CAOI and each variable with intervals: (a) 0.5 hPa, (b) 0.3 K, (c) 5 gpm, and (d) 0.5 mm day$^{-1}$, respectively. Light and dark shadings exceed 90% and 99% confidence levels of its correlation coefficients. Zero contour lines are omitted.

Table 4.1 Correlation coefficients between East Asian CAO indices (W-CAOI and E-CAOI) and selected climate indices. Single (*) and double (**) asterisk denote 95% and 99.9% confidence levels.

| Climate index | W-CAO | E-CAO | Reference |
|---|---|---|---|
| SH | 0.79** | 0.03 | Gong et al. (2001) |
| AL | -0.35* | -0.75** | Overland et al. (1998) |
| EU | 0.75** | 0.04 | Wallace and Gutzler (1981) |
| WP | -0.48** | 0.01 | Wallace and Gutzler (1981) |
| AO | -0.47** | 0.08 | Thompson and Wallace (1998) |
| PNA | 0.28* | 0.77** | Wallace and Gutzler (1981) |
| Niño-3 | -0.28* | 0.35* | SST (5°S-5°N, 150°-90°W) |
| TIO | -0.35* | 0.31* | SST (10°S-10°N, 40°-90°E) |

In the tropics, negative geopotential height anomaly spreads throughout the equatorial regions (Figure 4.7c) and nearly overlaps with the negative SLP anomaly field (Figure 4.7a). Dry anomalies in the precipitation field are visible over the central Pacific and Indian Ocean, while a large-scale wet anomaly is pronounced over the Maritime continent (Figure 4.7d). In the viewpoint of global mass-weighted meridional circulation, the ETD circulation over midlatitudes seems to enhance due to contribution of enhanced equatorward flow in East Asia (Figure 4.8a). Around the equatorial region, the W-CAO appears to be associated with weakening of northern global Hadley cell. Observational and diagnostic analyses have shown that ENSO largely affect the hemispherically symmetric variability of Hadley cell, which tends to intensify in El Niño events and weaken in La Niña events (Seager et al. 2003, 2005). The zonal variation of precipitation anomalies over the Indo-Pacific indicates the enhancement of two Walker circulations in Indo-Pacific region, which is also robust in 200-hPa velocity potential anomaly field (Figure 4.8b). The anomaly of divergent wind field at the upper level shows enhanced local Hadley circulation over the western Pacific but weakening one over the central Pacific. These signatures over the tropics quite resemble the major atmospheric response to a cool phase of ENSO event (i.e., La Niña). Over the Pacific basin, ENSO plays major roles in the variability of local Hadley cell over the western and central Pacific (Wang 2004). The significant signals over the tropics suggest that ENSO may play prominent role in W-CAO variation.

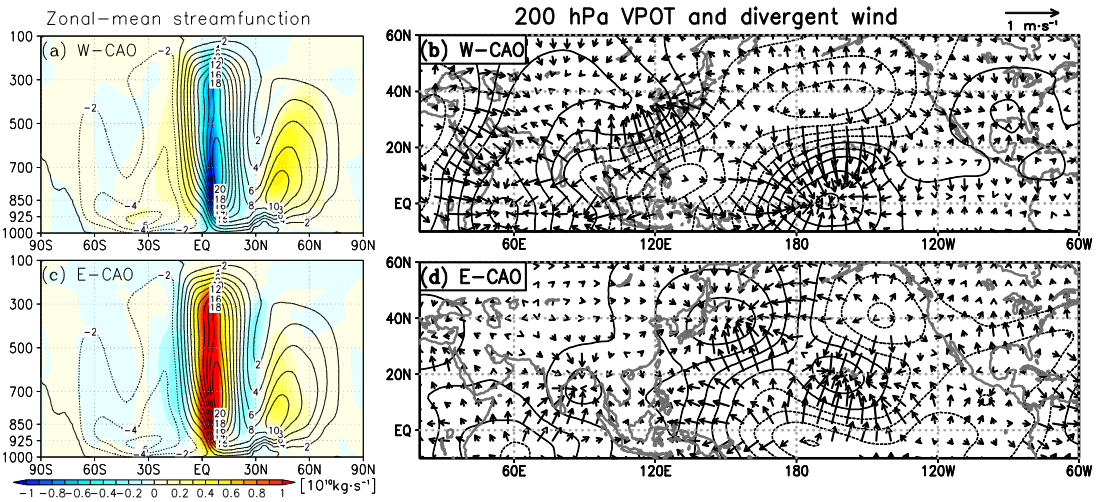


Figure 4.8 Left panels show regression between mass streamfunction of meridional circulation (calculated from mass-weighted isentropic zonal-mean) with (a) W-CAO and (c) E-CAO index (shaded; $0.1\times10^{10}$ kg $s^{-1}$ interval). Black contours in (a) and (c) denote winter climatology of mass streamfunction with $2\times10^{10}$ kg $s^{-1}$ interval. Right panels show regression between 200 hPa velocity potential (contour; $2\times10^{5}$ $m^2$ $s^{-1}$ interval) with (b) W-CAO and (d) E-CAO index, respectively. Vector field indicates divergent wind.

### 4.5.2 Climate anomalies linked to eastern CAO

Figure 4.6b shows the anomaly of PCAM amount and PCAM flux associated with E-CAO winter. In contrast to W-CAO, the positive and negative PCAM anomalies of E-CAO tend to distribute zonally rather than meridionally. The increasing PCAM is observed mainly over the western North Pacific, and coincided with the northerly anomalies. On the other hand, an enormous decrease of PCAM is seen over eastern North Pacific and western North America, overlapped with southerly flux anomalies. Figure 4.9a shows an anomalous cyclonic circulation over North Pacific corresponding to the strengthening of Aleutian low (AL). The correlation coefficient between E-CAOI and AL index is -0.75, far above 99.9% confidence level (Table 4.1). Yet, the correlation with Siberian high index is very small. The distribution of temperature anomalies (Figure 4.9b) is quite consistent with PCAM anomalies. Negative temperature anomalies over East Asia are less prominent compared to those observed in W-CAO. However, high positive temperature anomalies prevail particularly over western North America due to substantial loss of CAM. Figure 4.9c shows geopotential height anomalies in mid-troposphere. A northeastward wave trains-like pattern extending from subtropical central Pacific to North America resembles the positive phase of Pacific North America (PNA) teleconnection pattern (Wallace and Gutzler 1981). The correlation coefficient of E-CAOI with PNA index indeed shows a significant relationship between E-CAO and PNA ($r$ = 0.77; Table 1).

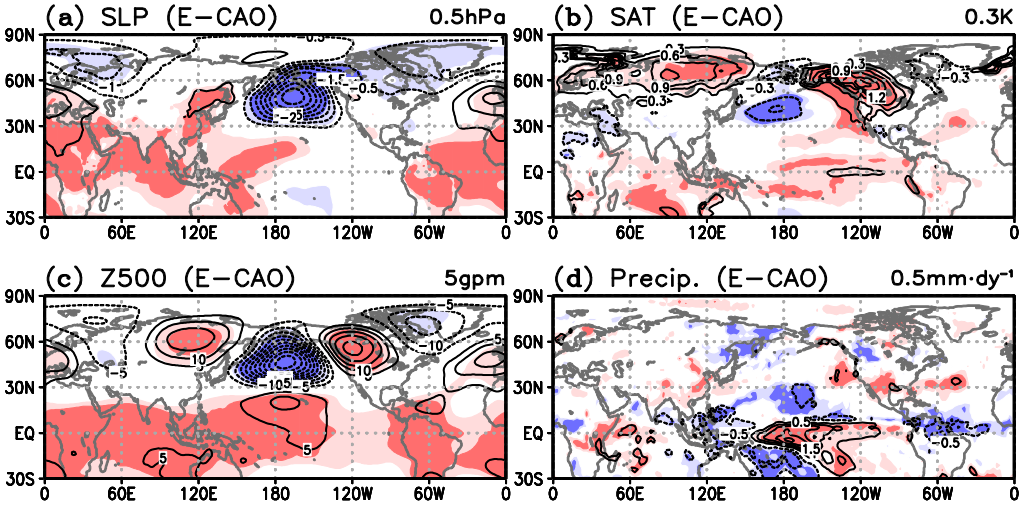


Figure 4.9 As in Fig. 4.7, but for E-CAO.

Although W-CAO has a greater impact on East Asian temperature compared to E-CAO, the impact of E-CAO on precipitation should not be negligible, particularly over Japan area (Figure 4.10). Mountainous region in the center of Japan archipelago causes distinct precipitation response to W-CAO between Japan Sea side (northern coast) and Pacific side (eastern and southern coast) (Figure 4.10a). In Japan Sea side, the northwesterly flow is blocked by the mountain, which consequently induces precipitation and causes snowy winter around the region. The eastern and southern Japan experience less precipitation under this condition. On the other hand, E-CAO causes less precipitation over northeastern Japan, but more precipitation over eastern and southern Japan (Figure 4.10b). This finding highlights the importance of E-CAO on the increasing precipitation over the Pacific side of Japan. It is worth noting that, in short time scale, cold air mass coming from the Pacific Ocean (resembling E-CAO-like events) can be a driving factor for extreme snowfall events in the eastern Japan (Yamazaki et al. 2015).

In tropical region, positive anomalies associated with E-CAO are evident in geopotential height and SLP fields (Figure 4.9a,c). Tropical precipitations are enhanced over the central Pacific and reduced over the Maritime Continent (Figure 4.9d), which in turn weaken the Walker circulation (Figure 4.8d). Large upper level divergence over the central Pacific strengthens the overlaying local Hadley cell, which contributes to the intensification of global Hadley circulation (Figure 4.8c,d). These results confirm that the E-CAO is also closely associated with the tropical climate variability, particularly El Niño-like event (Seager et al. 2003; Wang 2004).

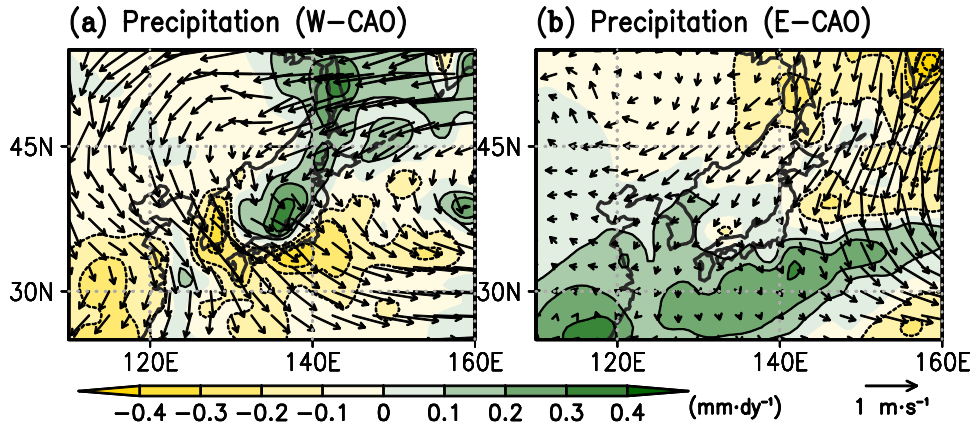


Figure 4.10 Impact of CAO on precipitation and wind field around Japan. Precipitation (shading; 0.1 mm day$^{-1}$ contour interval) and 850-hPa wind (vector) anomalies are regressed with (a) W-CAO and (b) E-CAO index.

### 4.5.3 Relationship with sea surface temperature and tropical convection

Figure 4.11a reveals SST anomaly associated with W-CAO winter. Negative SST anomalies present over off East Asian coasts, indicating oceanic response to cold air outbreaks. The anomalies span mainly from the East China Sea around 30°N to equatorial region, which represents the route of W-CAO. In tropical central and eastern Pacific, we notice a tongue of negative SST anomalies that resembles a La Niña-like pattern. This indicates the interannual variability of W-CAO is consistent with typical ENSO influence to the East Asian winter monsoon (e.g., Zhang et al. 1997), which suggests that winter monsoon tends to be stronger (weaker) during La Niña (El Niño) events, respectively. A negative correlation is also observed between W-CAO and the tropical Indian Ocean (TIO) SST. To quantify the relationship between W-CAOI and tropical SSTs, we use SST indices as areal averages over Niño-3 region (5°S-5°N, 150°-90°W) and TIO region (10°S-10°N, 40°-90°E), respectively. Correlation coefficient between W-CAOI and Niño-3/TIO index is -0.28/-0.35, satisfying 95% confidence level (Table 4.1). The SST anomaly associated with E-CAO winter is shown in Figure 4.11b. North Pacific SST exhibits a cooling structure, which is affected by equatorward cold air advection associated with the enhanced Aleutian low. In western North America, poleward advection of warm air from warm subtropical ocean yields positive SST anomalies along the off coast of North America. In the tropical region, positive SST anomalies are particularly visible over the central and eastern Pacific, showing a resemblance to El Niño-like pattern. The warm SST anomalies also appear in Indian Ocean. The E-CAOI is positively correlated with Niño-3/TIO index with a correlation coefficient value of 0.35/0.31, significant at 95% confidence level (Table 4.1).

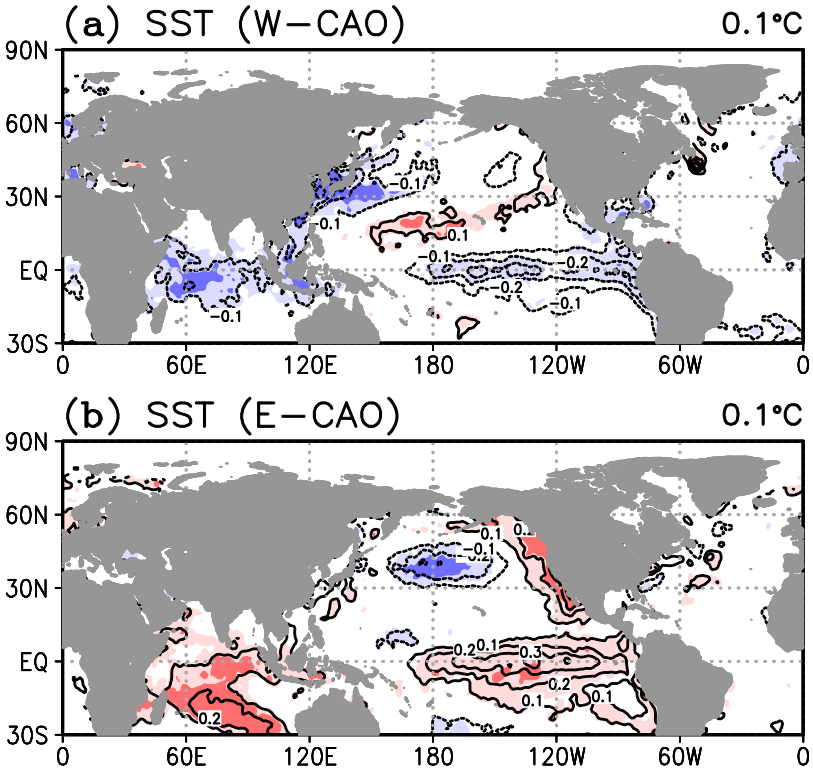


Figure 4.11 As in Fig. 5 but for SST anomalies associated with (a) W-CAO and (b) E-CAO. Contour interval is 0.1°C. Light and dark shadings exceed 90% and 99% confidence levels of its correlation coefficients.

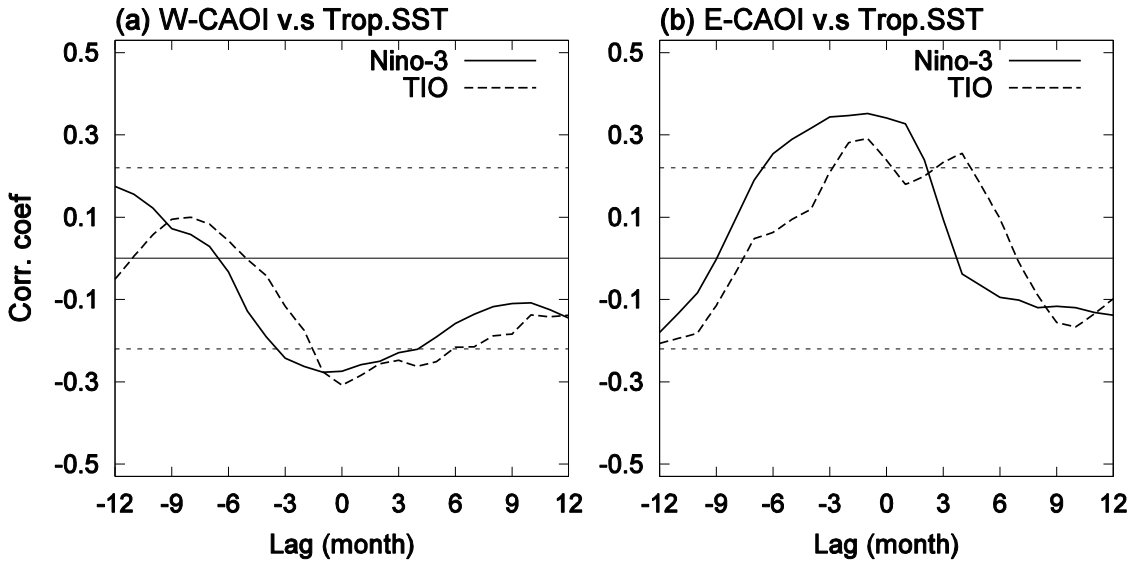


Figure 4.12 Evolutions of tropical SST anomalies prior to and post winter of (a) W-CAO and (b) E-CAO. Black solid and dashed lines denote month-lagged correlation coefficients with Niño-3 and TIO SST index, respectively. Horizontal dashed lines denote confidence level at 90%, while the horizontal solid line in the middle denotes zero correlation coefficient.

To clarify the evolution of ENSO-induced tropical SST anomalies, we calculate month-lagged correlation between CAO indices and SST indices. The monthly SST data is first smoothed by 3-month running mean and the trend is removed before calculation. Figure 4.12a shows that W-CAO winter is clearly preceded by significant eastern Pacific SST cooling that appears in autumn, reaches peak in early winter, and persists until spring. Generally, similar features are observed for E-CAO winter, but it is accompanied by eastern Pacific SST warming instead of cooling (Figure 4.12b). Note that, TIO SST evolutions follow the evolution of eastern Pacific SST with lag time of several months. These features confirm the ENSO-like SST evolution. Indian Ocean SST responds to ENSO events possibly via "atmospheric bridge" (Klein et al. 1999; Lau and Nath 2003). In W-CAO pattern, lag time between Niño-3 SST and TIO SST evolution is approximately 1-2 month. On the other hand, the lag time in E-CAO pattern is longer (2 - 4 month), showing a close resemblance to typical ENSO-induced Indian Ocean SST signal as noted by Lau and Nath (1996) (3 – 6 month). In addition, the simultaneous correlation coefficient of W-CAOI/TIO index is somewhat stronger than W-CAOI/Niño-3 index, unlike the pattern for E-CAO where the correlation coefficient of E-CAOI/TIO index is lower than that of E-CAOI/Niño-3 index. These may indicate that the role of Indian Ocean SST is important for enhancing ENSO impact to W-CAO. Watanabe and Jin (2003) demonstrated atmospheric response to El Niño event using a moist linearized atmospheric model with and without Indian Ocean SST anomaly. The El Niño-induced SST warming over the Indian Ocean was found important to amplify the suppression of convection over the Maritime Continent through changes in the Walker circulation associated with the anomalous diabatic heating over Indian Ocean (Watanabe and Jin 2003). In the lower troposphere, they showed that the suppression of convection over the Maritime Continent induces subtropical Philippine Sea anticyclone (PSA), which is suggested by Wang et al. (2000) as a mechanism why the East Asian winter monsoon tend to be warmer or weaker during El Niño. However, it seems that the PSA is not strong enough to suppress the equatorward PCAM flow in the mid-latitude. We suggest that the ENSO impact on the W-CAO is mainly delivered through upper-tropospheric response, where the Rossby wave-trains are excited due to anomalous convection over the Maritime Continent. In short, ENSO-induced TIO SST anomalies contribute to the variability of Maritime Continent convection and its upper level convergence/divergence which favor the development of Rossby wave trains in East Asia, and consequently influence W-CAO variability. The mechanism is further discussed in the following paragraphs. In the case of E-CAO, however, the appearance of Indian Ocean SST signal may be solely associated with ENSO and unnecessarily connected to E-CAO variation.

Table 4.2 Correlation coefficients between precipitation indices (PRE-MC and PRE-CP) and Niño-3, W-CAOI, and E-CAOI. Values with (*) exceed 99.5% confidence levels.

| Index | PRE-MC | PRE-CP |
|---|---|---|
| Niño-3 | -0.821* | 0.904* |
| W-CAO | 0.524* | -0.427 |
| E-CAO | -0.356 | 0.521* |

ENSO is known to have global impact through atmospheric circulation anomalies, which are mainly triggered by SST-induced tropical convection anomalies (e.g., Trenberth et al. 1998). To see the direct impact of tropical convection, we build winter precipitation index for two main locations averaged over the Maritime continent (PRE-MC index; 10°S-15°N, 100°-140°E) and central Pacific (PRE-CP index; 5°S-5°N, 170°E-140°W). Both PRE-MC and PRE-CP indices are strongly correlated with Niño-3 SST index. The correlation coefficients are -0.821 and 0.904, respectively (Table 4.2). Therefore, the positive values of PRE-MC and PRE-CP resemble La Niña event and El Niño event, respectively. Correlation coefficients for PRE-MC/W-CAO and PRE-CP/E-CAO indices are quite high compared to Niño-3/CAO indices (0.524 and 0.521, respectively), satisfying 99.5% confidence level. It implies that the ENSO impacts to western and eastern CAO are better explained by forcing of convections over the Maritime Continent and central Pacific.

Figure 4.13a,b(left) reveals northern hemispheric circulation anomalies correlated and regressed with PRE-MC index. Negative anomaly of upper-level geopotential height prevails over the tropics and negative phase of PNA-like pattern appears from the central Pacific to North America, indicating La Niña-like event (Figure 4.13a(left)). In East Asia, subtropical positive height anomalies exist as upper-level Rossby response to the convection over Maritime continent. Sardeshmukh and Hoskins (1988) confirmed that, in their vorticity equations, the upper-tropospheric divergence situated in equatorial easterly wind could lead to a Rossby wave source in the subtropical westerlies. It excites subtropical anticyclonic anomaly and thus potentially delivers Rossby wave trains to the extratropics, causing change in East Asian jetstream and development of negative geopotential height over mid-latitude East Asia (i.e., East Asian trough). The anomalous cyclonic circulation triggers extratropical low-level tropospheric flow barotropically, as seen in 280 K cold air mass flow field (Figure 4.13b(left)). It shows significant positive CAM anomalies and equatorward flow over inland East Asia. These conditions are favorable for developing more W-CAO events. Negative cold air mass and anomalous poleward flow are observed in the middle of North Pacific, indicating less E-CAO events, although the amplitude is not as significant as W-CAO.

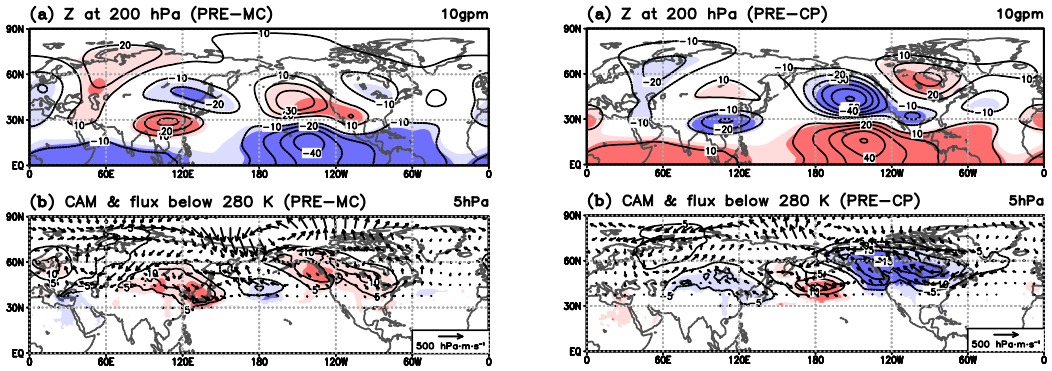


Figure 4.13 Northern hemisphere circulations regressed with (left) precipitation index over Maritime continent (PRE-MC) (10°S-15°N, 100°-140°E) and (right) precipitation index over central Pacific (PRE-CP) (5°S-5°N, 170°E-140°W). Black contours denote regression coefficients of (top) 200 hPa geopotential height with 10 gpm interval and (bottom) 280 K CAM with 5 hPa interval. Light and dark shadings exceed 90% and 99% confidence levels of its correlation coefficients. Vectors in bottom panels denote regression coefficients of 280 K CAM flux.

Over northern Eurasian continent, the EU teleconnection pattern is significantly correlated with PRE-MC index (Figure 4.13a(left)). We suggest that this signal appears not due to the impact of convection over the Maritime Continent, but rather mainly due to the impact of synoptic scale W-CAO events (associated with mid-latitude waves across EU pattern) to the tropical convection over some part of the Maritime Continent (i.e., South China Sea and Philippines). Previous studies have noted that CAO events can lead to more convection in the tropics (e.g., Compo et al. 1999). Further investigation using lagged analysis of daily data reveals that W-CAO events can both affect and be affected by tropical convections, indicating the impact and precursor of CAO. More detailed discussion about this topic will be presented in our next work. In short, the relationships in Figure 4.13a(left) may contain two-ways interactions between W-CAO and PRE-MC index. To elucidate the impact from PRE-MC, we perform simple model experiments using prescribed thermal forcing, which are presented in next subchapter. On the other hand, Figure 4.13a(right) reveals circulation anomalies associated with PRE-CP index. The PNA-like pattern is more robust compared to the pattern depicted by PRE-MC index and can be traced from central Pacific to Atlantic. The associated wave train enhances negative geopotential height in north Pacific and then strengthens the Aleutian low, which in turns induces positive cold air mass and equatorward flow anomalies around E-CAO region (Figure 4.13b(right)). In East Asia, the weakening of W-CAO is observed but less significant compared to the strengthening of E-CAO. The above results imply relative importance of Maritime Continent and central Pacific convection to the W-CAO and E-CAO events.

## 4.6 **Numerical simulations with idealized tropical heating**

Remote response of East Asian equatorward flow to the tropical convection is examined using simple linear model experiments. A linearized steady-state baroclinic model enables us to calculate the steady direct atmospheric response from a prescribed thermal forcing in a given 3 dimensional basic flow. The model is expected to provide a clear dynamical evidence of how ENSO-like convection anomalies affect equatorward flow of W-CAO and E-CAO. Using this kind of model, Hoskins and Karoly (1981) first demonstrated PNA pattern triggered by heating associated with El Niño events.

We use a dry linear baroclinic model (LBM) as in Watanabe and Kimoto (2000). It has T21 horizontal resolution with 20 $\sigma$ levels. LBM includes three dissipation terms: biharmonic ($\nabla^4$) horizontal diffusion with 6 hr *e*-folding decay time, weak vertical diffusion with damping timescale of 1000 days to suppress noises arising from finite difference, and linear drag resembling Rayleigh friction and Newtonian damping. The linear drag term is set to one day at the three lowest levels ($\sigma > 0.9$) and the two uppermost levels ($\sigma < 0.03$), and 15 or 30 days at other levels. The basic state is zonally varying climatology from 1958 to 2013 winter. In this study, three types of experiments are carried out. The first two experiments demonstrate the atmospheric response to a monopole heating centered over the Maritime Continent and the central Pacific, respectively. The third experiment uses thermal forcing with a dipole structure that mimics El Niño pattern: cooling over the Maritime Continent and heating over the central Pacific. An idealized Gaussian horizontal distribution is used for each anomalous heating center, while its vertical distribution follows sinusoidal pattern with a maxima at $\sigma = 0.36$ (4 K day$^{-1}$) and zero heating at the uppermost and lowest level. Spatial heating distribution in each experiment is denoted by grey shadings in Figure 4.14Figure 4.15. Heating over the central Pacific is set to be wider in longitude compared to heating over the Maritime Continent. Time-integration approach is used to solve the linear response in LBM (e.g., Jin and Hoskins 1995). The model is run for 30 days, yet only results at day 15 are shown here because the extratropical responses tend to be steady in about two weeks after integration.

Figure 4.14(left) exhibits the simulated atmospheric response to the heating over the Maritime Continent (first experiment). The negative geopotential height over mid-latitude East Asian coast is evidently enhanced by the poleward Rossby wave trains associated with heating over the tropics (Figure 4.14a(left)). Over the tropical region, the low-level cyclonic and anticyclonic patterns appear respectively in the northwest and northeast off to the center of heating (Figure 4.14b(left)), indicating vorticity response to the low-level convergence as shown in simple model of Gill (1980). Clear barotropic response can be seen in extratropical cold air

mass field, as well as a robust development of equatorward flow over W-CAO region (Figure 4.14c(left)). This equatorward flow transports more PCAM to most of East Asian countries. In high latitude region north of 45°N, a significant decrease of cold air mass is also evident and consistent with the observation. No signature of EU pattern is found over the northern Eurasia. It clarifies that the significant EU pattern in the regression map appears due to the impact of EU on the convection rather than the Maritime Continent convection.

The second experiment using heating over the central Pacific is quite common and has been investigated numerous times after Hoskins and Karoly (1981). Figure 4.14a(right) shows the PNA-like pattern emanating from central Pacific which is generally consistent with the past studies. Development of low-level equatorward flow over northwest Pacific is evident following Aleutian low response to the barotropic Rossby wave trains, facilitating more E-CAO events (Figure 4.14b,c(right)).

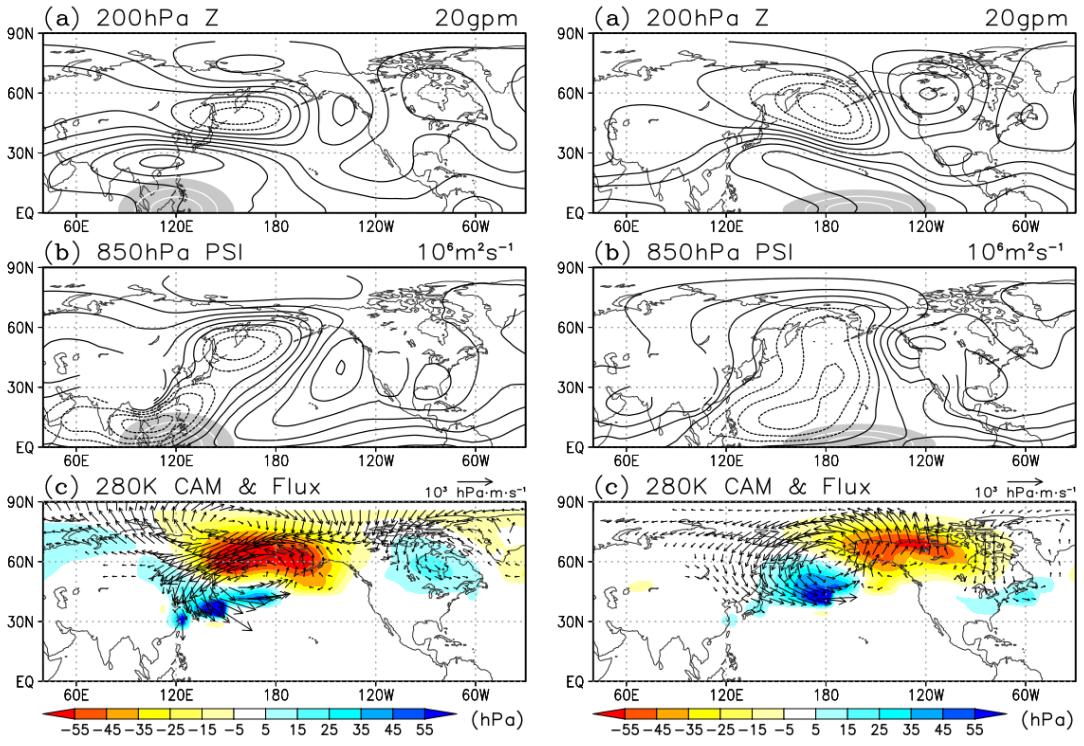


Figure 4.14 Northern hemisphere atmospheric response in the model experiment using idealized heating over (left) the Maritime Continent and (right) the central Pacific. (top) 200 hPa geopotential height (black contour; 20 gpm interval), (middle) 850 hPa streamfunction (black contour; $1\times10^6$ $m^2s^{-1}$ interval), and (bottom) CAM (shaded; 10 hPa interval) and its flux (vector) below 280 K. Grey shadings in the tropics denote positive heating anomalies at σ=0.37 model level greater than 1 K $day^{-1}$ (1 K $day^{-1}$ contour interval).

Nevertheless, the center of negative height anomaly over North Pacific (Figure 4.14a(right)) seems to shift westward compared with the regression with central Pacific precipitation shown in Figure 4.13(right). A monopole prescribed heating over central Pacific is not adequate to mimic the response during El Niño event in the dry LBM (Watanabe and Jin 2003). A suppression of convection (or cooling) over the Maritime Continent should be included to demonstrate more realistic El Niño event. Figure 4.15 exhibits the atmospheric response by including both of the central Pacific heating and the Maritime Continent cooling. Along East Asian coast to North America, the upper height response is quite consistent with the regression maps. Seesaw pattern between equatorward mass fluxes over the W-CAO and E-CAO regions is evident, confirming that El Niño events tend to suppress W-CAO and enhance E-CAO. In contrast, La Niña event (represented as central Pacific cooling and Maritime Continent heating) yields a reverse response in both of East Asian CAOs compared with El Niño.

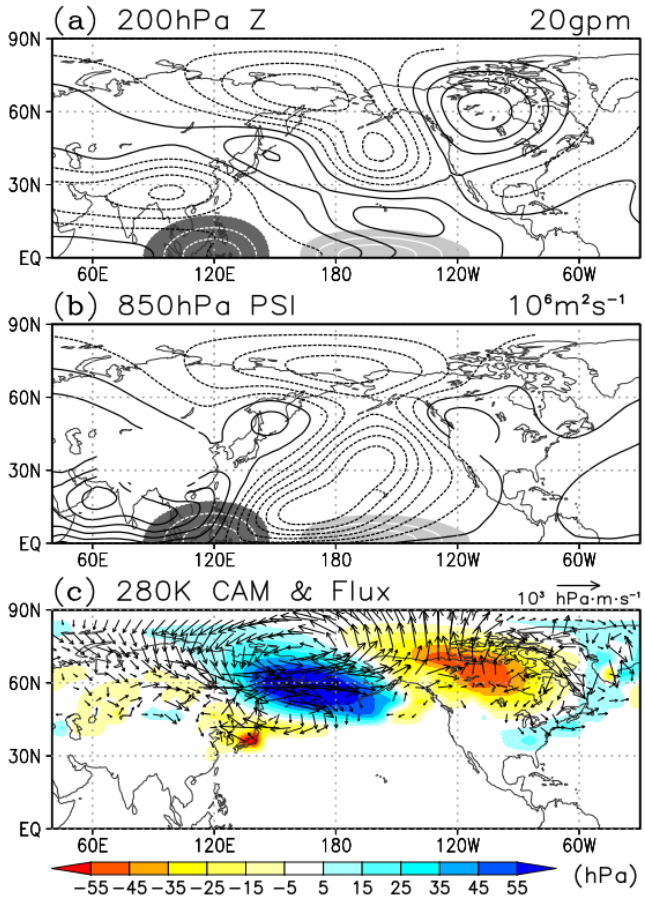


Figure 4.15 As in Fig. 4.14, but use a dipole pattern of heating anomalies: cooling over the Maritime Continent and heating over the central Pacific.

## 4.7 **Conclusion**

The winter mean East Asian CAOs exhibit two major modes, which remarkably contribute to interannual variability of East Asian equatorward flow. The first and second modes clearly depict the eastern CAO (E-CAO) and western CAO (W-CAO) types, respectively. W-CAO index, defined as equatorward flux at 45°N from 90° to 135°E, and E-CAO index, defined as equatorward flux at 45°N from 135° to 180°E, have very robust correlations with the time-series components of EOF2 and EOF1 indices ($r$ exceeding 0.95), respectively. This indicates that W-CAO and E-CAO closely represent the prominent modes of East Asian equatorward flow.

Simultaneous correlation and regression using W-CAOI and E-CAOI are used to reveal their characteristics on global climate patterns. In the extratropics, W-CAO supplies abundant amount of PCAM to the continental East Asia, and consequently causes cold winter over the region. On the other hand, E-CAO releases PCAM mostly over the western North Pacific and gives less impact on East Asian land temperature. The strong E-CAO is also associated with robust warm winter over northwest America. Differences in the signature of W-CAO and E-CAO arise from different driving forces. The W-CAO and E-CAO are closely associated with Siberian high and Aleutian low variability, respectively. These imply that using W-CAOI and E-CAOI, we can observe relative importance of zonal pressure gradient forcing in East Asian winter monsoon system. Furthermore, W-CAO and E-CAO are significantly connected with several teleconnection patterns over extratropical northern hemisphere. W-CAO winter is associated with positive Eurasian (EU), negative western Pacific (WP), and negative Arctic Oscillation (AO) patterns. On the other hand, the E-CAO is mostly associated with Pacific North American (PNA) pattern.

The W-CAO and E-CAO have distinct relationship with the tropics. W-CAO is associated with greater precipitation over the Maritime Continent, weaker global Hadley circulation, and negative SST anomalies over the tropical eastern Pacific and Indian Ocean. Stronger Walker circulations are evident and consistent with the La Niña-like events. On the other hand, E-CAO exhibits greater precipitation over the central Pacific, stronger global Hadley cell, and positive SST anomalies over the eastern Pacific and Indian Ocean. The El Niño-like events tend to induce E-CAO. These signals indicate that there are notable interactions between extratropical CAO and tropical circulation system, particularly those related to ENSO. The primary forcing of interactions between ENSO and East Asian CAO climate is tropical convections, which trigger global circulation anomalies through poleward Rossby wave trains. The main action centers of ENSO-induced tropical convection anomalies

are located over the Maritime Continent and central Pacific. Both are evidently shown to have significant relationship with the W-CAO and E-CAO variability.

It should be noted that complex dynamical system in the extratropics (i.e., internal variability) plays dominant role in the variation of East Asian CAOs. Therefore, the relationships between tropical atmosphere and CAOs may be variable depending on particular influence from internal modes in the extratropics, which is worth considered in the future study. Considering the long time span of current period of study, it is also important to note that the W-CAO and E-CAO may experience some decadal or interdecadal variations (Fig. 4). In fact, many studies have documented interdecadal feature of East Asian winter monsoon (e.g., Wang et al. 2009, 2010), which may partially exist in both W-CAO and E-CAO variation.

ENSO can explain the interannual variability of winter-mean CAO. However, it cannot explain the variation of CAO events which has a time scale about 1 week (Shoji et al. 2014). Moreover, previous studies have documented that cold surges are able to give impacts on tropical convection (e.g., Chang et al. 1979; Zhang et al. 1997). For our next work, we will focus on the interactions between CAOs and tropical weather system in intraseasonal time scale. A better understanding on this topic is expected to improve short- to medium-range forecast of both CAO events and tropical weather.

# 5. Influence of Madden-Julian Oscillation on intraseasonal variability of East Asian cold air outbreak

## 5.1 **Introduction**

Previous Chapter 4 shows the influence of tropical variability to East Asian cold air outbreaks on interannual time scale. This chapter aims to investigate whether such teleconnection appears on shorter period; for example intraseasonal or synoptic time scale. Any tropical forcing that is identified on this period would be expected to act as precursors for CAO events and therefore it can give advantage for weekly/daily CAO forecast.

One of prominent intraseasonal modes of tropical variability is the Madden-Julian Oscillation (MJO) with a typical period of 30-80 day (Wheeler and Hendon 2004). MJO is shown by large-scale eastward-moving tropical disturbance that strongly appears over Indo-Pacific. It consists of wet phase (convectively active) and dry phase (convectively inactive) which cause significant impact over the Indian Ocean, the Maritime Continent, and the central Pacific. Furthermore, like ENSO, MJO is known with its remote impacts around the globe. For example, winter precipitation over Canada is partly controlled by MJO with a time lead of one or two pentads (Lin et al. 2010). A few studies have documented the influence of MJO on temperatures and cold air outbreaks over East Asia (Jeong et al. 2005; He et al. 2011). However, their cold air outbreaks definitions were not based a quantitative approach and the results seem to be limited on particular areas of East Asia. Here, we will discuss the impact of MJO in the viewpoint of quantitative cold air outbreaks.

## 5.2 **Data and method**

This chapter employs daily dataset to depict the evolution of CAOs and its relationship with tropical intraseasonal variability. Atmospheric variables are obtained from the Japanese 55-year Reanalysis (JRA-55), which has a 6-hour time resolution, 1.25°×1.25° horizontal resolution and 37 vertical pressure levels (Kobayashi et al. 2015). Daily interpolated Outgoing

Contents of this chapter have been published in M. R. Abdillah, Y. Kanno, T. Iwasaki, 2018b: Tropical–Extratropical Interactions Associated with East Asian Cold Air Outbreaks. Part II: Intraseasonal Variation. *J. Clim.*, **31**, 473–490, doi:10.1175/JCLI-D-17-0147.1.

Longwave Radiation (OLR) is provided by NOAA/OAR/ESRL PSD (Liebmann and Smith 1996) and utilized to denote the tropical convection; it has a 1-day temporal resolution and 2.5°×2.5° horizontal resolution. As shown in the previous chapter, the East Asian CAOs exhibit two distinct modes and can be decomposed into two different types: western CAO (W-CAO) and eastern CAO (E-CAO). Intensity indices for W-CAO and E-CAO follow the equations of Shoji et al. (2014) as explained in Chapter 2.1.3.

Interannual variability associated with ENSO is excluded from the time series because the tropical atmosphere, especially convection, is highly correlated with ENSO. In addition, ENSO was found to have remote impacts on the East Asian CAOs (Chapter 4). Therefore, the influence of ENSO must be removed to emphasize intraseasonal signals in the analysis. We follow an ENSO removal procedure provided by Wheeler and Hendon (2004), except we use the monthly Niño-3 SST index (5°S-5°N, 150°-90°W) as a parameter to represent ENSO evolution. The monthly values of the Niño-3 index are converted to a daily basis. Then, a linear regression is calculated from the daily field data at each grid point, separately for each month, which results in 12 regression parameters. The monthly regression parameters are interpolated to a daily basis to yield a 365-day seasonally dependent relationship. Finally, the ENSO influence is diminished by subtracting the regression relationship of each field at each grid point.

We perform a time-lagged correlation and regression among CAOIs and field variables. In this approach, the atmospheric anomalies that precede or follow the CAO event can be determined objectively. The analysis period covers 34 winters from 1979 to 2012, in which the 1979 winter denotes 1979/80 winter. In the lagged analysis, the days of the predictand are fixed at 1 December – 28 February, and the days of the predictor depend on the lags that could be in November – March. Figure 5.1 shows results of lagged regression using unfiltered daily data showing the evolution of tropical atmosphere associated with W-CAO and E-CAO. Day 0 is regarded as the peak of CAO event. At day 0, the strongest equatorward wind anomalies appear from the midlatitudes to the subtropics. Prior to the CAO event at day -6 and day -3, both W-CAO and E-CAO tropical patterns show large-scale organized convection and circulation anomalies (Figure 5.1a,b). These patterns that appear before the event indicate potential precursors for development of CAO events. For W-CAO, the precursor pattern is large enhanced convection over the Maritime Continent and small suppressed convection over the central Pacific. For E-CAO, the precursor pattern resembles a clear dipole: enhanced convection over the western Pacific and suppressed convection over the Indian Ocean. Following the events (day +3 and day +6), there is another notable signature appeared over northern Maritime

Continent in W-CAO event. It shows development of convection which suggests an impact of CAO over the tropics. This topic will be discussed in details in next Chapter 6.

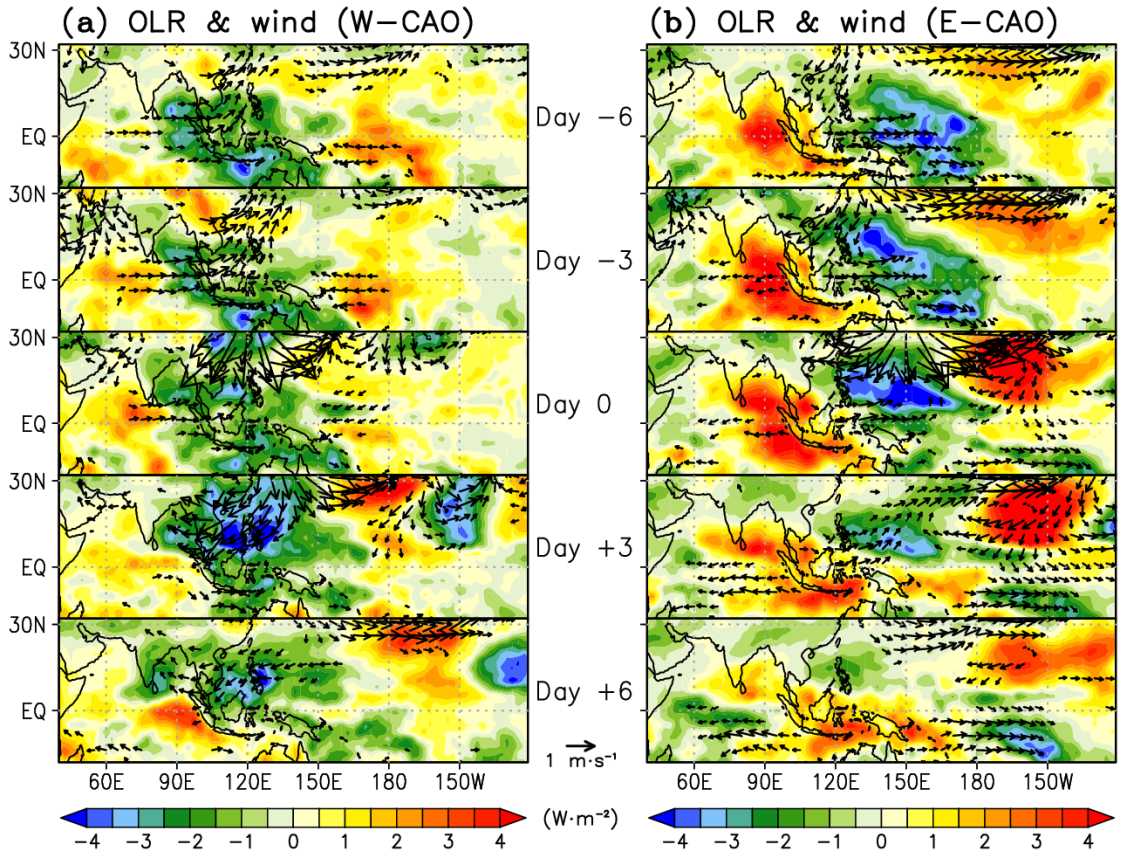


Figure 5.1 Day-lagged regressions of unfiltered tropical convection and low-level circulation onto (a) W-CAO index and (b) E-CAO index. Shading denotes OLR anomalies (contour interval 0.5 W $m^{-2}$) and vector denotes 850-hPa wind. Top panels to bottom panels show evolution from day -6 to day +6 relative to the day of CAO event (day 0).

During the course of CAO evolution, the precursor signals seem to propagate eastward in both CAO cases (Figure 5.1). These large-scale convection anomalies resemble two distinct phases of MJO. For W-CAO, the precursor pattern looks like the wet MJO over the Maritime Continent and, for E-CAO, the pattern resembles the wet MJO over the western Pacific. To focus our attention on the influences of MJO, the datasets are temporally bandpass filtered (BPF) on the typical period of MJO of 30-80 day using a Lanczos filter (Duchon 1979) from 1 November to 31 March with 320 daily weights for each winter. The 30-80-day band period is selected because 1) it is a common MJO period where the highest spectra of MJO-related tropical OLR were found (e.g., Wheeler and Hendon 2004); and 2) we find that the strongest

connectivity between leading-tropical OLR and East Asian CAO indices is observed near this band period (see Figure 5.2). If we include a high-frequency band (< 30 days), the correlations between CAOs and leading tropical OLRs are greatly reduced (Figure 5.2).

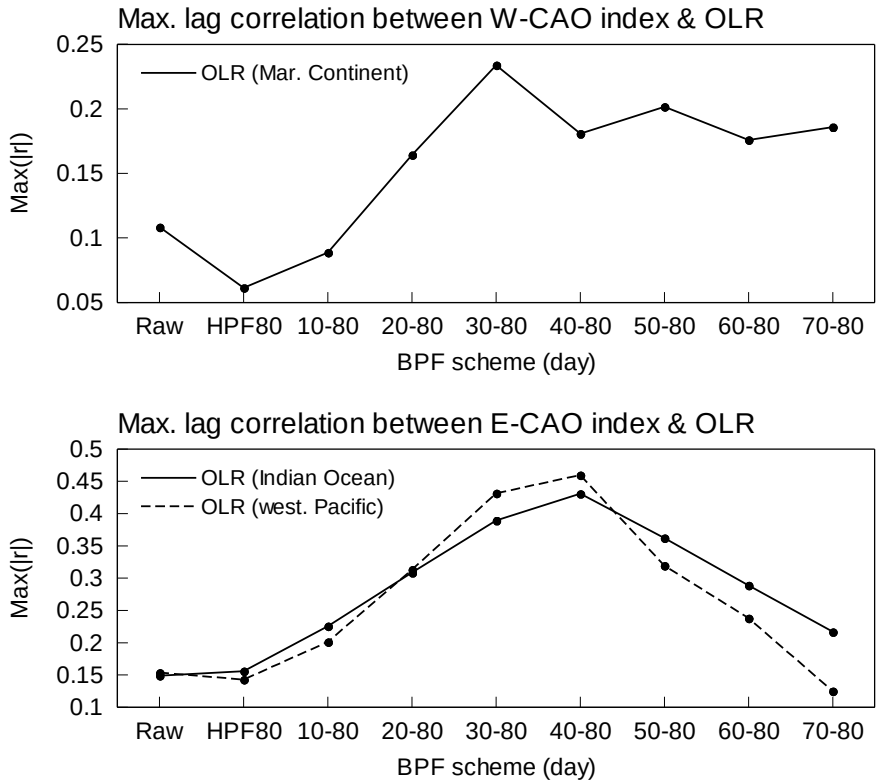


Figure 5.2 Connectivity between East Asian CAOs and tropical OLRs denoted by maximum absolute lag correlations (find a maximum from lag -10 to lag 0) between CAO indices and area-averaged OLRs for different time filter schemes. The top panel shows correlations between the W-CAO index and OLR over the Maritime Continent (100°-130°E; 15°S-15°N). The bottom panel shows correlations between the E-CAO index and OLR over the Indian Ocean (70°-100°E; 15°S-15°N) and western Pacific (140°-170°E; 15°S-15°N).

Day-to-day variations of unfiltered and 30-80 day filtered CAO indices (CAOIs) are shown in Figure 5.3a. The time interval between two adjacent peaks of an unfiltered CAOI is usually a few days to one week (Shoji et al. 2014). The autocorrelation feature of an unfiltered CAOI exhibits a clear single peak with high positive correlation persisted from approximately day -2 to day +2 in both W-CAOI and E-CAOI (Figure 5.3b). This highlights the time scale of intermittent CAO events. The synoptic conditions during the W-CAO event and E-CAO event suggest the relative importance of the Siberian high and Aleutian low, respectively (Shoji et al. 2014), which also appears in their interannual variability (Chapter 4). The W-CAO event

appears to persist in a slightly shorter time than the E-CAO , which is possibly related to the shorter lifetime of the anomalous Siberian high (because of the rapid southward progression) compared with the stationary Aleutian low (Shoji et al. 2014). In contrast, peak-to-peak time interval of a 30-80-day filtered CAOI is several weeks (Figure 5.3a). The autocorrelation feature indicates that the filtered CAOI lasts long and has significant periodicity (Figure 5.3c). Both filtered W-CAOI and E-CAOI have consistent autocorrelation features. There are two minimum peaks at lags near 20-25 days, which exhibit a -0.8 correlation coefficient. The CAOs occurred at 30-80 day period are mentioned as intraseasonal CAO events.

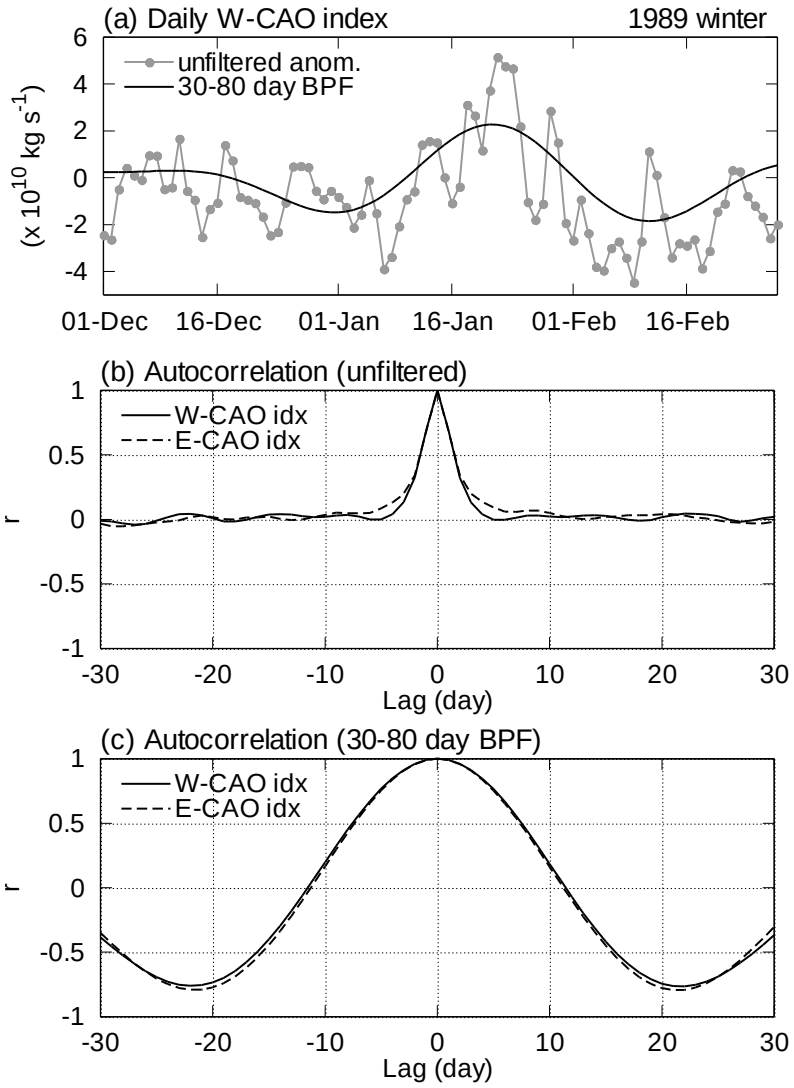


Figure 5.3 (a) Time series of unfiltered and filtered W-CAO indices in 1989 winter. (b) and (c) show, respectively, the autocorrelation properties of unfiltered and filtered CAO indices from all 34 winters.

In Chapter 5.3.3, we reconstruct an MJO cycle based on a combined lagged analysis from two leading EOF patterns of tropical OLR. This approach enables us to determine the timing of intraseasonal CAO events relative to an MJO cycle and explain its mechanism. Furthermore, we carry out several numerical experiments using a linearized GCM to demonstrate the MJO influence. Full details on the MJO cycle and model configuration are shown in Chapter 5.4. Our main discussion is the impact of MJO on intraseasonal variability of CAOs. Figure 5.2 shows that the leading tropical correlations are very small for higher frequency variability (less than 30 day) which suggests the inability of tropical forcing in determining the timing of CAO events that basically occur at synoptic time scale or shorter time scale. To check the potential role of MJO on high frequency CAOs variability, we conduct some composite analysis in Chapter 5.5.

To depict the energy propagation of quasi-stationary Rossby waves, we calculate upper-level horizontal wave activity flux (WAF) formulated by Takaya and Nakamura (2001). The horizontal WAF (**W**) is given as:

$$\mathbf{W} = \frac{\mathrm{p}\cos\phi}{2\,|\mathbf{U}|}\begin{pmatrix} \frac{1}{a^2\cos\phi}\left[\mathrm{U}\left(\frac{\partial\psi'}{\partial\lambda}\frac{\partial\psi'}{\partial\lambda}-\psi'\frac{\partial^2\psi'}{\partial\lambda^2}\right)+\frac{\mathrm{V}}{\cos\phi}\left(\frac{\partial\psi'}{\partial\lambda}\frac{\partial\psi'}{\partial\phi}-\psi'\frac{\partial^2\psi'}{\partial\lambda\partial\phi}\right)\right] \\ \frac{1}{a^2}\left[\frac{\mathrm{U}}{\cos\phi}\left(\frac{\partial\psi'}{\partial\lambda}\frac{\partial\psi'}{\partial\phi}-\psi'\frac{\partial^2\psi'}{\partial\lambda\partial\phi}\right)+\mathrm{V}\left(\frac{\partial\psi'}{\partial\phi}\frac{\partial\psi'}{\partial\phi}-\psi'\frac{\partial^2\psi'}{\partial\phi^2}\right)\right] \end{pmatrix}$$

where $\mathrm{p} = (\mathrm{pressure}/1000\ \mathrm{hPa})$ and basic flow $|\mathbf{U}| = (\mathrm{U},\mathrm{V},0)^T$. The perturbation quasi-geostrophic streamfunction is defined as $\psi' = \Phi'/f$, where $\Phi'$ is perturbation geopotential and $f$ $(= 2\Omega\sin\phi)$ is the Coriolis parameter with the earth's rotation rate $\Omega$. The notations $a$, $\phi$, and $\lambda$ denote earth's radius, latitude, and longitude, respectively.

A significance test for the correlation coefficient is calculated based on two-sided Student's *t*-test at 95% and 99% confidence levels. The time series at each grid point must be decorrelated first to obtain the effective number of degrees of freedom, $n$. As in Livezey and Chen (1983), the autoregressive properties of both time series $A$ and $B$ are taken into account:

$$\tau = 1 + 2\sum_{i=1}^{N} C_A(i)C_B(i),$$

where $N$ and $C(i)$ denote the number of samples and the autocorrelation at lag $i$, respectively. $n$ is then estimated by:

$$n = \frac{N}{\tau}.$$

Then, the statistical significance is evaluated locally at each grid point and for each time frame. Figure 5.4 shows a distribution of $n$ from all calculations at every grid point. $n$ is distributed from 90 to 200, which corresponds to critical correlation coefficients of 0.21-0.14 and 0.28-0.19 for 95% and 99% confidence levels, respectively.

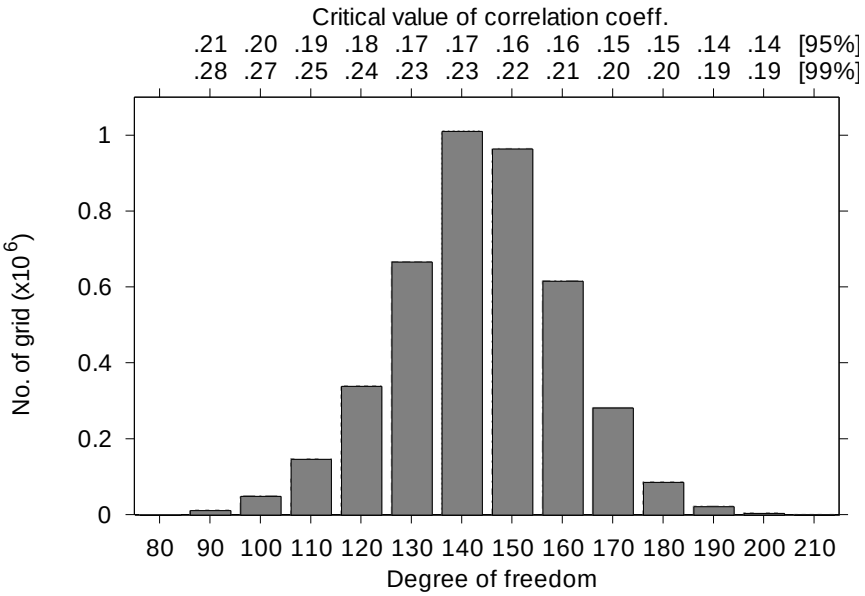


Figure 5.4 A histogram showing the number of degrees of freedom (*n*) used in the analysis. The top *x*-axis denotes the critical value of the correlation coefficient for each block of *n* at 95% and 99% confidence levels.

In Chapter 5.5, we count number of CAO events occurred throughout the study period during winter. The CAO events are collected in the same way with those shown in Chapter 4.4. The CAOs are then composited into 8 MJO phases. The significance of CAO composite is tested using Monte Carlo simulation. The test is computed as follows: 1) the CAO events that occurred when the MJO intensity ≥ 0.5 are counted; 2) all CAO events satisfying step no. 1 are distributed randomly into 8 MJO phases, resulting in a random number of CAO events for each phase; 3) step no. 2 is repeated 1000 times; 4) the probability density functions of random CAO events in all phases are averaged; 5) the highest and lowest 2.5% values are defined as the top and bottom thresholds; and 6) CAO composites above the top and below the bottom thresholds are considered significant.

## 5.3 Particular MJO phases as precursors for East Asian CAOs

### 5.3.1 Tropical evolution associated with a western CAO event

The lagged correlations/regressions with the filtered CAOIs are used to capture the atmospheric evolution associated with the intraseasonal CAO events. Figure 5.5a shows a longitude-time diagrams of the lagged correlation between tropical OLR (15°S-15°N) anomalies and the W-CAOI from day -21 to day +21. In general, day 0 corresponds to occasions when the filtered W-CAOI is a maximum. The significant negative correlation leading day 0 suggests a potential precursor to the intraseasonal W-CAO event (Figure 5.5a). It is characterized by a peak of the negative OLR anomalies over the western Maritime Continent (105°E) approximately one week before the event. The negative correlation propagates eastward crossing the Maritime Continent near day 0 and arrives at the western Pacific afterwards. Approximately two weeks after the event, a significant positive OLR anomaly develops. This is related to the characteristics of the intraseasonal W-CAOI, which has a large periodicity (Figure 5.3c). Therefore, the positive OLR anomaly in Figure 5.5a may indicate a precursor of weak equatorward flow in the W-CAO region.

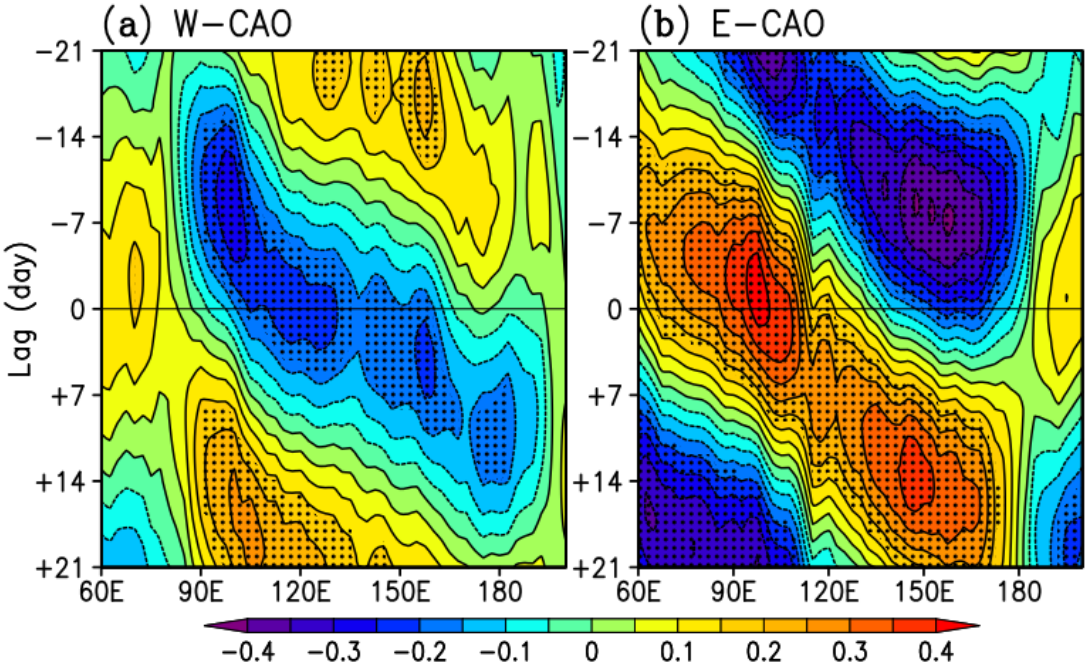


Figure 5.5 Lagged correlations between tropical OLR anomalies (averaged at 15°S-15°N) with (a) W-CAOI and (b) E-CAOI shown in longitude-time diagrams (0.05 contour interval). Horizontal lines denote day 0. Stippled areas are significant at the 95% confidence level.

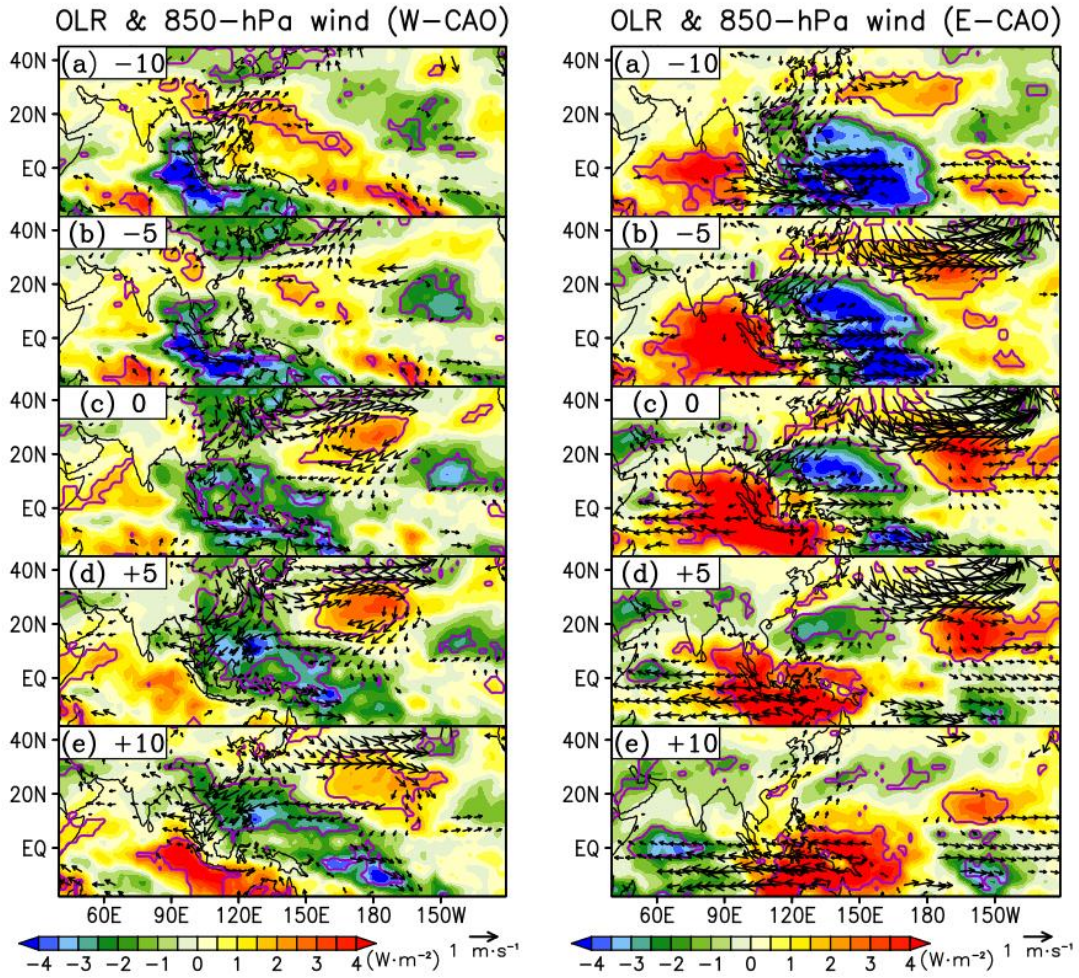


Figure 5.6 Day-lagged regressions of 30-80 day BPF tropical convection and low-level circulation onto (a) W-CAO index and (b) E-CAO index. Shading denotes OLR anomalies (contour interval 0.5 W $m^{-2}$) and vector denotes 850-hPa wind. Top panels to bottom panels show evolution from day -6 to day +6 relative to the day of CAO event (day 0).

Figure 5.6(left) presents the temporal evolution of the spatial feature of OLR and 850-hPa wind field anomalies associated with a W-CAO event. We focus on the evolution of the W-CAOI maximum during the timeline (approximately day -10 to day +10). The field anomalies shown here are constructed from a lagged regression and indicate the values according to one standard deviation of the W-CAOI. In general, the W-CAO event is accompanied by a large-scale feature of the organized tropical convections. It is characterized by a wide area of negative OLR anomalies over the Maritime Continent whose signals are more apparent before the event at day -10 and day -5 (Figure 5.6a,b(left)). At day 0, a strong equatorward outflow from mid-latitude East Asia is observed (Figure 5.6c(left)), indicating the peak of the W-CAO event. Following the W-CAO event at days +5 and +10, the large-scale negative OLR anomaly persists and propagates eastward and the low-level northerly wind dominates over the subtropical and

tropical regions (Figure 5.6d,e(left)). All these patterns are similar with Figure 5.1a, except that the MJO-like signals appear more robust than those in Figure 5.1a.

### 5.3.2 Tropical evolution associated with an eastern CAO event

The signature of tropical OLR anomalies correlated with the intraseasonal E-CAOI is shown in Figure 5.5b. Before day 0, the OLR anomaly resembles a clear dipole pattern with the negative anomaly over the western Pacific and the positive anomaly over the Indian Ocean. The OLR anomalies propagate eastward similar to the characteristics observed during the intraseasonal W-CAO event. The OLR correlations in the E-CAOI are more significant than those in the W-CAOI. The spatial variation of OLR and 850-hPa wind anomalies is shown in Figure 5.6(right). An E-CAO event is clearly led by the large-scale dipole pattern over the western Pacific and Indian Oceans (Figure 5.6a,b(right)). This dipole pattern resembles an MJO wet phase over the western Pacific, and it could be a precondition for an E-CAO event. At day 0, the CAO occurs over the northwestern Pacific Ocean (Figure 5.6c(right)). Following the event, the negative OLR anomaly weakens over the equatorial Pacific (Figure 5.6d,e(right)), while the positive OLR anomaly dominates from the Indian Ocean to the Maritime Continent. In contrast to those in a W-CAO pattern, the post-event feature of an E-CAO does not exhibit a penetration of low-level northerly flow anomaly to the tropical regions. The large portion of the extratropical mass flux from the E-CAO region is stirred eastward because of domination of stationary Aleutian low (Shoji et al. 2014; Chapter 4).

### 5.3.3 Evidence revealed in the MJO life cycle

The previous figures indicate possible influences of the MJO on the East Asian CAOs. Further analysis from a viewpoint of MJO events is needed to investigate the interactions in detail because such a way emphasizes the MJO roles. Previous studies often used simultaneous composites of several MJO phases to study the impact of the MJO (e.g.,Vecchi and Bond 2004; Jeong 2005). However, considering the forcing from the tropics takes time to affect the mid-latitude weather, it may be difficult to see the evolution and direct impact of the MJO by using the simultaneous composite.

In this study, we perform an analysis based on a combination of lagged regressions/correlations with two MJO indices. First, the MJO indices are created from the two leading EOF modes of the filtered OLR anomaly in the tropics (20°S-20°N, 30°E-120°W). OLR EOF1 shows a clear dipole pattern of tropical convection over the western Pacific and Indian Oceans, whereas OLR EOF2 shows a broad area of convection anomaly centered over the Maritime Continent accompanied by a reversed anomaly center over the central Pacific (Figure 5.7a,b). Their variance contributions are quite balanced, 14.52% for EOF1 and 13.54% for

EOF2. These OLR EOFs simply represent two orthogonal phases of the eastward propagating MJO. The autocorrelation of PC1 index and lagged correlation between PC1 and PC2 indices yield a sequence of –EOF2, +EOF1, +EOF2, and –EOF1 that appear to be separated by approximately 12 days (Figure 5.7c). We infer that a complete MJO life cycle has a nominal length of 48 days, which is identical to previous studies (e.g., Matthews et al. 2004). Progression through the MJO cycle is determined in terms of a phase angle varied from 0° ($t$ = 0 days) to 360° ($t$ = 48 days). The 0° phase corresponds to occasions when PC2 is a maximum, and simultaneous regression maps for this phase are calculated using PC2 as the dependent variable. The 180° phase, when PC2 is a minimum, corresponds to $t$ = 24 days; therefore, –PC2 is used to calculate the simultaneous regression. The 90° ($t$ = 12 days) and 270° ($t$ = 36 days) phases are denoted by simultaneous regressions using –PC1 and +PC1, respectively. Because of the periodicity in the analysis technique, $t$ = 48 days is equivalent to $t$ = 0. Regression maps at intermediate phases are constructed by linear combinations of lagged regression maps based on PC1 and PC2. For example, to determine regression maps at $t$ = 1 to 11 days, lagged regressions maps of PC2 at lag +1 to +11 day are combined with the maps of -PC1 at lag -11 to -1 day, respectively, with certain weights. The weights are linearly distributed from 11/12 to 1/12 for PC2 and 1/12 to 11/12 for -PC1. Therefore, the regression maps at $t$ = 6 days (45° phase) are obtained by combining lagged regression maps of PC2 at lag +6 day and –PC1 at lag -6 day with equal weights of 6/12. This also applies for lagged correlations. To calculate the statistical significance level, the numbers of degrees of freedom are combined using the same method. This approach enables us to depict a day-to-day evolution of the MJO life cycle.

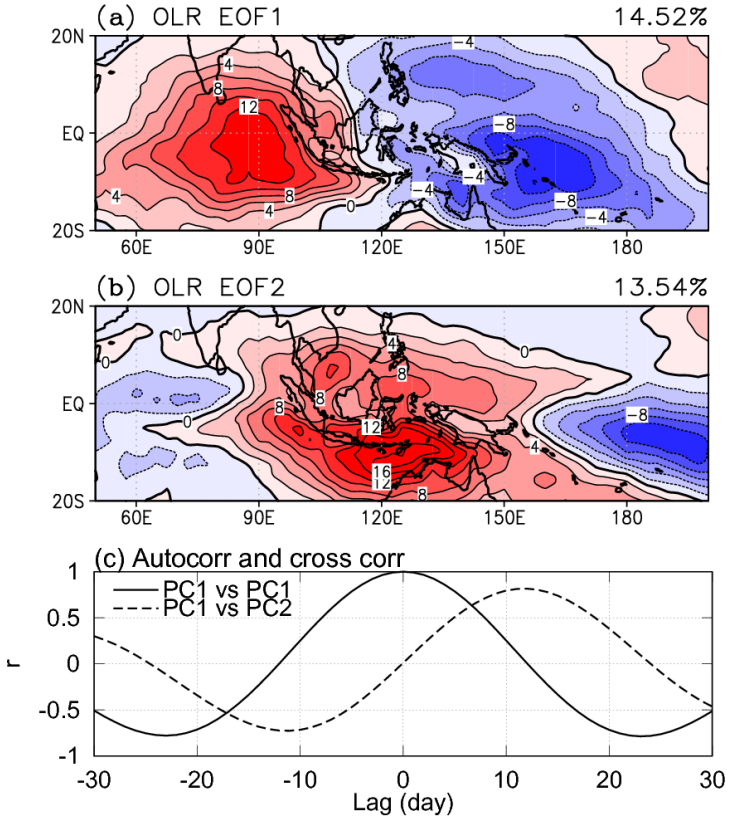


Figure 5.7 Two leading EOF modes extracted from tropical OLR anomaly fields (20°S-20°N; 50°E-160°W). OLR EOF1 and OLR EOF2 patterns are shown in (a) and (b), respectively. Contours denote the OLR anomalies obtained from simultaneous regressions with the corresponding PC indices (2 W $m^{-2}$ contour interval). (c) The solid line shows the autocorrelation of the PC1 index, and the dashed line shows the lagged correlation between the PC2 index and the PC1 index

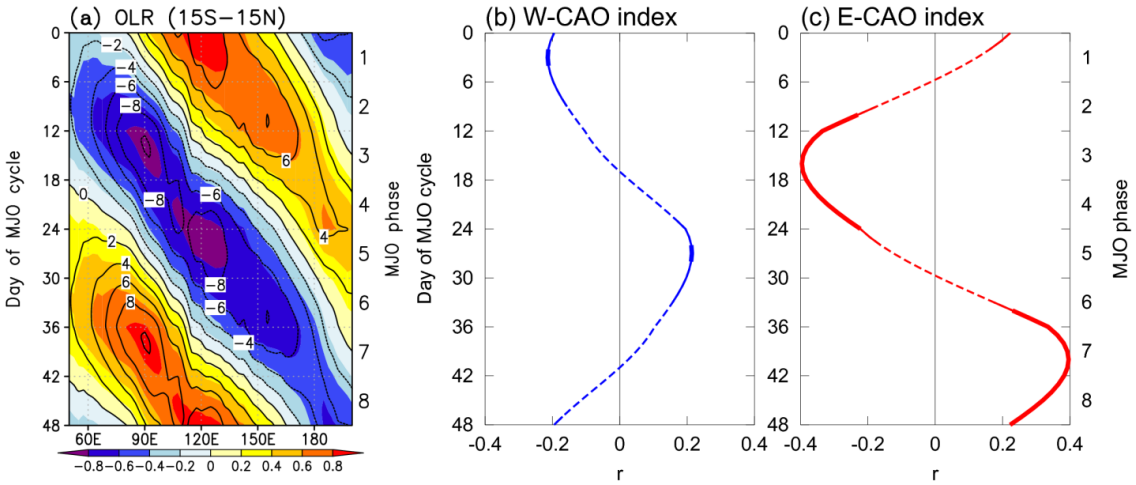


Figure 5.8 Temporal evolution of an MJO cycle calculated from the combined lagged analysis and OLR PC indices. Left and right axes denote the day of the MJO cycle or the corresponding 8-phases of the MJO. (a) The regressions (contour lines; 2 W $m^{-2}$ contour interval) and correlation coefficients (color shaded; 0.2) of OLR. (b) and (c) The variation of correlation coefficients of W-CAOI and E-CAOI, respectively. Thin and thick solid lines are significant at 95% and 99% confidence levels, respectively.

Figure 5.8a shows tropical OLR evolution of an MJO cycle in a longitude-time diagram. The negative OLR anomalies clearly propagate from the central Indian Ocean at $t$ = 0 days to the central Pacific at $t$ = 48 days, while the positive OLR anomalies appear over the central Indian Ocean at $t$ = 24 days. Figure 5.8b,c show evolution of intrasesaonal CAO indices. The maximum of the W-CAOI is approximately at $t$ = 27 days, corresponding to the MJO phase 5 or the late phase of Maritime Continent's MJO. Additionally, the maximum of the E-CAOI is seen at $t$ = 39 days, corresponding to the MJO phase 7 after the MJO crossing over the western Pacific. Because of the periodicity of the MJO, the minima of the W-CAOI and E-CAOI are observed at $t$ = 3 days and $t$ = 15 days, respectively. The minima of CAOIs differ by 24 days with their maxima. This time scale is nearly consistent with the time scale of the autocorrelations of CAO indices (Figure 5.3c).

The remote impacts of the MJO on the extratropics were often explained by poleward Rossby wave trains, which are induced by the upper-level divergence/convergence of tropical convective anomalies (Matthews et al. 2004; Lin et al. 2010; Seo and Son 2012). Here, we explore the possibility of Rossby waves influencing the East Asian CAOs. Figure 5.9 shows atmospheric circulation anomalies at $t$ = 21, 24, and 27 days represented by a 250-hPa geopotential height and its wave activity flux (Takaya and Nakamura 2001), 500-hPa geopotential height, and the PCAM amount and its flux below 280 K, as well as 850-hPa wind and temperature fields. The convection over the Maritime Continent induces an upper-level anomalous anticyclone over South Asia (Figure 5.9), which subsequently develops upper-level anomalous cyclonic circulation over mid-latitude East Asian coast. The extratropical response is quite barotropic. The development of a 500-hPa East Asian trough is clear and reaches its peak at $t$ = 27 day (Figure 5.9b). The trough triggers more equatorward cold air flow in the west of the cyclone, which is the location of W-CAO (Figure 5.9c). The evolution of low-level monsoon circulation is also observed (Figure 5.9d). The anomalous 850-hPa northerly and cold temperature extend from mid-latitude East Asia to the tropical region. On the other hand, Figure 5.10 exhibits atmospheric anomalies at $t$ = 33, 36, and 39 days. The Rossby wave trains, which are induced by the convective anomalies over the western Pacific and Indian Oceans, are also evident (Figure 5.10a) and even stronger than those in Figure 5.9a. This stronger wave train induces stronger negative pressure anomalies and yields greater response of equatorward PCAM flow in E-CAO compared with those in W-CAO case.

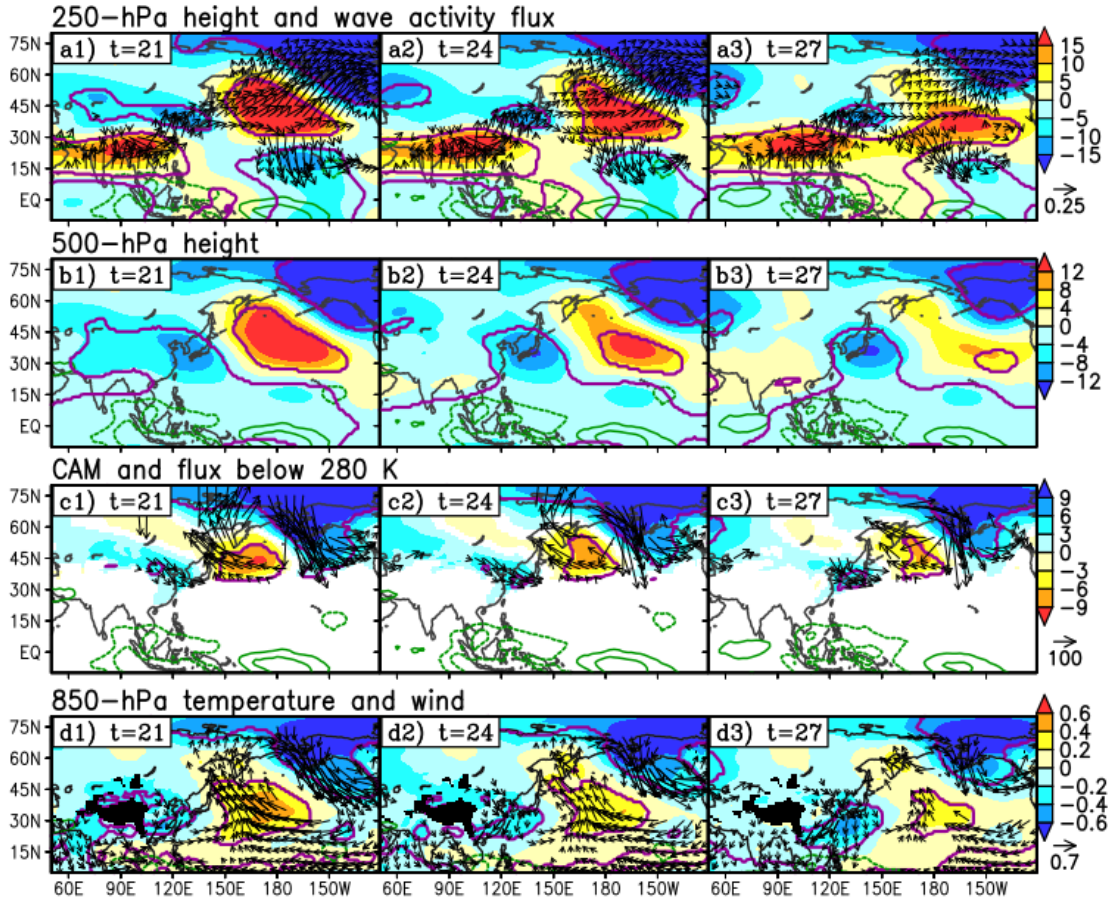


Figure 5.9 Atmospheric anomalies at $t$ = 21 (left), $t$ = 24 (middle), and $t$ = 27 day (right) of MJO cycle. From top to bottom: (a1-a3) 250-hPa height (shaded; 5 gpm contour interval) and wave activity flux ≥ 0.05 $m^2$ $s^{-2}$ (vector), (b1-b3) 500-hPa height (shaded; 4 gpm contour interval), (c1-c3) CAM amount (shaded; 3 hPa contour interval) and its flux (vector; unit in hPa m $s^{-1}$) below 280 K, and (d1-d3) 850-hPa temperature (shaded; 0.2 K contour interval) and wind (vector; unit in m $s^{-1}$). Purple contours and vectors in c) and d) denote significant correlations at the 95% confidence level. Green contours indicate OLR anomalies with a 4 W $m^{-2}$ contour interval (zero values omitted).

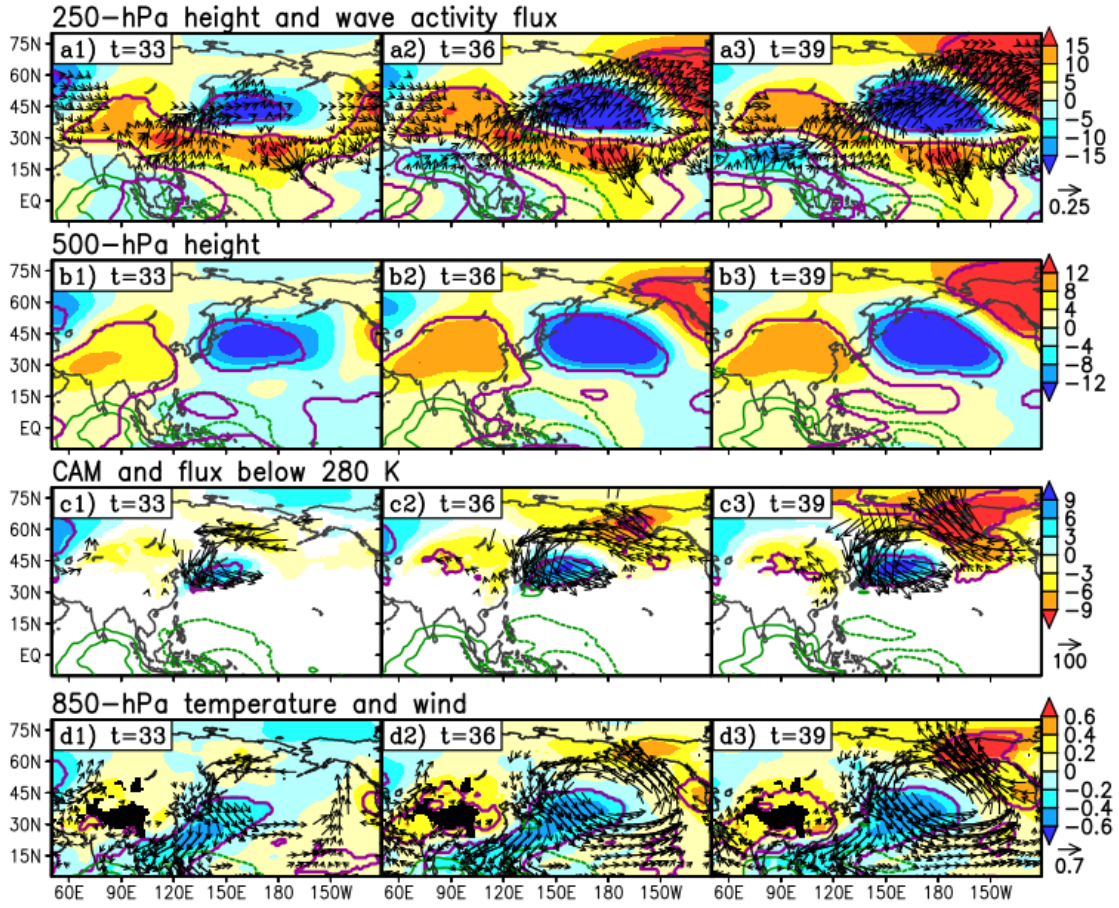


Figure 5.10 As in Fig. 5.9, but for $t$ = 33 (left), $t$ = 36 (middle), and $t$ = 39 day (right).

Figure 5.11 shows the temporal evolution of the East Asian meridional PCAM fluxes and 500-hPa geopotential height anomalies in an MJO cycle. This figure clearly shows that the variation of East Asian CAOs is strongly guided by the center of mid-latitude trough and ridge. The equatorward flow becomes stronger when the trough is apparent, but becomes weaker when the ridge prevails. The equatorward flow anomaly starts to develop at approximately $t$ = 15 days (phase 3) over the westernmost part. It then propagates eastward following the center of the trough developed by the MJO. The response over the E-CAO region is more robust than it is over the W-CAO region because the anomaly height is larger over the eastern part than it is over the western part.

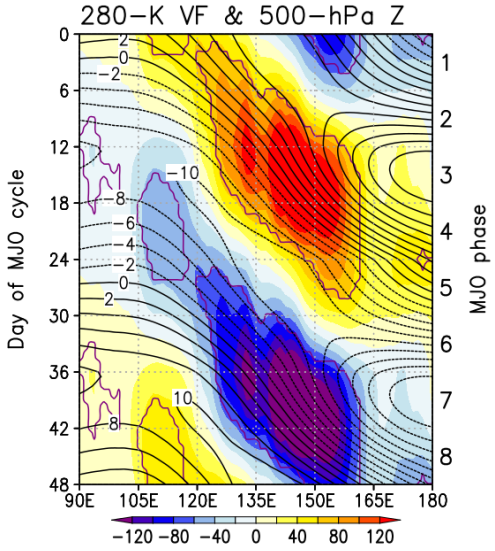


Figure 5.11 Longitude-time diagram of anomalous meridional component of a 280-K CAM flux at 45°N (color shaded; 20 hPa m $s^{-1}$ contour interval) and a 500-hPa geopotential height averaged over 30°-40°N (black contour; 2 gpm contour interval). Purple lines enclose the significant meridional CAM flux at the 95% confidence level.

## 5.4 **Numerical simulations with more realistic tropical heating**

To demonstrate the impact of the MJO, we perform numerical experiments using a linear baroclinic model (LBM; Watanabe and Kimoto 2000) using prescribed MJO-like thermal forcing. Model configurations are generally similar with those in Chapter 4, except the horizontal pattern of heating is approximated from MJO-like convection anomalies rather than idealized Gaussian patterns. Table 5.1 shows a list of experiments. The experiments can be divided into two groups: MJO-A and MJO-B experiments. Thermal forcing in MJO-A is estimated from tropical OLR anomalies (20°S-20°N, 40°E-120°W) when the MJO crosses over the Maritime Continent (–EOF2 pattern), whereas MJO-B mimics the heating pattern when the MJO crosses over the western Pacific (+EOF1 pattern). OLR anomalies <2 W $m^{-2}$ and >-2 W $m^{-2}$, as well as minor convective centers, are excluded from the model input. The minimum or maximum thermal forcing is set to be approximately 4 or -4 K $dy^{-1}$. Furthermore, we perform sensitivity experiments to reveal the relative importance of different heating centers. The results are expected to provide answers for why the wave train and extratropical response in the E-CAO are stronger than those in the W-CAO. MJO-A_MC and MJO-A_CP experiments simulate atmospheric responses based on the Maritime Continent heating and the central Pacific cooling, while MJO-B_WP and MJO-B_IO experiments simulate the responses based on the western Pacific heating and the Indian Ocean cooling, respectively.

Table 5.1 Name and description of experiments carried out in the linear model simulations

| Experiment | Description of heating source |
|---|---|
| MJO-A | Approximated from simultaneous regressions between -PC2 index and tropical OLR |
| MJO-A_MC | As in MJO-A exp., but only heating over the Maritime Continent |
| MJO-A_CP | As in MJO-A exp., but only cooling over the central Pacific |
| MJO-B | Approximated from simultaneous regressions between +PC1 index and tropical OLR |
| MJO-B_WP | As in MJO-B exp., but only heating over the western Pacific |
| MJO-B_IO | As in MJO-B exp., but only cooling over the Indian Ocean |

Figure 5.12a shows the linear response of atmospheric circulation in the MJO_A experiments two weeks after the integration. The wave trains are evident over East Asia (Figure 5.12a(left)) that deepen the East Asian trough, induce equatorward flow over the W-CAO region and bring more cold air mass to East Asia (Figure 5.12a(right)). The sensitivity experiments of MJO-A_MC and MJO-A_CP suggest that the East Asian responses are strongly controlled by the Maritime Continent heating (Figure 5.12b,c). The response due to the central Pacific cooling is significantly weaker that the response due to Maritime Continent heating, and even indicates an anticyclone over the North Pacific that inhibits equatorward flow. In fact, the lagged regression of OLR anomalies onto the W-CAOI shows only a weak signal over the central Pacific (Figure 5.6(left)). The importance of Maritime Continent heating for W-CAO was also mentioned in Chapter 4.

Figure 5.13a shows the atmospheric responses in the MJO-B experiment. The resulting Rossby wave trains appear from South Asia to North America, develop a cyclonic anomaly over the North Pacific, and trigger an equatorward cold air flow over the E-CAO region. The Rossby waves are substantially stronger than those in the MJO-A experiment, which is consistent with the observations. Unlike MJO-A cases, the sensitivity experiments of MJO-B_WP and MJO-B_IO show the important roles of both western Pacific heating and Indian Ocean cooling on the development of E-CAO (Figure 5.13b,c). The response in E-CAO is greater than that in W-CAO because of the collaborative effects of in-phase Rossby waves induced by western Pacific heating and Indian Ocean cooling.

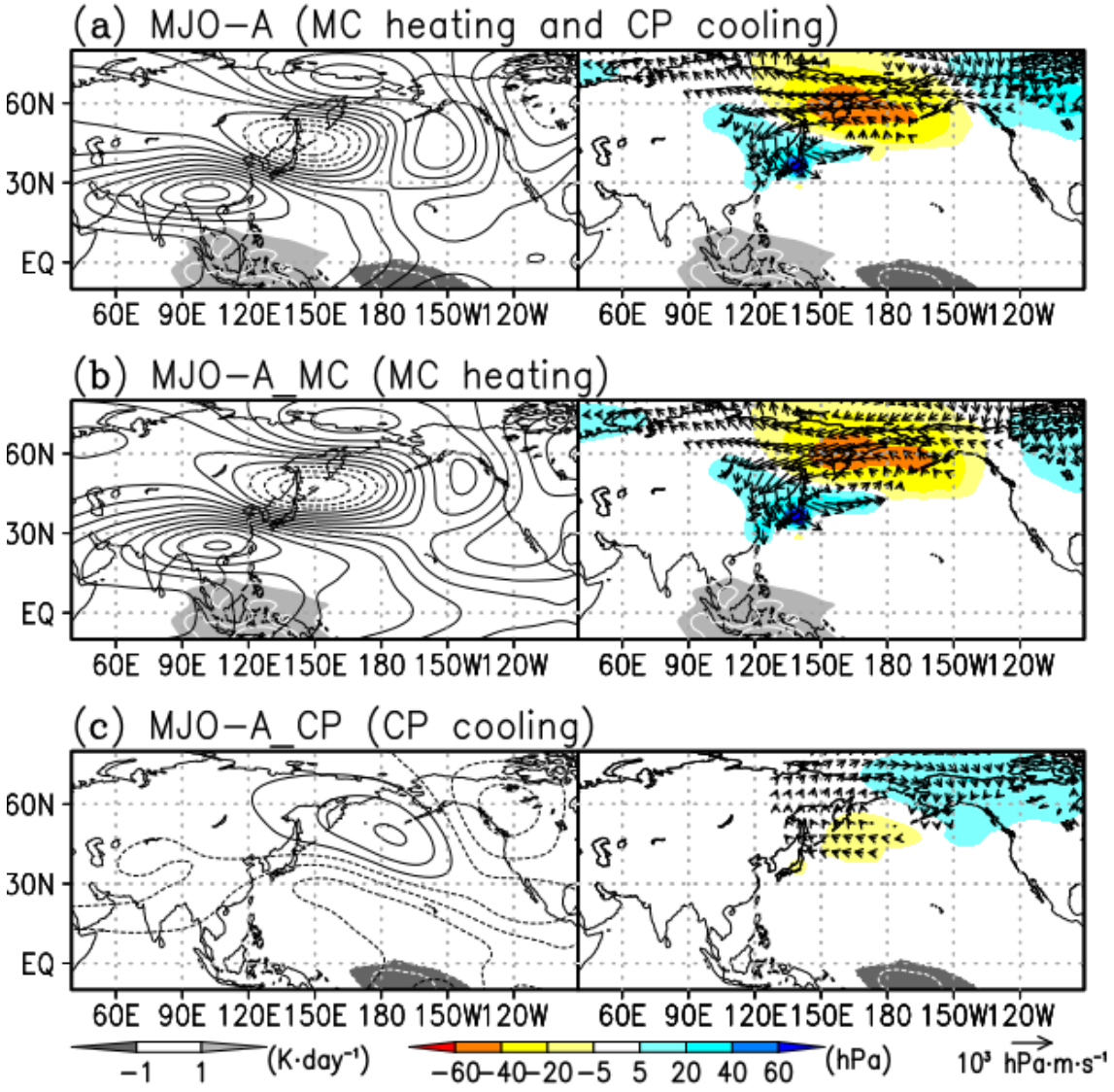


Figure 5.12 Northern hemisphere atmospheric responses two weeks after the integration in (a) MJO-A, (b) MJO-A_MC, and (c) MJO-A_CP experiments denoted by anomalies of (left) a 250-hPa geopotential height (black contour with 10 gpm contour interval) and (right) a CAM (blue-red color shadings) overlapped with its flux (vector). Light and dark gray shadings in the tropics denote the prescribed positive and negative heating anomalies greater than ±1 K $dy^{-1}$.

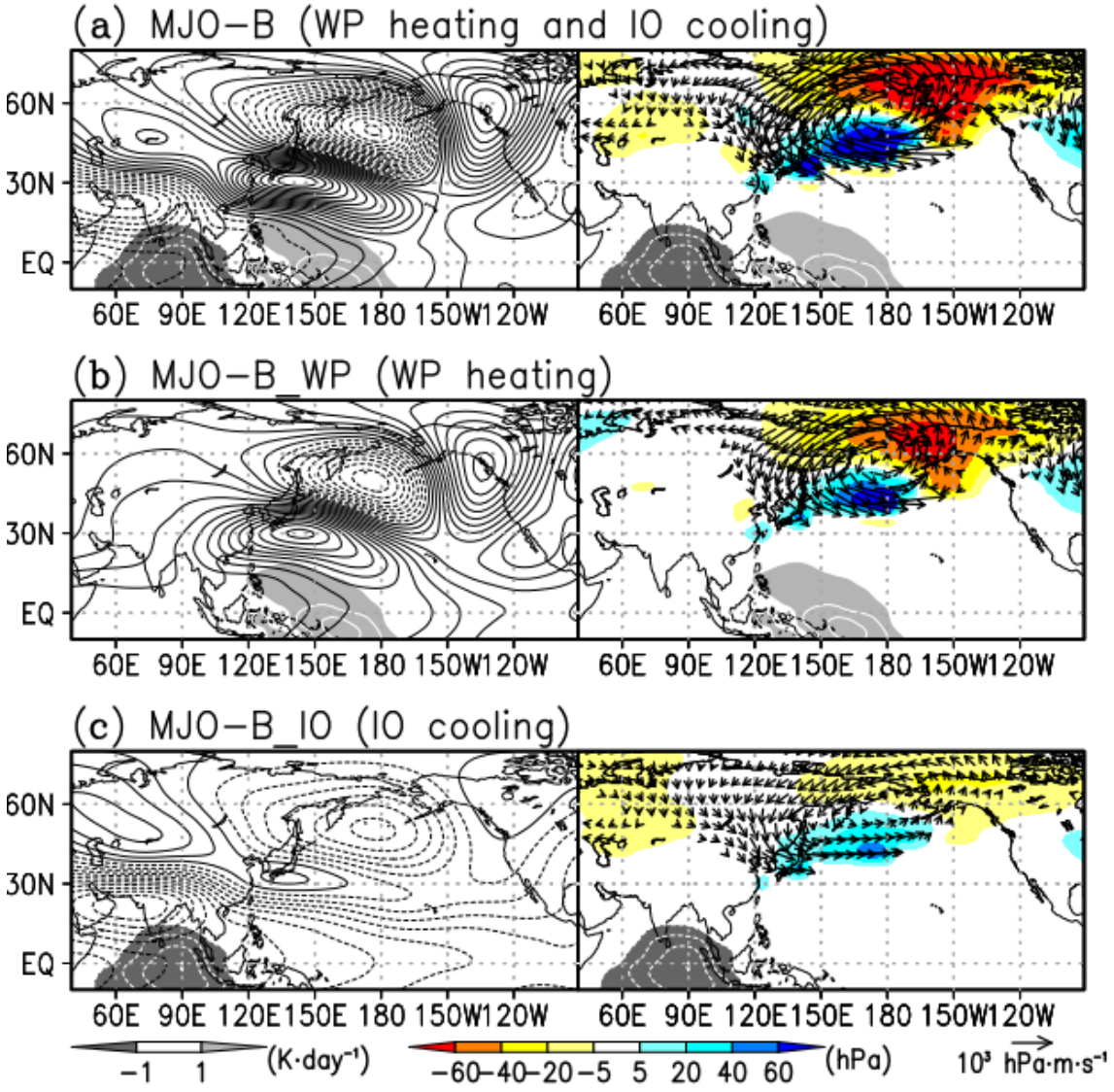


Figure 5.13 As in Fig. 5.12, but for MJO-B, MJO-B_WP, and MJO-B_IO experiments.

## 5.5 **Influence of MJO on short-term CAO events**

Despite the inability of the MJO to predict the timing of short-term/synoptic scale CAO events, the MJO may play a significant role on the probability of its occurrence. Here, we create a composite analysis of the short-term CAO events in eight MJO phases. The CAO events are identified based on local maxima of unfiltered CAO indices; the maxima must be greater than or equal to 1.5 standard deviation. There is a total of 151 W-CAO events and 130 E-CAO events captured during the analysis period. We count the number of CAO events that occurred in specific MJO phases, and perform a significance test using the Monte Carlo bootstrap method (Efron and Tibshirani 1993; Li et al. 2016) (see Chapter 5.2).

Figure 5.14 exhibits distributions of short-term W-CAO events and E-CAO events over MJO phase-space diagram of Wheeler and Hendon (2004). The diagram is built from RMM indices that are obtained from Australian Bureau of Meteorology website. The figure shows that W-CAO events tend to occur after the MJO crossing over the Maritime Continent (Figure 5.14a). For a comparison among the MJO phases, the maximum number of W-CAO events is detected in phase 5 (20.1%) followed by phase 6 (18.0%), whereas the lowest frequency is observed in phases 8 (6.5%) and 1 (7.2%). They are statistically significant at 95% (Figure 5.14c). Meanwhile, the E-CAO events tend to occur after the MJO crossing over the western Pacific, where several extreme events are observed (phases 7 and 8) (Figure 5.14b). The significant maximum occurrence is observed in phase 7 with 19% of the total frequency (Figure 5.14d), while there is no clear minimum peak. Figure 5.14e,f show the frequency distributions of CAO events analyzed using the OLR EOF indices. The result is somewhat consistent with the CAO distribution in the RMM indices. The peak of W-CAO occurrence appears in phase 5 (Figure 5.14e) and emphasizes the CAO occurrence during the post-stage of the Maritime Continent's MJO. Additionally, the peaks of E-CAO occurrence are observed in phase 8 and 6 (Figure 5.14f), rather different with those obtained from RMM indices. The occurrence probability of E-CAO events seems sensitive to the definition of MJO indices. In OLR EOF indices, the E-CAO occurrences are distributed widely during MJO phases over the western to central Pacific.

This finding suggests impacts of the MJO on the probability of short-term/synoptic scale CAO occurrence. The intrasesonal response to MJO seems to provide favorable background conditions, such as negative geopotential height anomalies which may cause CAO to occur more often.

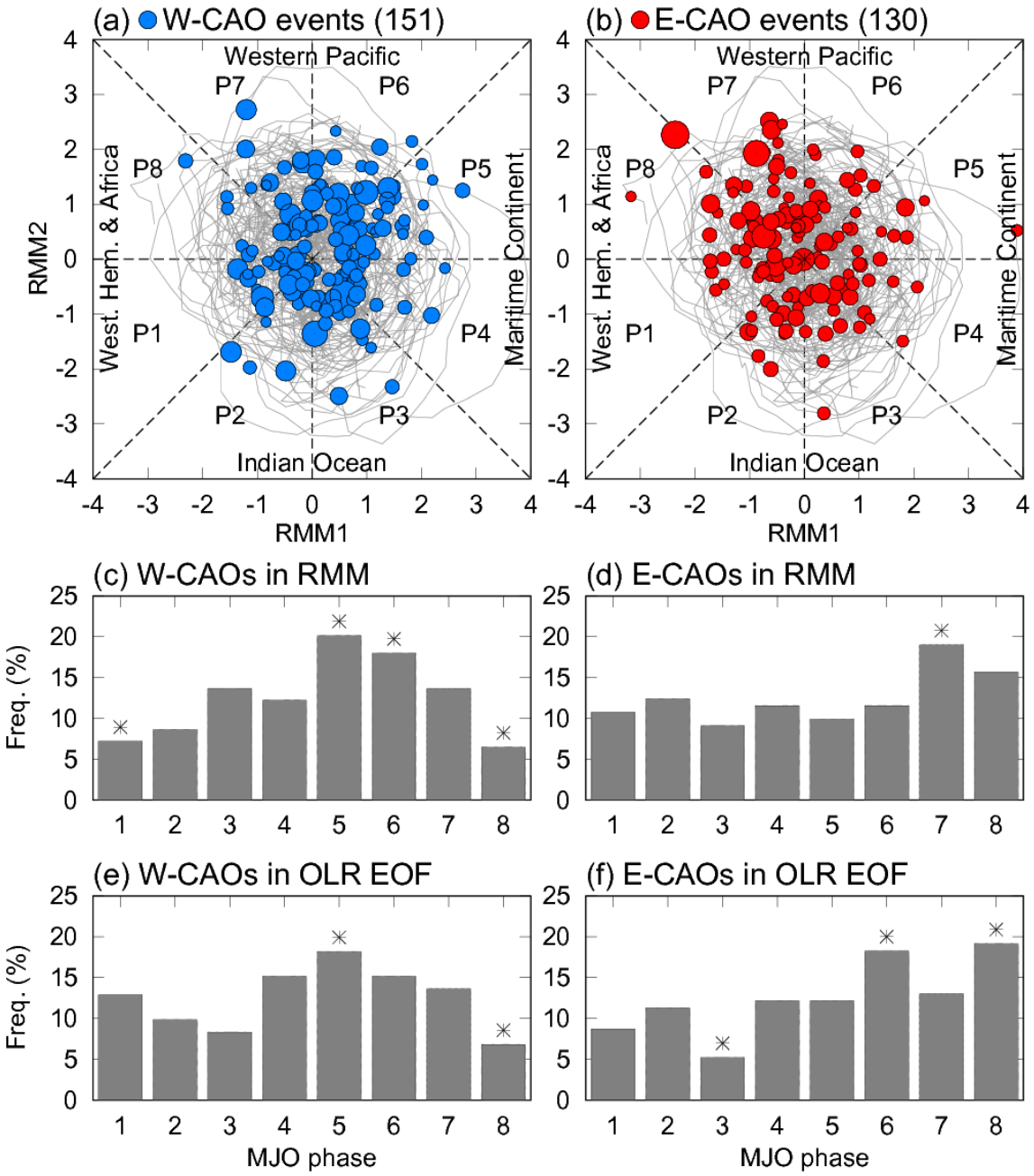


Figure 5.14 (a,b) Scatterplot distribution of short-term (a) W-CAO events (blue circles) and (b) E-CAO events (red circles) over the MJO phase-space diagram using RMM indices (Wheeler and Hendon 2004). The size of the circles is proportional to the intensity of the CAO event. Historical MJO tracks are drawn as gray lines. (c-f) The percentage of CAO events are calculated for each MJO phase (MJO intensity ≥ 0.5) in (c,d) RMM indices and (e,f) OLR EOF indices. The asterisks indicate statistical significance at the 95% confidence level using Monte Carlo simulation.

## 5.6 **Circulation anomalies in eight MJO phases**

Several studies have investigated the influences of the MJO on East Asia. Using a simultaneous composite analysis in eight MJO phases, Jeong et al. (2005) concluded that the MJO over the Indian Ocean (phases 2 and 3) tends to cause cold events and cold surges with more dominant influence at phase 3. It seems at first to be inconsistent with our finding related to the W-CAO development that appears at phase 5. To validate the consistency, we show the evolution of low-level temperature anomalies for the eight MJO phases (Figure 5.15). This figure is comparable with Fig. 1 in Jeong et al. (2005). The temperature anomalies associated with the MJO phases shown in their result are similar to our result to a broad extent. Here, the broadest significant cooling over continental East Asia is observed at phase 3 (Figure 5.15c), which does not contradict with their finding. To get a better view, 850-hPa wind anomalies are shown in Figure 5.15, and a 280-K anomalous PCAM flux is shown in Figure 5.16. At phase 3, significant northerly winds are mainly located over inland China (Figure 5.15c). The northerly PCAM flux toward inland China is observed at phase 3, but its amplitude and its region are rather limited (Figure 5.16c). However, phase 5 exhibits strong northerly anomalies emanating from 45°N latitude (Figure 5.15e and Figure 5.16e). Significant low-level temperature drops are largely observed near the southern Korean Peninsula, Japan, and Southern China (Figure 5.15e). Another important signature at phase 5 is that the northerly and cold anomaly extends to the East China Sea and propagates to the South China Sea and Southeast Asian countries (Figure 5.15e,f).

The difference in conclusions from those of Jeong et al. (2005) is related to the difference in CAO definition. One of cold surge criteria in their study was based on temperature drops over the Middle or South of China. Using this definition, most of the cold events are captured at phase 3 (Figure 5.15c and Figure 5.16c). In this study, we define W-CAOI as an equatorward cold air mass flux at 45°N, 90°-135°E, whose magnitude reaches a maximum at phase 5. Nevertheless, our temperature anomaly maps are quite consistent, although some minor differences may exist due to the difference in analysis techniques and the utilization of a time filter. It is very clear that the pathway of anomalous northerlies shifts eastward following the MJO propagation. The enhanced equatorward flux that appears at phase 3 extends and propagates eastward at phases 4 and 5. It then gradually evolves into an E-CAO-type flux at phases 6 to 8. Our result demonstrates that the location of anomalous northerly flow in East Asia is sensitive to the MJO propagation. This northerly cold flux is controlled by the propagation of the East Asian trough, as shown in Figure 5.11.

Our result is also consistent with a study by He et al. (2011). They investigated the pentad-scale evolution of East Asian weather using regression analysis with the two leading MJO modes. They showed that the MJO over the Maritime Continent enhances East Asian winter monsoon circulation and brings cold and dry weather over East Asia, while the Indian Ocean MJO and western Pacific MJO lead to the occurrence of cold weather over the western (continental) and eastern (oceanic) East Asia, respectively (He et al. 2011). In our study, phase 5 in Figure 5.15e (3 days after the peak of the Maritime Continent MJO) exhibits strong northerly and cold anomalies in East Asia indicating the enhanced winter monsoon circulation documented in He et al. (2011). While the dipole patterns between the western and eastern parts appear at phases 3 and 7 (Figure 5.15c, g), which are also consistent with their result. He et al. (2011) suggested that, to some extent, the enhanced local Hadley circulation associated with the Maritime Continent MJO strengthens the East Asian winter monsoon. This could explain why the northerlies at phase 5 are quite strong near subtropical coastal China and the East China Sea (Figure 5.15e) despite the cold air outbreak from mid-latitude being not so strong (Figure 5.15e andFigure 5.16e).

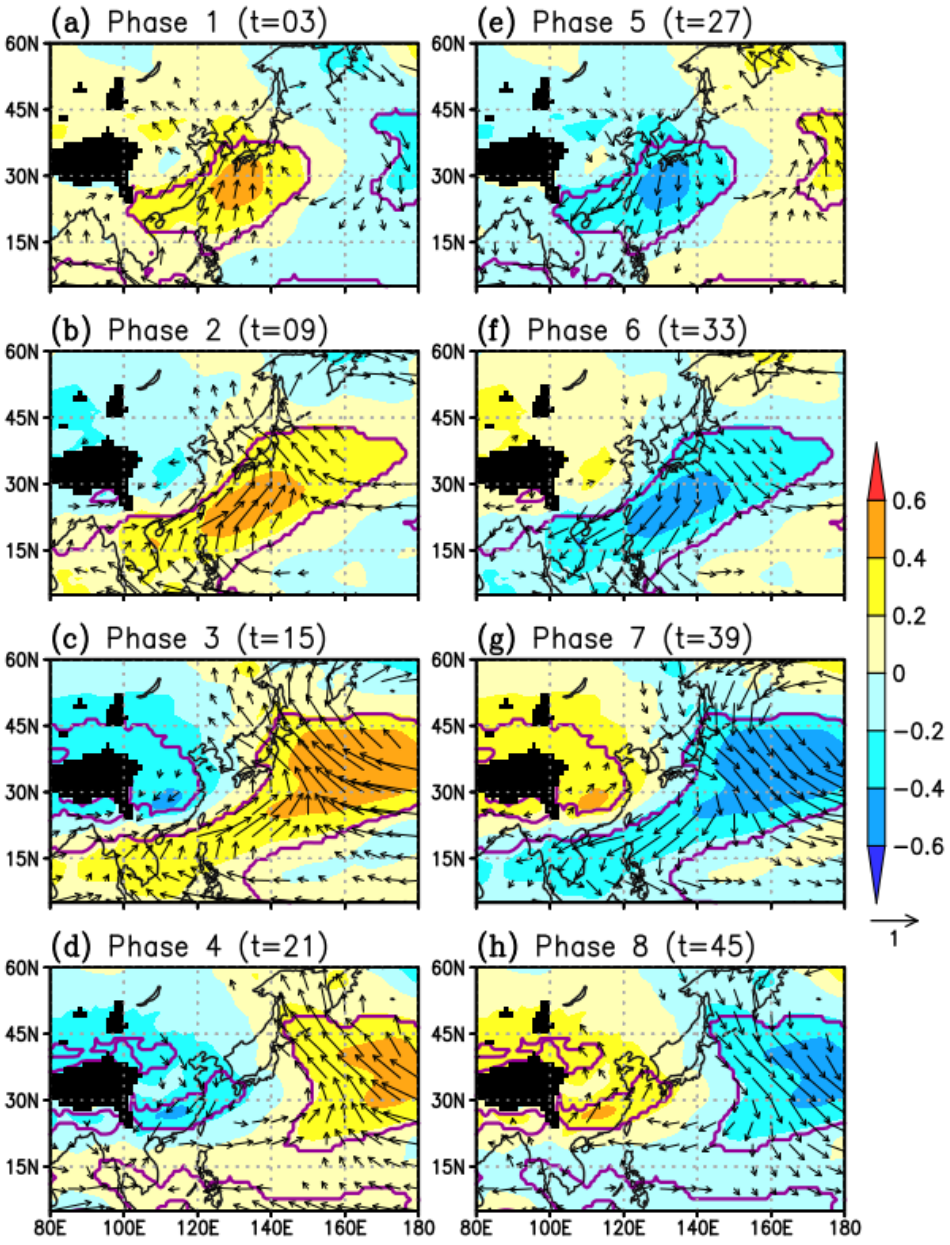


Figure 5.15 (a-h) 850-hPa wind (vector; unit in m $s^{-1}$) and temperature (shading; unit in K) anomalies at eight MJO phases selected from the 48 days MJO cycle. Only wind vectors exceeding 95% confidence level are shown. Purple contours serve as the boundary of temperature with 95% confidence level.

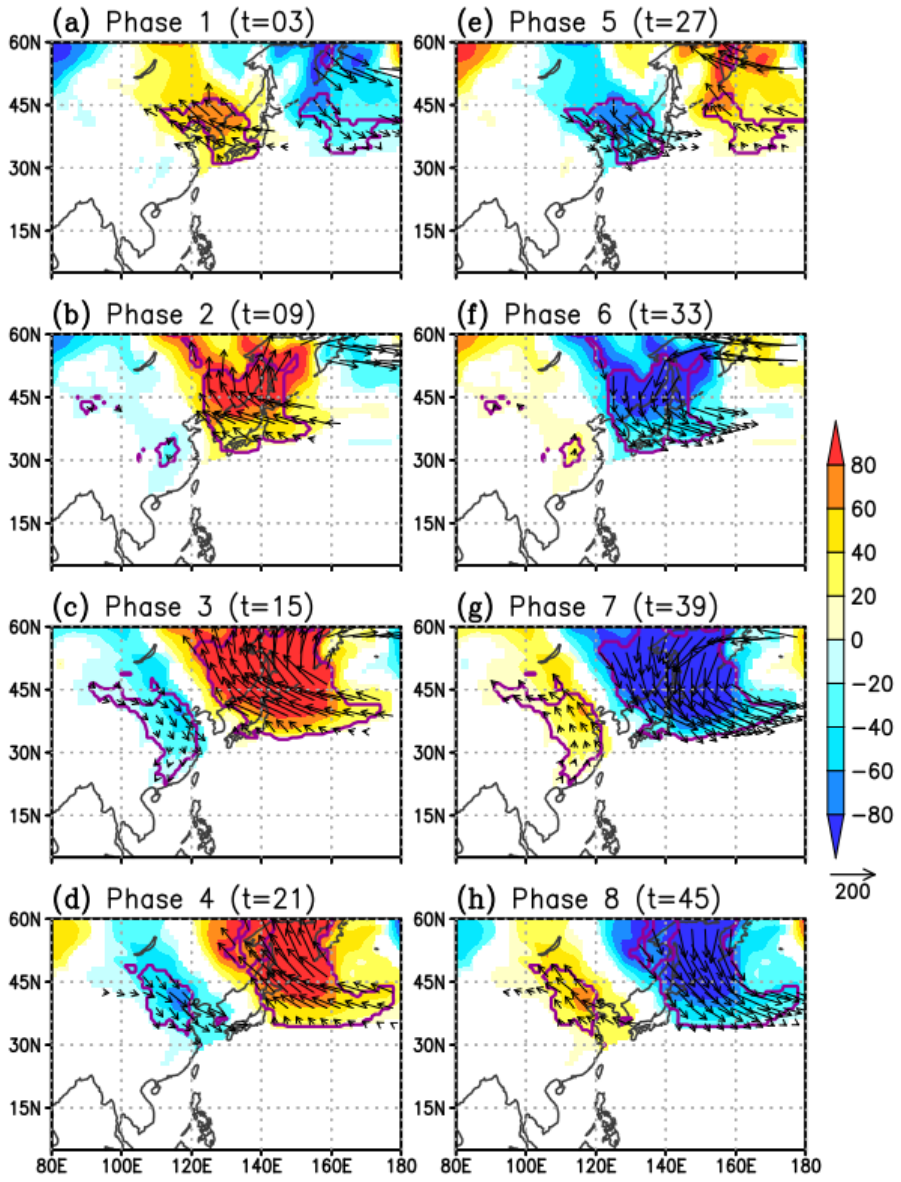


Figure 5.16 As in Fig. 5.15, except for the 280-K CAM flux (vector; unit in hPa m s-1) and the meridional component of mass flux (shading; unit in hPa m s-1).

## 5.7 **Conclusion**

We have investigated the interactions between tropical atmosphere and East Asian CAOs on an intraseasonal time scale (30-80-day period). Two quantitative East Asian CAOs are examined: W-CAO and E-CAO. Lagged regressions and correlations are used to determine the evolution of CAO events. It is found that the intraseasonal W-CAO and E-CAO events are preconditioned by MJO-related large-scale convections with the signals preceding the CAOs by approximately 1 week. The precursor for W-CAO is the MJO over the Maritime Continent, while the precursor for E-CAO is the MJO over the western Pacific. The remote impact is delivered by poleward Rossby wave trains excited by anomalous tropical convections, which in turn develop negative geopotential height anomalies in mid-latitude East Asia and affect the low-level PCAM flux. Model simulations using linearized GCM show that the response in E-CAO is stronger than it is in W-CAO because the Rossby wave trains during the western Pacific's MJO are more significant because of the in-phase relationships of circulation patterns excited by anomalous convections over the western Pacific and Indian Oceans.

Reflecting our results in Chapter 4 and this chapter, the tropics have significant effects on the East Asian CAOs in two frequency bands: interannual and intraseasonal time scales. The seasonal mean of a CAO is affected by ENSO (Chapter 4), whereas the intraseasonal CAO event is affected by the MJO in a 30-80-day band period. The sensitivity analysis shown in Figure 5.2 finds no notable interactions between the tropics and short-term CAO events in the high-frequency band (< 30 day), as indicated by the very small correlations. The tropical waves in this period (< 30 day) are not strong enough to transfer a remote impact to the extratropics. It was documented that the shorter the timescale of the anomalous tropical heating, the more equatorially trapped is the atmospheric response (Trenberth et al. 1998). Therefore, the timing of short-term/synoptic scale CAO events is largely controlled by the internal extratropical dynamics. Despite that, the MJO does influence the occurrence probability of short-term CAO events, as shown by the composite analysis. Comparing among the MJO phases, approximately 38% (34%) of short-term W-CAO (E-CAO) events occur at phases 5 and 6 (phases 7 and 8) following the MJO over the Maritime Continent (western Pacific). The MJO develops a favorable background condition in the extratropics that facilitates more frequent CAO events. A more detailed study is needed to investigate the MJO influence on the transient CAOs.

The location of intraseasonal northerly anomalies in East Asia is sensitive to the MJO propagation. The equatorward flow starts to develop at phase 3 over continental East Asia (Jeong et al. 2005), particularly, over the western part of the W-CAO region, which then extends and shifts eastward following the development of the East Asian trough at phases 4 and

5. At phase 5, the W-CAOI reaches its maximum, and the low-level winter circulation in East Asia becomes more active (He et al. 2011). The equatorward flow then gradually evolves into an E-CAO-type flux at phases 6 to 8. These results imply the complexity of the MJO's influence over East Asia because East Asia covers a vast region elongating from the subtropics to polar region and from the Tibetan plateau to the North Pacific, and they require careful interpretation depending on the region of interest.

In Chapter 4, we investigated the interannual variability of CAOs, and its relationship with tropical climate. Two leading EOF modes of East Asian equatorward flow were identified. Both are consistent with W-CAO and E-CAO. ENSO-related convection anomalies affect the intensity of seasonal-mean East Asian CAO indices. La Niña tends to induce a strong W-CAO winter, and El Niño tends to induce a strong E-CAO winter. In this chapter, the intraseasonal CAO events are affected by particular phases of the MJO. The intraseasonal W-CAO is triggered by the MJO over the Maritime Continent and is consistent with Chapter 4 according to the location of convection. While the intraseasonal E-CAO is shown to be controlled by wet MJO over the western Pacific and dry MJO over the Indian Ocean. This finding improves our understanding on the precursors of equatorward fluxes over E-CAO region. Based on the numerical experiments in this chapter and Chapter 4, the E-CAO flux can be affected by tropical heating over the western to central Pacific and cooling over the Indian Oceean. These studies emphasize the importance of tropical convections on medium- and long-range CAO forecasting. Despite the different time scales between the MJO and ENSO, the characteristics of MJO evolution and its teleconnection sometimes depend on ENSO phases (Moon et al. 2011; Feng et al. 2015). A more detailed study on the interactions between CAO-MJO-ENSO is needed to gain a better understanding on the CAO variation.

# 6. Impact of cold air outbreaks on tropical weather variability

## 6.1 **Introduction**

The previous Chapters 4 and 5 show the importance of tropical convections on the development of extratropical CAOs over East Asia. Here, we investigate the possible influence of the CAOs on tropical convections. The East Asian CAOs exhibit two distinct modes: W-CAO and E-CAO. However, this chapter specifically discusses the impacts coming from W-CAO events. E-CAO is not considered because, as shown in Chapter 5, the northerly flow associated with E-CAO does not penetrate deeply into low latitudes (Figure 5.1).

## 6.2 **Data and method**

We utilize the Japanese 55-year Reanalysis (JRA-55) (Kobayashi et al. 2015) for CAO calculations and atmospheric circulation. The JRA-55 is available from Jan 1958. Daily interpolated Outgoing Longwave Radiation (OLR) is used as a proxy of tropical convection (Liebmann and Smith 1996). OLR data is provided by NOAA/OAR/ESRL PSD and has 2.5° horizontal resolution. The OLR data is available from 1974; however the data suffers from many missing dates prior to 1979. For precipitation, we use daily Global Precipitation Climatology Project (GPCP) version 1.2 which has 1° horizontal resolution. The GPCP data is derived from multi-satellite observations and available from late 1996.

This chapter consists of lagged regression analysis and clustering analysis. The former aims to identify the *average* response of tropical precipitation following the W-CAO events. The latter aims to find *inhomogeneity* among independent precipitation responses. The clustering builds some groups of CAO events. Each group has consistent pre-defined condition(s), which are explained later in the next sub-chapters.

The dataset is temporally filtered by 6-day low-pass filter (LPF). Removing high-frequency variations helps us to focus our attention on synoptic and intraseasonal variability. The selection of 6 day limit is consistent with previous studies (e.g., Compo et al. 1999), which showed that the equatorward penetration of East Asian cold surges are robust on the period greater than 6 day. The filtering method is the Lanczos filter (Duchon 1979). The CAO events

are identified as local maxima of daily filtered W-CAO index. The basic formulation of W-CAO index is mentioned in Chapter 2.1.3.

The analysis periods are 1979/80 to 2012/13 winter for circulation and OLR-related analysis and 1997/98 to 2012/13 winter for precipitation-related analysis. This difference in the period may cause slight differences in the results due to different number of samples. To assess the consistency of the results between these two periods, we qualitatively compare OLR patterns and precipitation patterns. Over the tropical regions, the OLR and precipitation has excellent correlation (Xie and Arkin 1998). Therefore, a good consistency between these two periods would be achieved if OLR in the long period has similar pattern with precipitation in the short period. The statistical significance of regression analysis is assessed by two-sided student's *t*-test at 99% confidence level.

## 6.3 **Lagged regression: mean response of precipitation**

The basic evolution of W-CAO (hereafter CAO) event is documented in Shoji et al. (2014) and briefly shown in Figure 2.6. The CAO is preconditioned by developing Siberian High in north of Tibetan Plateau. During the peak of CAO, the strong equatorward flux brings PCAM from northern Eurasia to midlatitude East Asia. Following the CAO, the PCAM rapidly disappears over south of 45°N due to diabatic heating from warm ocean surface of Kuroshio. Although the PCAM and its flux already disappear following the peak of CAO, the low-level northerly wind anomalies still persist and even propagate to tropical regions. The strong intrusion of northerlies is maintained by southward expansion of Siberian High (Figure 6.1(top)).

The average impacts of anomalous northerlies on tropical convection and precipitation are shown in middle and bottom panels of Figure 6.1. At day +2, negative OLR anomalies develop over the subtropical ocean. These may indicate the development of shallow clouds due to low-level turbulences (Chang et al. 1979). The negative OLR anomalies expand to the tropics over Philippines and South China Sea, which develop largely at day +4. In this area, the convections are deeper (indicated by larger negative anomalies) and induced by strong northerlies that interact with complex topography over the Maritime Continent. The tropical response shown by precipitation signals is also evident. Despite the difference in study period, the precipitation pattern closely resembles OLR pattern, especially over the tropics south of 15°N where the negative OLR anomalies are large. Therefore, the results show consistency in terms of convective activities and study period. The regression analysis clarifies the remote impact of East Asian CAO event over the tropical regions.

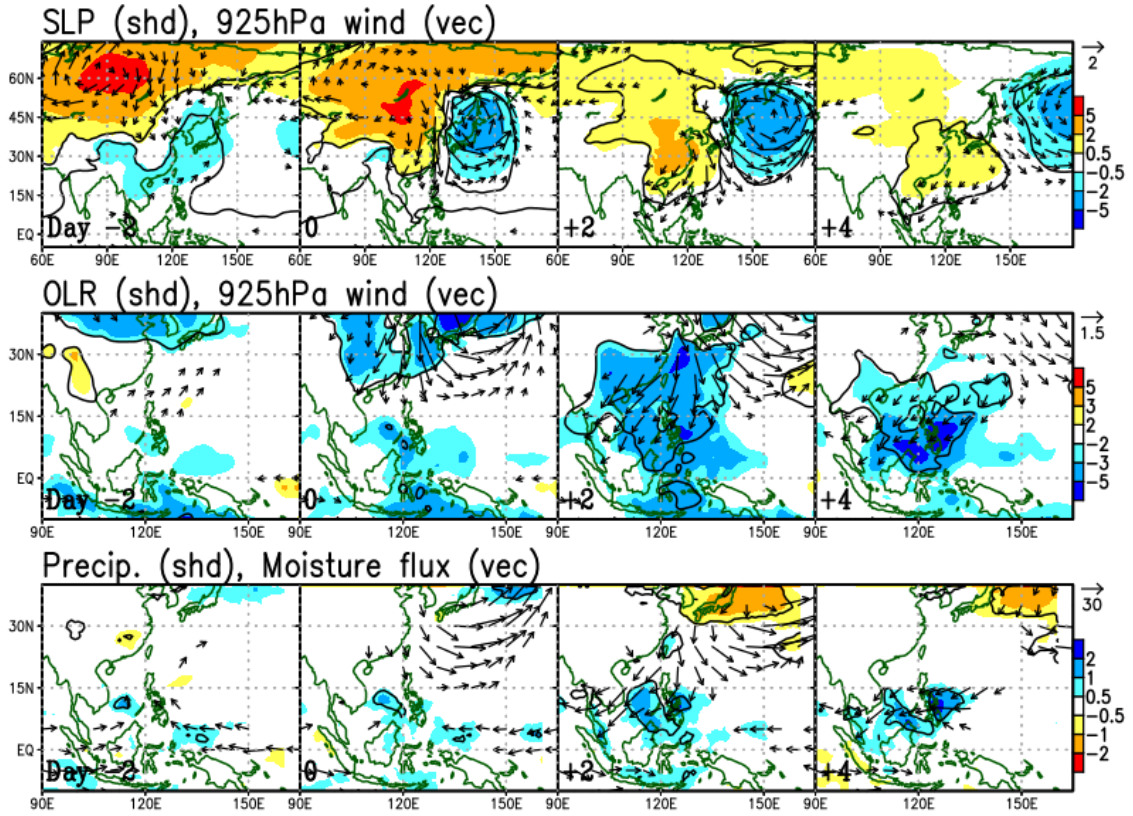


Figure 6.1 Mean temporal evolution of W-CAO event (day -2 to +4) shown by several parameters regressed with W-CAO index. Top panels show mean sea level pressure (SLP; shaded) and low-level wind field at 925 hPa (arrow) anomalies over large part of East Asia. Middle panels show OLR (shaded) and the wind field (arrow) anomalies over and around the Maritime Continent. Bottom panels show precipitation (shaded) and moisture fluxes (arrow) anomalies. The moisture flux is obtained from column integration over 1000-200 hPa. The scales are shown in the right side of panels. The physical units are: hPa (SLP), m $s^{-1}$ (wind), W $m^{-2}$ (OLR), mm $day^{-1}$ (precipitation), and kg m $s^{-1}$ (moisture flux). Black contour lines indicate statistically significant areas at 99% confidence level.

## 6.4 **Level 1 clustering: different pathways at midlatitude**

The precipitation responses in Figure 6.1 appear to be statistically significant; however the responses seem weak in amplitude and limited in area. Some previous studies have shown that the impact of cold surges can be greater and cover a larger part of the Maritime Continent (e.g., reaching southern South China Sea), although their cold surges definitions are on the basis of subtropical indices (e.g., Chang et al. 2005). We are curious whether such large response can be produced by the new isentropic CAO index.

Investigation on each independent CAO event is required to explore the variation in precipitation response. We detect 84 CAO events over 1979-2013 period and 45 CAO events over 1997-2013 period. Cross examination between all events finds that only a portion of CAOs exhibited large response in precipitation, whereas the rest of events showed weak or no response

in precipitation. This indicates that there is significant inhomogeneity or variability between tropical responses to CAO events.

Why is there inhomogeneity on the CAO impact? We hypothesize that it is related to differences in CAO pathways. The CAO event is defined based on mass flux at 45°N latitude (Chapter 2.1.3). Due to this remote distance between CAO region and the tropical Maritime Continent, the CAO pathways are likely affected by current synoptic conditions over East Asia and the Maritime Continent that enhance/block the northerly flows and thus modify the precipitation response. Therefore, it is important to discover the distinct pathways of CAO for identifying various precipitation responses to CAO.

In the lagged regression Figure 6.1(top), the CAO induces large equatorward flow anomalies from midlatitude East Asia. After the CAO event (day +2), a portion of equatorward flow appears to keep moving to the tropics (northerly surge) and the other portion seems to turn eastward into the North Pacific Ocean (westerly surge). The cross examination among individual CAO events finds that some CAO events showed stronger northerly surge, and the others showed stronger westerly surge. To classify CAO events that developed to northerly surge and westerly surge, we perform simple clustering on the basis of some given criteria. Steps for clustering are shown as following.

1. Two new surge indices are defined: northerly index (NI) and westerly index (WI) index. NI is meridional wind at 850 hPa averaged over 30°N,120°-135°E, and WI is zonal wind at 850 hPa averaged over 30°-45°N, 135°E (Figure 6.2(left)). The surge indices are calculated for each CAO event one day after its local maximum (day +1). A distribution of NI and WI is shown in Figure 6.2(right).
2. To classify CAO events, we define a separation line. The separation line is a northwest-southeast oriented diagonal line that is drawn from a point where the winter climatologies of NI and WI are met (Figure 6.2(right)).
3. We cluster CAO events into two types: CAO(NS) and CAO(WS). CAO(NS) is CAO event that developed to northerly surge. It is defined when the CAO is located on the left/bottom side of separation line. Whereas CAO(WS) is CAO event that developed to westerly surge. Any CAOs that appear on the right/top side of separation line are defined as CAO(WS).

A total of 57 out of 84 events (68%) are categorized as CAO(NS), and a total of 27 events (32%) are CAO(WS) during the long period of 1979-2013. While during short period of 1997-2013, there are 31 out of 45 (69%) CAO(NS) and 14 (31%) CAO(WS) events. Lagged

composite analysis is conducted on each CAO group to study the synoptic evolution. On one hand, Figure 6.3 shows composite anomalies during the evolution of CAO(NS). The synoptic pattern over the midlatitude is quite similar with the regression analysis, but with the stronger southward expansion of Siberian High. The northerly anomalies over the subtropics and tropics are more vivid and organized. In South China Sea, the northerly develops to northeasterly and reaches some regions over equatorial line such as Borneo, Peninsular Malaysia, Singapore, and Sumatra Island of Indonesia. The moisture flux enhancement is stronger than before and results in grater and wider convective areas, which cover a larger part of South China Sea. On the other hand, Figure 6.4 shows composite anomalies during the evolution of CAO(WS). The northerlies south of 45°N are barely shown because most of mass fluxes turn eastward toward the ocean, which cause an absence of northerly surge over the subtropics and tropics. Consequently, the moisture influx is not affected, and tropical precipitation does not develop. Despite the difference in study period, the patterns of OLR and precipitation are quite similar to each other in both CAO composites.

These results indicate that the classification into two different types, CAO(NS) and CAO(WS), successfully separates CAO events that cause active precipitation and inactive precipitation response. Why is the equatorward flow not maintained in case of CAO(WS)? It is associated with synoptic conditions where Siberian High does not expand to the south (Figure 6.4). CAO(WS) is primarily controlled by enhanced negative pressure anomalies located over the East Asian coast/Northwestern Pacific, which causes large eastward tendency following the cyclonic development. The appearance of negative pressure may be related to the development of explosive cyclones over the Northwest Pacific.

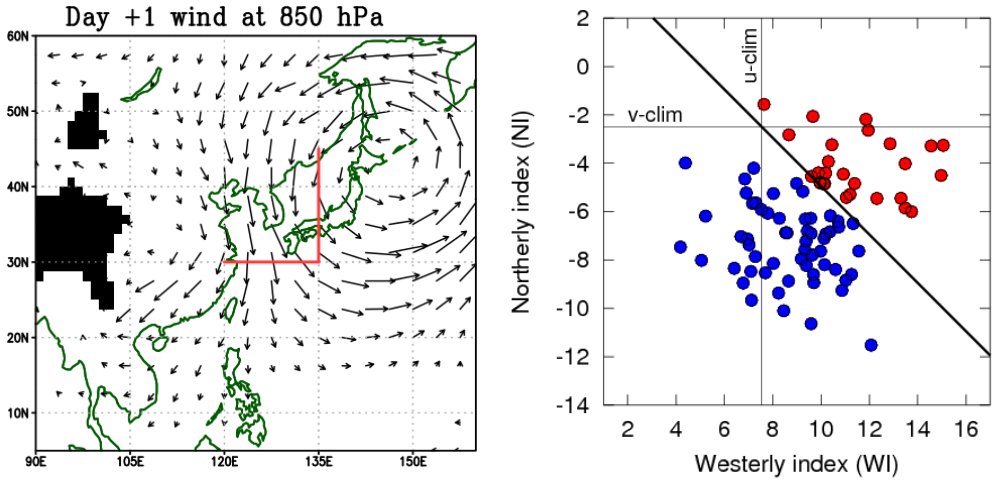


Figure 6.2 (Left) Red lines indicate regions for calculating northerly index (NI) (30°N,120°-135°E) and westerly index (WI) (30-45N, 135E). (Right) Distribution of CAO events as function of WI and NI. The climatology of northerly and westerly winds (horizontal black line and vertical black line) and a separation line (diagonal black line) are shown. See text for details.

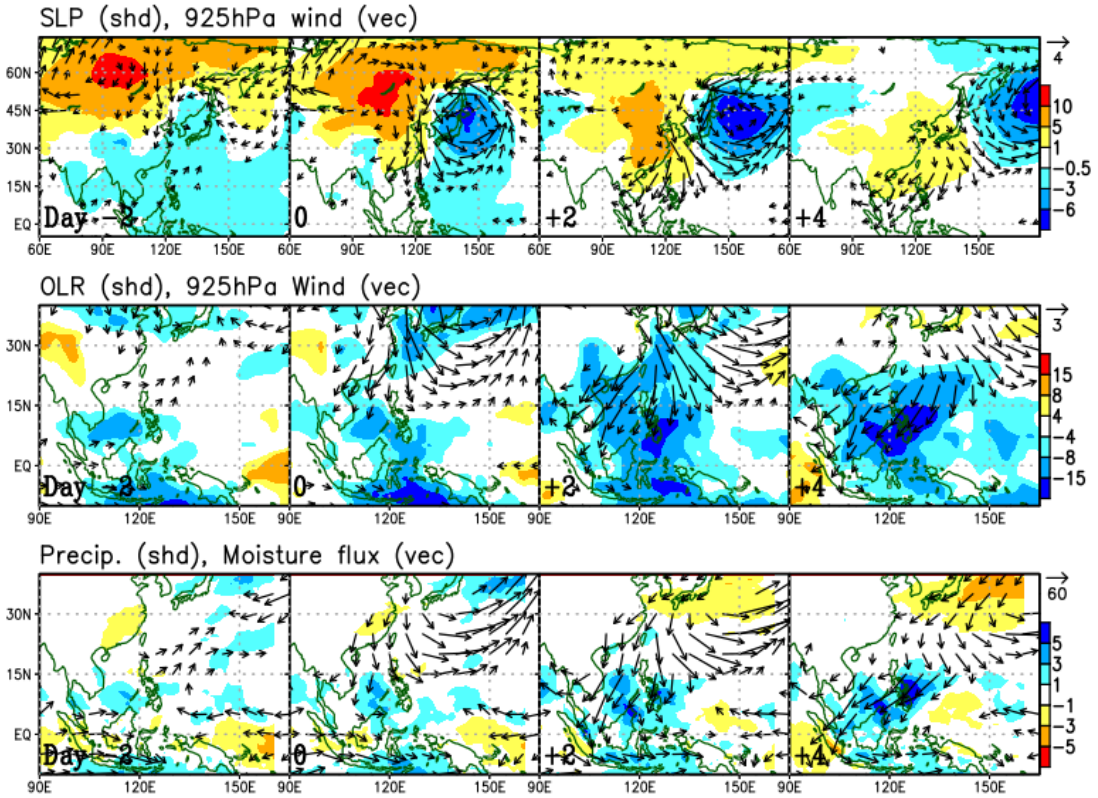


Figure 6.3 Composite evolution of CAO(NS) group. Figure description is same with Fig. 6.1, except scales of contours and arrows.

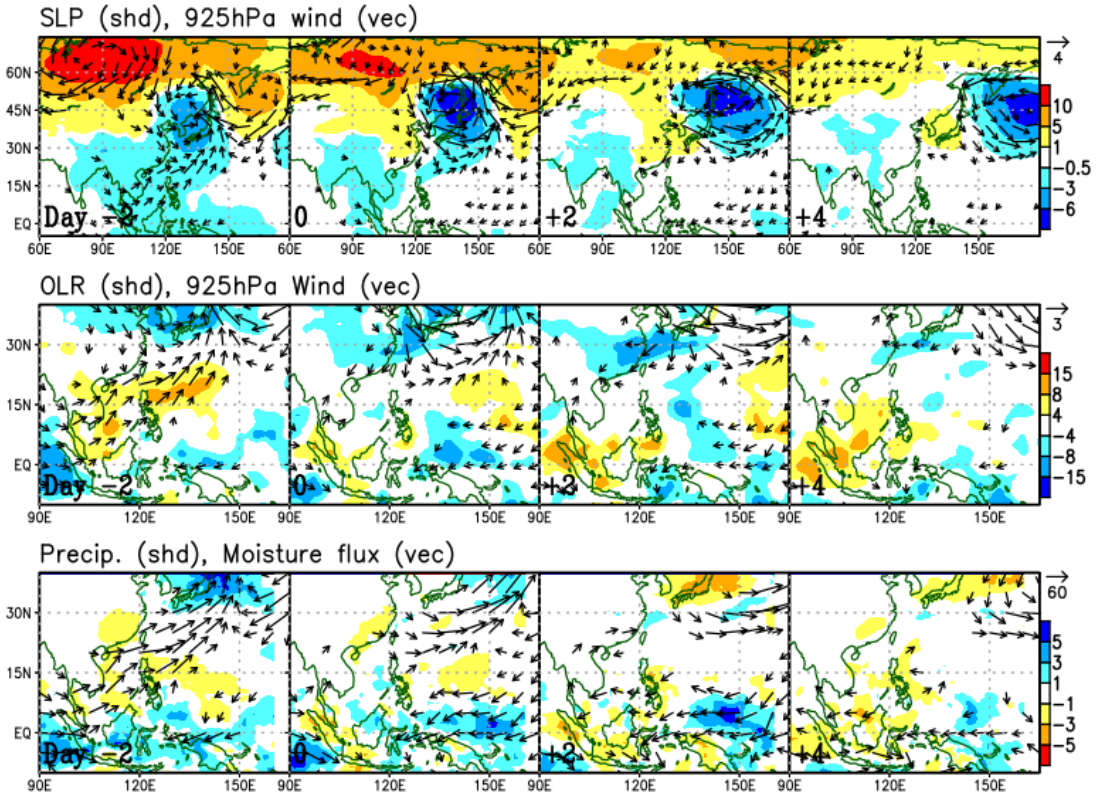


Figure 6.4 Composite evolution of CAO(WS) group. Figure description is same with Fig. 6.1, except scales of contours and arrows.

## 6.5 **Level 2 clustering: different pathways at the subtropics**

Some studies documented that northerly surges in East Asia can split to or choose different pathways over the subtropical regions. Two northerly surge types were previously identified: South China Sea (SCS) type and Philippines Sea (PHS) type (e.g. ,Compo et al. 1999). The variability of surge pathway over the subtropics motivates us to perform an additional clustering applied to CAO(NS) group. To do that, at first we define two new surge criteria:

SCS surge: if $v_{after} < v_0$ and $|v_{after}| \geq |u_{after}|$ at (15°N, 110°-117.5°E),

PHS surge: if $v_{after} < v_0$ and $|v_{after}| \geq |u_{after}|$ at (15°N, 122.5°-130°E).

$v_0$ denotes 925-hPa meridional wind at day 0 relative to peak of CAO event in midlatitude. $v_{after}$ and $u_{after}$ are meridional and zonal wind at a day when the strongest meridional wind is observed within day +2 to +4 relative to peak of CAO event. The condition $v_{after} < v_0$ simply means that the northerly wind over the designated regions must gain more momentum after the

CAO event. $|v_{after}| \geq |u_{after}|$ is used to ensure that the northerly component is stronger than the zonal component. The difference between SCS surge and PHS surge criteria is only in their region. By using the new criteria, we introduce four additional CAO types derived from CAO(NS):

1. SCS-type: CAO(NS) that satisfied SCS surge condition but not PHS surge condition.
2. PHS-type: CAO(NS) that satisfied PHS surge condition but not SCS surge condition.
3. Both-type: CAO(NS) that satisfied both SCS surge and PHS surge conditions.
4. Blocked-type: CAO(NS) that did not satisfy any condition.

The number of events categorized into each type is shown in Figure 6.5. Out of 57 cases, there are 20 SCS-type, 5 PHS-type, 8 both-type, and 24 blocked-type during the long period of 1979-2013. And for the short period of 1997-2013, out of 31 cases, there are 10 SCS-type, 2 PHS-type, 4 both-type, and 15 blocked-type. The blocked-type seems majority. We will propose some mechanisms for each type.

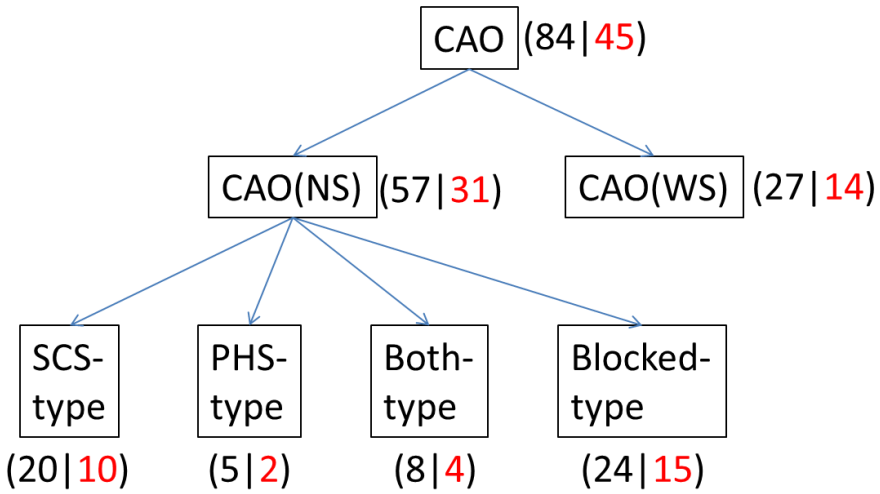


Figure 6.5 Tree diagram of CAO clustering from identified W-CAO events. The first clustering yields two different types: CAO(NS) and CAO(WS) types. The second clustering that is applied to CAO(NS) type results in four different sub-types: SCS-type, PHS-type, both-type, and blocked-type. The black and red values indicate number of CAO events in each group identified during the period of 1979-2013 and period of 1997-2013, respectively.

Figure 6.6 shows the evolution of SCS-type. The synoptic patterns in SCS-type are similar to those in the composite of all CAO(NS) but with greater responses. The expansion of Siberian High to tropical region is evident. The northerlies gradually evolve into northeasterlies and the flow becomes more perpendicular to the Philippines Archipelago and some lands over

southern South China Sea. The convection and precipitation responses are greater especially over the Philippines, north of Borneo, Peninsular Malaysia, Singapore, and Sumatra. The precipitation is mainly developed by terrain-induced mechanism where the enhanced moisture fluxes are forcedly lifted up due to topography. This is a typical impact of northerly surge over the South China Sea (Lim et al. 2017). The characteristic and impact of SCS-type are schematically shown in Figure 6.10a.

Figure 6.7 presents the evolution of PHS-type. The magnitude of anomalies in PHS-type is relatively larger than that in other types possibly due to small number of samples. PHS-type is accompanied by a dipole-like structure of pressure anomalies over the Maritime Continent. The western Maritime Continent shows high anomalies and the eastern shows low anomalies. Due to this condition, the northerlies are confined over the Philippines Sea. The anomalous northerlies confluence with a pre-existing cyclonic low east of Philippines and appears to develop a strong cyclonic convergence. It then causes large precipitation response over the northwestern Pacific. The large scale dipole pattern of pressure is also evident in OLR and precipitation patterns. This dipole is associated with a particular phase of MJO (explained later in Chapter 6.6). The pre-existing cyclonic low may be related to tropical easterly wave which is consistent with synoptic pattern of PHS-like surge shown in Compo et al. (1999). Figure 6.10b shows schematic characteristic of PHS-type.

Figure 6.8 shows the evolution of both-type. One of interesting feature is that both-type is accompanied by large scale anomalous convergence over the tropical regions. During the course of CAO evolution, the Maritime Continent exhibits negative OLR anomalies. The large scale convergence enables clear propagation of northerlies in both pathways over SCS and PHS. The large scale feature of convergence is related to active phase of MJO over the Maritime Continent (explained later in Chapter 6.6). Furthermore, the intrusion of northerlies appears to amplify precipitation anomalies especially over the northern Maritime Continent. The findings of SCS-type and both-type show the interactions between CAO impact and large scale tropical variability. Figure 6.10b shows schematic characteristic of PHS-type.

Finally Figure 6.9 shows the evolution when CAO does not develop to SCS surge or PHS surge (blocked-type). The blocked-type shows that the Siberian High is not expanding to the SCS and this condition causes a development of easterly surge around 15°N. The easterly flow affects precipitation anomalies over the Philippines, northern SCS, and Indochina region. While the regions over the equatorial line are relatively dry. From all 24 blocked-type CAO, we identify several reasons for the “blocking” of northerlies in the subtropics. The blocking can occur when there is synoptic scale cyclonic disturbance or anticyclonic disturbance over the

northern Maritime Continent (Figure 6.10d). The cyclonic disturbance appears to be the majority, and therefore mainly accounts for composite analysis in Figure 6.9.

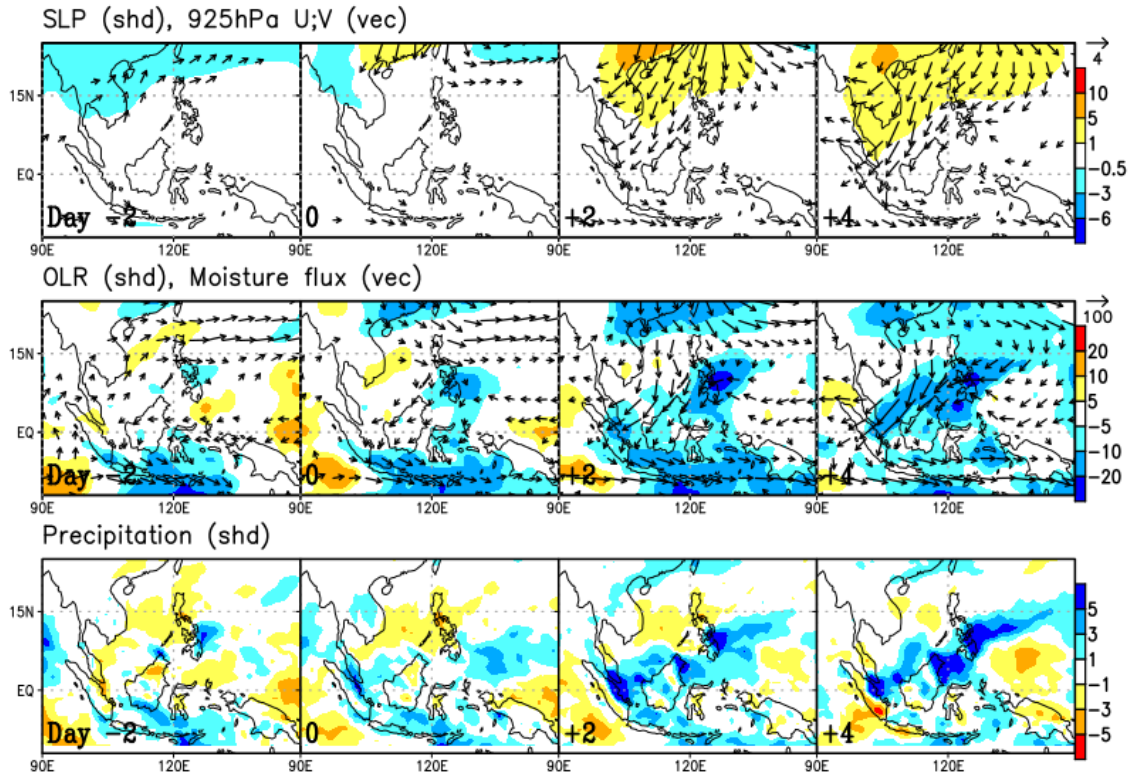


Figure 6.6 Composite evolution of SCS-type group. The temporal evolution (day -2 to +4) is shown composite anomalies. Top panels show mean sea level pressure (SLP; shaded) and low-level wind field at 925 hPa (arrow) anomalies over and around the Maritime Continent. Middle panels show OLR (shaded) and moisture fluxes (arrow) anomalies. Bottom panels show precipitation (shaded). The scales are shown in the right side of panels.

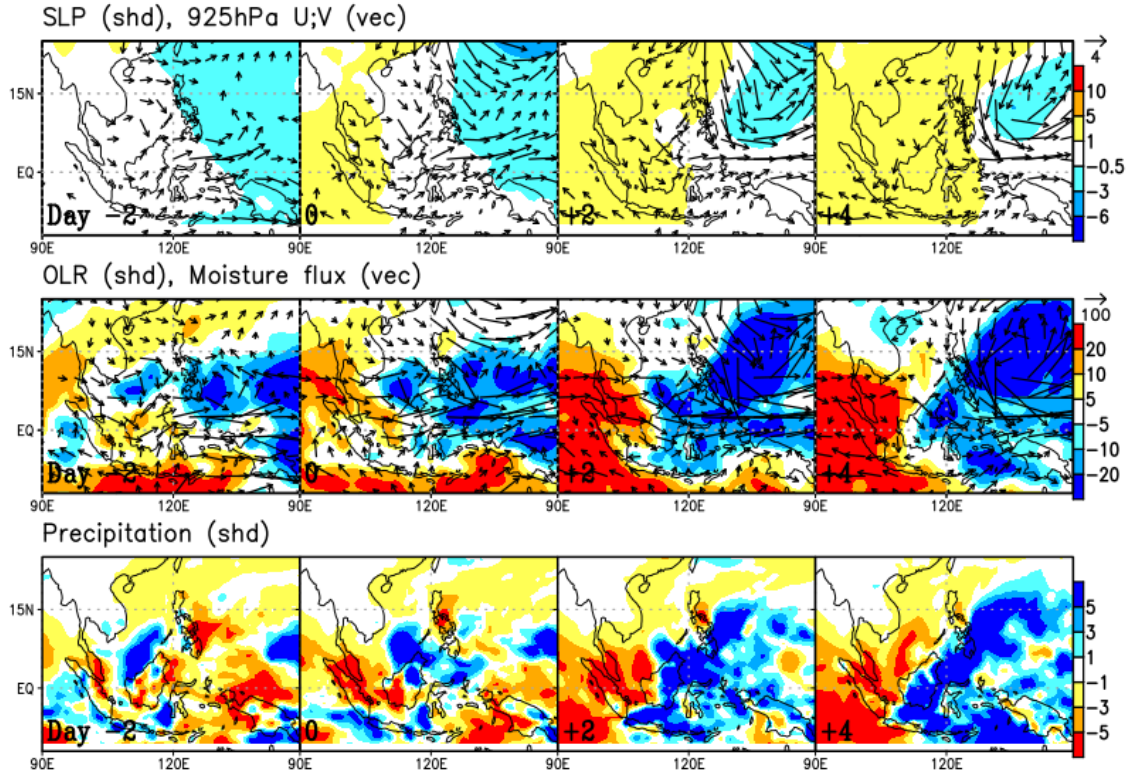


Figure 6.7 Composite evolution of PHS-type group. Figure description is same with Fig. 6.6.

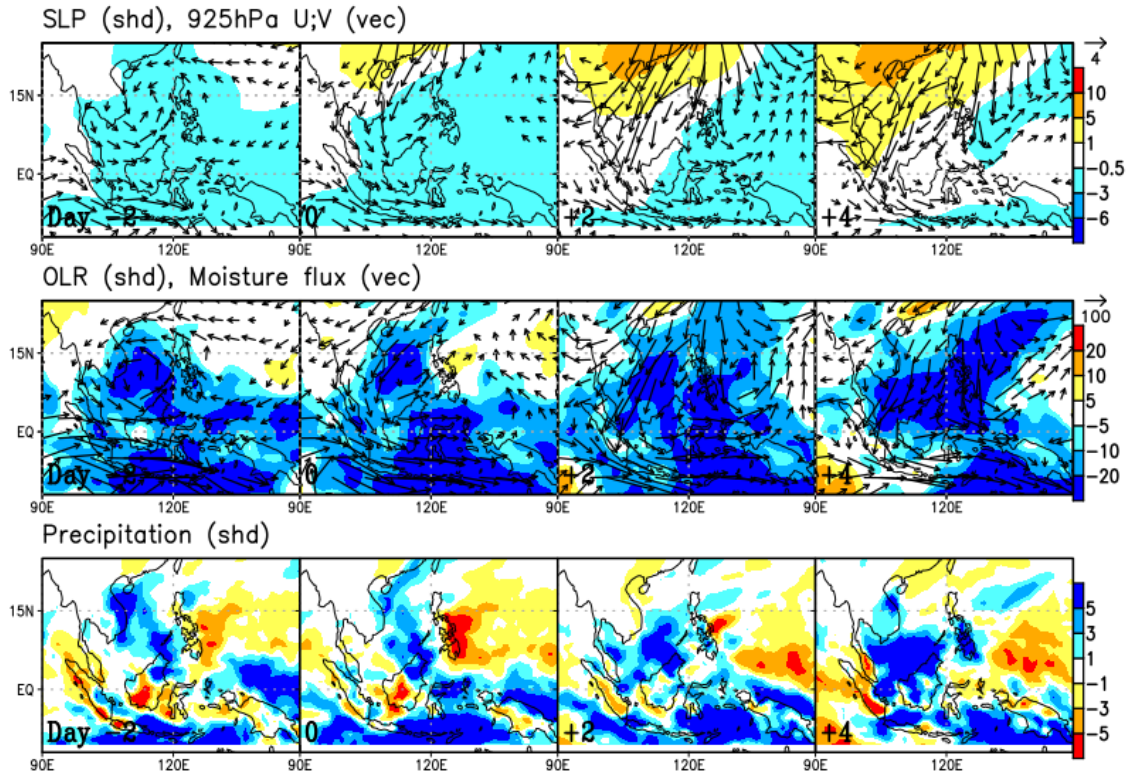


Figure 6.8 Composite evolution of both-type group. Figure description is same with Fig. 6.6.

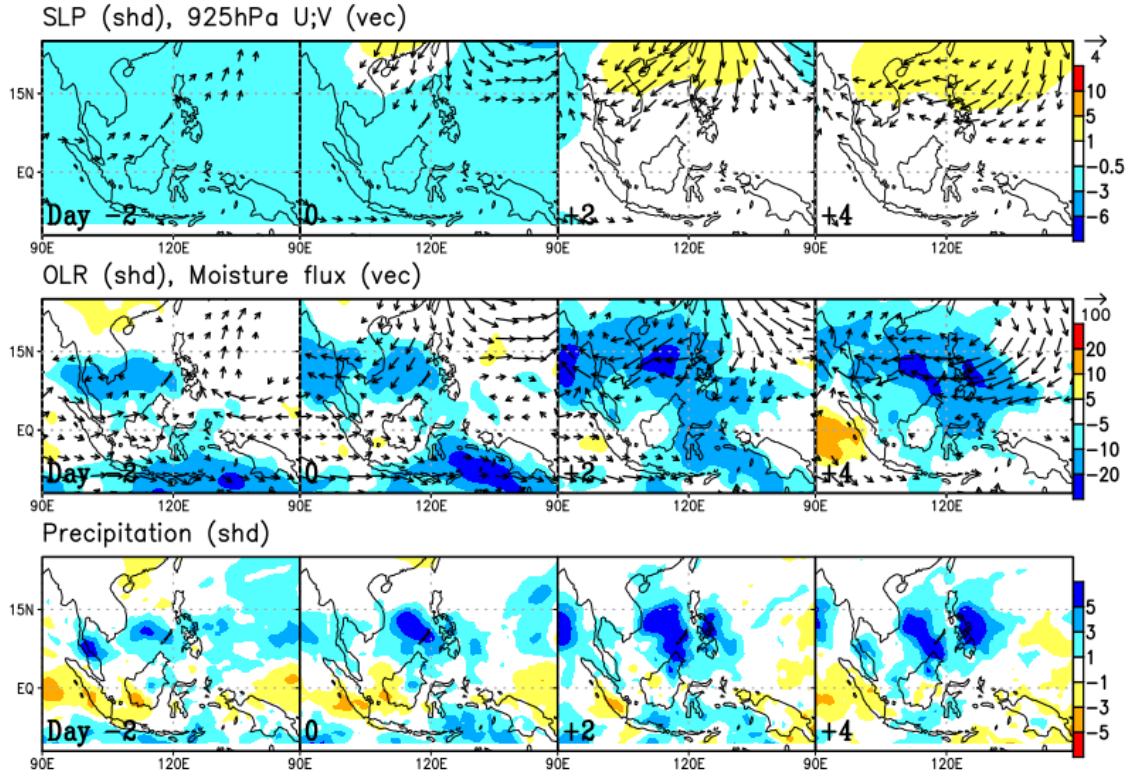


Figure 6.9 Composite evolution of blocked-type group. Figure description is same with Fig. 6.6.

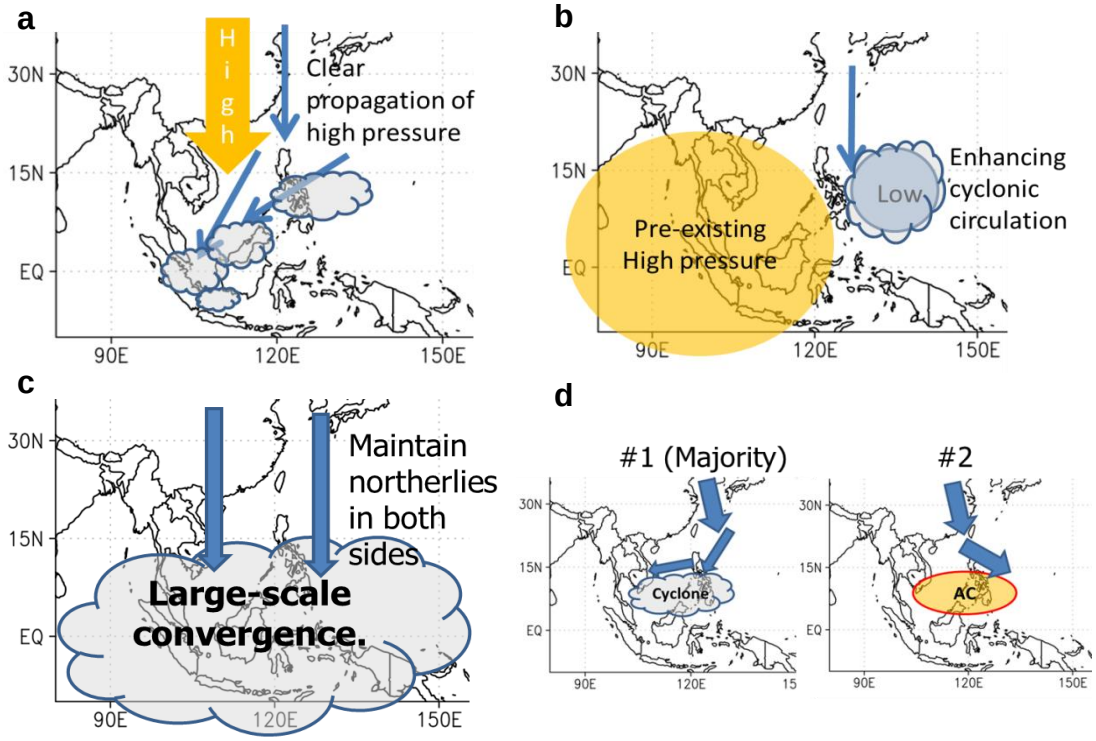


Figure 6.10 Schematic representations of four sub-types of CAO(NS) events: (a) SCS-type, (b) PHS-type, (c) both-type, and (d) blocked-type. See text for explanation.

## 6.6 **Sensitivity to MJO phases**

Composite anomalies of PHS-type and both-type indicate possible roles of large scale tropical variability associated with MJO. Figure 6.11 shows longitude-time diagrams of tropical OLR (averaged at 15°S-15°N) for each CAO type. PHS-type clearly exhibits dipole pattern of MJO where there is wet phase of MJO over the western Pacific and dry phase of MJO over the Indian Ocean around day 0. This condition blocks northerly development over the SCS and results in northerly surge over the PHS. For both-type, it shows strong propagation of wet phase of MJO crossing over the Maritime Continent around day 0. The active MJO over the Maritime Continent provides large scale atmospheric background that maintains northerlies over SCS and PHS. The OLR signals in SCS-type and blocked-type are quite small and unlikely important for controlling the CAO impact.

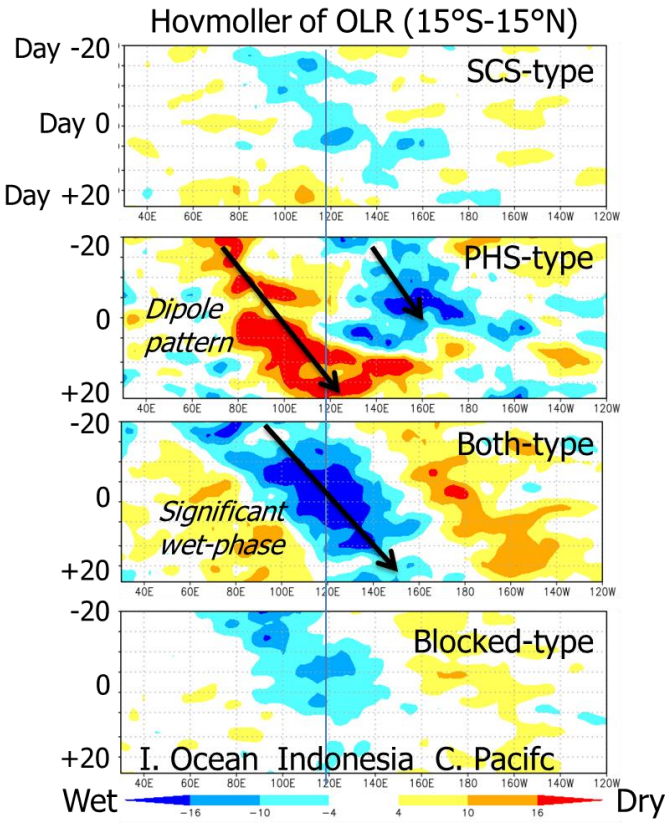


Figure 6.11 Composite of tropical OLR anomalies (averaged over 15°S-15°N) in four CAO types. From top to bottom, the panels show SCS-type, PHS-type, both-type, and blocked-type.

## 6.7 **Conclusion**

This chapter documents the impact of western CAO along with its case-by-case variability over the tropical region. The regression analysis does show significant signature of the mean precipitation response to CAO, but there is inhomogeneity among individual CAO cases. The clustering analyses find distinct pathways of CAO, which consequently result in different precipitation response. In the midlatitude, the CAO can develop to northerly surge (CAO(NS)) or westerly surge (CAO(WS)). This difference in midlatitude pathways is controlled by current synoptic condition in the extratropics that is related to the intrusion of Siberian High. CAO(NS) obviously causes greater impact over the tropics, whereas there is no positive signal of precipitation during CAO(WS). Furthermore, during the course of its propagation, CAO(NS) can be divided into four additional types owing to the synoptic conditions over the tropical regions. They are SCS-type, PHS-type, both-type, and blocked-type. SCS-type shows a typical pattern of northerly surge over the South China Sea and causes precipitation induced by the topography. PHS-type is associated with dipole pressure pattern over the tropics and leads to cyclonic convergence over the northwestern Pacific. Both-type is controlled by large scale convergence associated with MJO; the northerlies amplify MJO-precipitation. Blocked-type occurs when there is blocking caused by synoptic scale cyclonic/anticyclonic disturbances over the northern Maritime Continent.

Although there is a difference in period of study due to data availability, the precipitation composites for CAO occurred in 1997-2013 exhibit similar patterns with OLR composites for CAO in 1979-2013. This indicates that the clustering method is reliable to depict consistent patterns regardless the period of study. We further confirm the consistency by comparing circulation patterns in those two different periods, which show a higher degree of similarity than those in precipitation-OLR (not shown).

This chapter improves our understanding on the variability of CAO impact. We identify several CAO pathways that vary according to the current synoptic condition in both the tropics and extratropics. The differences in pathways consequently cause differences in the impact of CAO, particularly the precipitation response. For CAO monitoring, these results suggest to add more criteria for CAO event in addition to the CAO magnitude, which can benefit for weather forecast over the tropical regions.

# 7. General conclusion

## 7.1 **Key findings**

This thesis investigates relationships between tropical variability and polar cold air mass (PCAM)/cold air outbreak (CAO). Several key findings are listed as following points.

- *Tropical variability influences PCAM/CAO:*
    1. ENSO plays a strong role on the interannual variability of total PCAM amount in the Northern Hemisphere. El Niño decreases total PCAM amount by decreasing the residence time of PCAM over North America and inducing cold air outflows over the central North Pacific (Chapter 3).
    2. Two primary modes of East Asian stream are discovered: western CAO and eastern CAO. Both CAOs are associated with ENSO, but with opposite responses. The western CAO is enhanced during La Nina, while the eastern CAO is induced during El Niño. ENSO affects East Asian CAOs through planetary Rossby wave train excited by tropical convections over the Maritime Continent and central Pacific (Chapter 4).
    3. MJO controls intraseasonal variability of CAO events in East Asia. On one hand, the western CAO is induced by wet MJO over the Maritime Continent. On the other hand, the eastern CAO is induced by wet MJO over the western Pacific and dry MJO over the Indian Ocean (Chapter 5).
- *CAO influences tropical variability:*
    4. The western CAO causes significant impact over the tropical regions. The intrusion of strong northerlies and enhancement of moisture influx induce precipitation development over the Maritime Continent. The impact varies depending on the downstream pathways of CAO that are controlled by associated synoptic conditions (Chapter 6).

The results improve our understanding on tropical-extratropical interactions. We anticipate that the findings on tropical precursors are helpful for mid- and long-range PCAM/CAO forecasts. And the identified CAO impacts are crucial for weather forecasters over the tropical regions.

## 7.2 Discussion and future work

We note several things related to this study. First, we utilizes the isentropic diagnosis on the basis of 280 K threshold. One may consider using other thresholds depending on the interest of study. For example, Shimada et al. (2018) used 296 K to depict summertime cool air. Second, the boundary between genesis box and loss box in the two-box framework model of PCAM is simplified to be constant at 45°N (Kanno et al. 2015b). We can improve the two-box model representation by designing a zonally asymmetric boundary that follows the actual geographical pattern of boundary between genesis and loss region (see Figure 2.2c). Third, the synoptic scale CAO events are mainly driven by extratropical waves and the tropical forcing serves as supporting driver. Due to different time scale, ENSO and MJO cannot predict the timing of CAO events, but they still can affect the average frequency of CAO events over a given period. Fourth, the impacts of CAOs to tropical weather are quite variable. The separations by simple clusterings have identified several dominant modes of CAO pathways that result in different response in precipitation. However, the criteria for clustering should be reviewed to affirm the consistency of physical patterns associated with CAO pathways.

Many potential future works have been mentioned in the last section of Chapters 3, 4, 5, and 6. Some interesting ideas are related to case studies. For example, it is necessary to assess the influence of tropical convection when both effects of MJO and ENSO are taking into account. Relating to the CAO events, it would be interesting to study a special case (if any) where there is significant influence of MJO to midlatitude CAO, and then the CAO gives feedback to the MJO through equatorward flow. Finally, the precipitation responses associated with CAO impact can be studied in details by performing numerical simulation using high-resolution regional weather model.

# Appendix A: List of Abbreviations/Acronyms

| | | |
|---|---|---|
| AC | : | Anticyclone |
| BPF | : | Band pass filter |
| CAO | : | Cold air outbreak |
| CAO(NS) | : | CAO that develops to northerly surge |
| CAO(WS) | : | CAO that develops to westerly surge |
| CAOI | : | CAO index |
| CP | : | Central Pacific |
| DJF | : | December-January-February |
| E-CAO | : | Eastern CAO in East Asia |
| EA | : | East Asia |
| ENSO | : | El Niño-Southern Oscillation |
| EOF | : | Empirical Orthogonal Function |
| ETD | : | Extratropical direct cell |
| GCM | : | Global climate model |
| HPF | : | High pass filter |
| IO | : | Indian Ocean |
| LBM | : | Linear baroclinic model |
| LPF | : | Low pass filter |
| MC | : | Maritime Continent |
| MJO | : | Madden-Julian Oscillation |
| NA | : | North America |
| NS | : | Northerly surge |
| OLR | : | Outgoing longwave radiation |
| PCAM | : | Polar cold air mass |
| PNA | : | Pacific-North American |
| PHS | : | Philippines Sea |
| SAT | : | Surface air temperature at 2 m |
| SCS | : | South China Sea |
| SLP/MSLP | : | Mean sea level pressure |
| SST | : | Sea surface temperature |
| T2m | : | *see* SAT |
| Total PCAM | : | Total hemispheric PCAM amount |
| W-CAO | : | Western CAO in East Asia |
| WP | : | Western Pacific |
| WS | : | Westerly surge |

# References


Abdillah, M. R., Y. Kanno, and T. Iwasaki, 2017: Tropical–Extratropical Interactions Associated with East Asian Cold Air Outbreaks. Part I: Interannual Variability. *J. Clim.*, **30**, 2989–3007, doi:10.1175/JCLI-D-16-0152.1.

——, ——, and ——, 2018a: Strong Linkage of El Niño-Southern Oscillation to the Polar Cold Air Mass in the Northern Hemisphere. *Geophys. Res. Lett.*, **45**, 5643–5652, doi:10.1029/2018GL077612.

——, ——, and ——, 2018b: Tropical–Extratropical Interactions Associated with East Asian Cold Air Outbreaks. Part II: Intraseasonal Variation. *J. Clim.*, **31**, 473–490, doi:10.1175/JCLI-D-17-0147.1.

Adler, R. F., and Coauthors, 2003: The Version-2 Global Precipitation Climatology Project (GPCP) Monthly Precipitation Analysis (1979–Present). *J. Hydrometeorol.*, **4**, 1147–1167, doi:10.1175/1525-7541(2003)004<1147:TVGPCP>2.0.CO;2.

Alexander, M. A., I. Bladé, M. Newman, J. R. Lanzante, N. C. Lau, and J. D. Scott, 2002: The atmospheric bridge: The influence of ENSO teleconnections on air-sea interaction over the global oceans. *J. Clim.*, **15**, 2205–2231, doi:10.1175/1520-0442(2002)015<2205:TABTIO>2.0.CO;2.

Barrett, B. S., G. R. Henderson, and J. S. Werling, 2015: The Influence of the MJO on the intraseasonal variability of Northern Hemisphere spring snow depth. *J. Clim.*, **28**, 7250–7262, doi:10.1175/JCLI-D-15-0092.1.

Beccario, C., 2018: Earth :: a global map of wind, weather, and ocean conditions. https://earth.nullschool.net/ (Accessed June 8, 2018).

Bjerknes, J., 1969: ATMOSPHERIC TELECONNECTIONS FROM THE EQUATORIAL PACIFIC 1. *Mon. Weather Rev.*, **97**, 163–172, doi:10.1175/1520-0493(1969)097<0163:ATFTEP>2.3.CO;2.

Brönnimann, S., 2007: Impact of El Niño-Southern Oscillation on European climate. *Rev. Geophys.*, **45**, RG3003, doi:10.1029/2006RG000199.

Cellitti, M. P., J. E. Walsh, R. M. Rauber, and D. H. Portis, 2006: Extreme cold air outbreaks over the United States, the polar vortex, and the large-scale circulation. *J. Geophys. Res. Atmos.*, **111**, 1–14, doi:10.1029/2005JD006273.

Chang, C.-P., J. E. Erickson, and K. M. Lau, 1979: Northeasterly Cold Surges and Near-Equatorial Disturbances over the Winter MONEX Area during December 1974. Part I: Synoptic Aspects. *Mon. Weather Rev.*, **107**, 812–829, doi:10.1175/1520-0493(1979)107<0812:NCSANE>2.0.CO;2.

Chang, C.-P., P. A. Harr, and H.-J. Chen, 2005: Synoptic Disturbances over the Equatorial South China Sea and Western Maritime Continent during Boreal Winter. *Mon. Weather Rev.*, **133**, 489–503, doi:10.1175/MWR-2868.1.

Chang, C. P., Z. Wang, and H. Hendon, 2006: The Asian Winter Monsoon. *The Asian Monsoon*, Springer Press, 89–127.

Compo, G. P., G. N. Kiladis, and P. J. Webster, 1999: The horizontal and vertical structure of east Asian winter monsoon pressure surges. *Q. J. R. Meteorol. Soc.*, **125**, 29–54, doi:10.1002/qj.49712555304.

Diaz, H. F., M. P. Hoerling, and J. K. Eischeid, 2001: Enso variability, teleconnections and climate change. *Int. J. Climatol.*, **21**, 1845–1862, doi:10.1002/joc.631.

Duchon, C. E., 1979: Lanczos Filtering in One and Two Dimensions. *J. Appl. Meteorol.*, **18**, 1016–1022, doi:10.1175/1520-0450(1979)018<1016:LFIOAT>2.0.CO;2.

Efron, B., and R. J. Tibshirani, 1993: *An Introduction to the Bootstrap*. Chapman & Hall/CRC,.

Feng, J., P. Liu, W. Chen, and X. Wang, 2015: Contrasting Madden-Julian Oscillation activity during various stages of EP and CP El Niños. *Atmos. Sci. Lett.*, **16**, 32–37, doi:10.1002/asl2.516.

Garreaud, R. D., 2001: Subtropical cold surges: Regional aspects and global distribution. *Int. J. Climatol.*, **21**, 1181–1197, doi:10.1002/joc.687.

Gill, A. E., 1980: Some simple solutions for heat- induced tropical circulation. *Q. J. R. Meteorol. Soc.*, **106**, 447–462.

Gong, D.-Y., S.-W. Wang, and J.-H. Zhu, 2001: East Asian Winter Monsoon and Arctic Oscillation. *Geophys. Res. Lett.*, **28**, 2073–2076, doi:10.1029/2000GL012311.

He, J., H. Lin, and Z. Wu, 2011: Another look at influences of the Madden-Julian Oscillation on the wintertime East Asian weather. *J. Geophys. Res.*, **116**, D03109, doi:10.1029/2010JD014787.

Hoerling, M. P., a Kumar, and M. Zhong, 1997: El Nino, La Nina, and the nonlinearity of their teleconnections. *J. Clim.*, **10**, 1769–1786, doi:10.1175/1520-0442(1997)010<1769:ENOLNA>2.0.CO;2.

Holmes, O., 2016: Deaths in Japan and Taiwan as record cold snap hits east Asia. *Guard.*,. http://www.theguardian.com/world/2016/jan/25/deaths-japan-taiwan-snow-ice-chaos-asia (Accessed July 8, 2018).

Horel, J. D., and J. M. Wallace, 1981: Planetary-Scale Atmospheric Phenomena Associated with the Southern Oscillation. *Mon. Weather Rev.*, **109**, 813–829, doi:10.1175/1520-0493(1981)109<0813:PSAPAW>2.0.CO;2.

Hoskins, B. J., and D. J. Karoly, 1981: The Steady Linear Response of a Spherical Atmosphere to Thermal and Orographic Forcing. *J. Atmos. Sci.*, **38**, 1179–1196, doi:10.1175/1520-0469(1981)038<1179:TSLROA>2.0.CO;2.

IPCC, 2013: *Climate Change 2013: The Physical Science Basis.* Intergovernmental Panel on Climate Change, Ed. Cambridge University Press, Cambridge, 1535 pp.

Iwasaki, T., and Y. Mochizuki, 2012: Mass-Weighted Isentropic Zonal Mean Equatorward Flow in the Northern Hemispheric Winter. *SOLA*, **8**, 115–118, doi:10.2151/sola.2012-029.

——, T. Shoji, Y. Kanno, M. Sawada, M. Ujiie, and K. Takaya, 2014: Isentropic Analysis of Polar Cold Airmass Streams in the Northern Hemispheric Winter. *J. Atmos. Sci.*, **71**, 2230–2243, doi:10.1175/JAS-D-13-058.1.

Jeong, J.-H., C.-H. Ho, B.-M. Kim, and W.-T. Kwon, 2005: Influence of the Madden-Julian Oscillation on wintertime surface air temperature and cold surges in east Asia. *J. Geophys. Res.*, **110**, D11104, doi:10.1029/2004JD005408.

Jin, F., and B. J. Hoskins, 1995: The Direct Response to Tropical Heating in a Baroclinic Atmosphere. *J. Atmos. Sci.*, **52**, 307–319, doi:10.1175/1520-0469(1995)052<0307:TDRTTH>2.0.CO;2.

Kahl, J. D., M. C. Serreze, and R. C. Schnell, 1992: Tropospheric low-level temperature inversions in the Canadian arctic. *Atmos. - Ocean*, **30**, 511–529, doi:10.1080/07055900.1992.9649453.

Kanno, Y., M. R. Abdillah, and T. Iwasaki, 2015a: Charge and discharge of polar cold air mass in northern hemispheric winter. *Geophys. Res. Lett.*, **42**, doi:10.1002/2015GL065626.

——, T. Shoji, and T. Iwasaki, 2015b: Comparison study of the polar cold air mass between Northern and

Southern Hemispheric winters based on a zonal-mean two-box model. *Atmos. Sci. Lett.*, **16**, 70–76, doi:10.1002/asl2.522.

——, M. R. Abdillah, and T. Iwasaki, 2016: Long-term trend of cold air mass amount below a designated potential temperature in Northern and Southern Hemispheric winters using reanalysis data sets. *J. Geophys. Res. Atmos.*, **121**, 10,138-10,152, doi:10.1002/2015JD024635.

——, J. E. Walsh, and T. Iwasaki, 2017: Interannual Variability of the North American Cold Air Stream and Associated Synoptic Circulations. *J. Clim.*, **30**, 9575–9590, doi:10.1175/JCLI-D-17-0104.1.

Klein, S. a, B. J. Soden, and N. C. Lau, 1999: Remote Sea Surface Temperature Variations during ENSO: Evidence for a Tropical\nAtmospheric Bridge. *J. Clim.*, **12**, 917–932, doi:10.1175/1520-0442(1999)012<0917:RSSTVD>2.0.CO;2.

Kobayashi, S., and Coauthors, 2015: The JRA-55 Reanalysis : General Specifications and Basic Characteristics. *J. Meteorol. Soc. Japan*, doi:10.2151/jmsj.2015-001.

L'Heureux, M. L., and Coauthors, 2017: Observing and predicting the 2015/16 El Niño. *Bull. Am. Meteorol. Soc.*, **98**, 1363–1382, doi:10.1175/BAMS-D-16-0009.1.

Lau, N.-C., and M. J. Nath, 1996: The Role of the "Atmospheric Bridge" in Linking Tropical Pacific ENSO Events to Extratropical SST Anomalies. *J. Clim.*, **9**, 2036–2057, doi:10.1175/1520-0442(1996)009<2036:TROTBI>2.0.CO;2.

Lau, N. C., and M. J. Nath, 2003: Atmosphere-ocean variations in the Indo-Pacific sector during ENSO episodes. *J. Clim.*, **16**, 3–20, doi:10.1175/1520-0442(2003)016<0003:AOVITI>2.0.CO;2.

Li, W., W. Guo, P. Hsu, and Y. Xue, 2016: Influence of the Madden–Julian oscillation on Tibetan Plateau snow cover at the intraseasonal time-scale. *Sci. Rep.*, **6**, 30456, doi:10.1038/srep30456.

Liebmann, B., and C. a. Smith, 1996: Description of a complete (interpolated) outgoing longwave radiation datasets. *Bull. Amer. Meteor. Soc.*, **77**, 1275–1277.

Lim, S. Y., C. Marzin, P. Xavier, C.-P. Chang, and B. Timbal, 2017: Impacts of Boreal Winter Monsoon Cold Surges and the Interaction with MJO on Southeast Asia Rainfall. *J. Clim.*, **30**, 4267–4281, doi:10.1175/JCLI-D-16-0546.1.

Lin, H., G. Brunet, and R. Mo, 2010: Impact of the Madden–Julian Oscillation on Wintertime Precipitation in Canada. *Mon. Weather Rev.*, **138**, 3822–3839, doi:10.1175/2010MWR3363.1.

Linkin, M. E., and S. Nigam, 2008: The North Pacific Oscillation–West Pacific Teleconnection Pattern: Mature-Phase Structure and Winter Impacts. *J. Clim.*, **21**, 1979–1997, doi:10.1175/2007JCLI2048.1.

Livezey, R. E., and W. Y. Chen, 1983: Statistical Field Significance and its Determination by Monte Carlo Techniques. *Mon. Weather Rev.*, **111**, 46–59, doi:10.1175/1520-0493(1983)111<0046:SFSAID>2.0.CO;2.

Lorenz, E. N., 1967: *The Nature and Theory of the general circulation of the atmosphere*. World Meteorological Organization, 74-78 pp.

Madden, R. A., and P. R. Julian, 1971: Detection of a 40–50 Day Oscillation in the Zonal Wind in the Tropical Pacific. *J. Atmos. Sci.*, **28**, 702–708, doi:10.1175/1520-0469(1971)028<0702:DOADOI>2.0.CO;2.

Mailler, S., and F. Lott, 2010: Equatorial Mountain Torques and Cold Surge Preconditioning. *J. Atmos. Sci.*, **67**, 2101–2120, doi:10.1175/2010JAS3382.1.

Matthews, A. J., B. J. Hoskins, and M. Masutani, 2004: The global response to tropical heating in the Madden-Julian oscillation during the northern winter. *Q. J. R. Meteorol. Soc.*, **130**, 1991–2011, doi:10.1256/qj.02.123.

Moon, J., B. Wang, and K. Ha, 2011: ENSO regulation of MJO teleconnection. *Clim. Dyn.*, **37**, 1133–1149, doi:10.1007/s00382-010-0902-3.

Overland, J. E., J. M. Adams, and N. A. Bond, 1999: Decadal Variability of the Aleutian Low and Its Relation to High-Latitude Circulation*. *J. Clim.*, **12**, 1542–1548, doi:10.1175/1520-0442(1999)012<1542:DVOTAL>2.0.CO;2.

Rayner, N. A., D. E. Parker, E. B. Horton, C. K. Folland, L. V. Alexander, D. P. Rowell, E. C. Kent, and A. Kaplan, 2003: Global analyses of sea surface temperature, sea ice, and night marine air temperature since the late nineteenth century. *J. Geophys. Res.*, **108**, 4407, doi:10.1029/2002JD002670.

Saha, K., 2010: *Tropical circulation systems and monsoons*. Springer Berlin Heidelberg, 1-324 pp.

Sardeshmukh, P. D., and B. J. Hoskins, 1988: The Generation of Global Rotational Flow by Steady Idealized Tropical Divergence. *J. Atmos. Sci.*, **45**, 1228–1251, doi:10.1175/1520-0469(1988)045<1228:TGOGRF>2.0.CO;2.

Screen, J. A., and I. Simmonds, 2010: The central role of diminishing sea ice in recent Arctic temperature amplification. *Nature*, **464**, 1334–1337, doi:10.1038/nature09051.

Seager, R., N. Harnik, Y. Kushnir, W. Robinson, and J. Miller, 2003: Mechanisms of hemispherically symmetric climate variability. *J. Clim.*, **16**, 2960–2978, doi:10.1175/1520-0442(2003)016<2960:MOHSCV>2.0.CO;2.

Seager, R., N. Harnik, W. a. Robinson, Y. Kushnir, M. Ting, H.-P. Huang, and J. Velez, 2005: Mechanisms of ENSO-forcing of hemispherically symmetric precipitation variability. *Q. J. R. Meteorol. Soc.*, **131**, 1501–1527, doi:10.1256/qj.04.96.

Seo, K.-H., and S.-W. Son, 2012: The Global Atmospheric Circulation Response to Tropical Diabatic Heating Associated with the Madden–Julian Oscillation during Northern Winter. *J. Atmos. Sci.*, **69**, 79–96, doi:10.1175/2011JAS3686.1.

Shimada, T., Y. Kanno, and T. Iwasaki, 2018: Low-level cool air over the midlatitude oceans in summer. *J. Clim.*, **31**, 2075–2090, doi:10.1175/JCLI-D-17-0188.1.

Shoji, T., Y. Kanno, T. Iwasaki, and K. Takaya, 2014: An Isentropic Analysis of the Temporal Evolution of East Asian Cold Air Outbreaks. *J. Clim.*, **27**, 9337–9348, doi:10.1175/JCLI-D-14-00307.1.

Takaya, K., and H. Nakamura, 2001: A Formulation of a Phase-Independent Wave-Activity Flux for Stationary and Migratory Quasigeostrophic Eddies on a Zonally Varying Basic Flow. *J. Atmos. Sci.*, 608–627.

Tangang, F. T., L. Juneng, E. Salimun, P. N. Vinayachandran, Y. K. Seng, C. J. C. Reason, S. K. Behera, and T. Yasunari, 2008: On the roles of the northeast cold surge, the Borneo vortex, the Madden-Julian Oscillation, and the Indian Ocean Dipole during the extreme 2006/2007 flood in southern Peninsular Malaysia. *Geophys. Res. Lett.*, **35**, L14S07, doi:10.1029/2008GL033429.

Thompson, D. W. J., and J. M. Wallace, 1998: The Arctic oscillation signature in the wintertime geopotential height and temperature fields. *Geophys. Res. Lett.*, **25**, 1297–1300, doi:10.1029/98GL00950.

Trenberth, K. E., 1997: The Definition of El Niño. *Bull. Am. Meteorol. Soc.*, **78**, 2771–2777, doi:10.1175/1520-0477(1997)078<2771:TDOENO>2.0.CO;2.

Trenberth, K. E., G. W. Branstator, D. Karoly, A. Kumar, N.-C. Lau, and C. Ropelewski, 1998: Progress during TOGA in understanding and modeling global teleconnections associated with tropical sea surface temperatures. *J. Geophys. Res.*, **103**, 14291, doi:10.1029/97JC01444.

Trilaksono, N. J., S. Otsuka, and S. Yoden, 2012: A Time-Lagged Ensemble Simulation on the

Modulation of Precipitation over West Java in January–February 2007. *Mon. Weather Rev.*, **140**, 601–616, doi:10.1175/MWR-D-11-00094.1.

Vecchi, G. a., and N. A. Bond, 2004: The Madden-Julian Oscillation (MJO) and northern high latitude wintertime surface air temperatures. *Geophys. Res. Lett.*, **31**, L04104, doi:10.1029/2003GL018645.

Vitart, F., and F. Molteni, 2010: Simulation of the Madden- Julian Oscillation and its teleconnections in the ECMWF forecast system. *Q. J. R. Meteorol. Soc.*, **136**, 842–855, doi:10.1002/qj.623.

Walker, G. T., and E. W. Bliss, 1932: World Weather V - NAO. *Mem. R. Meteorol. Soc.*, **IV**, 54–84, doi:10.1002/qj.49705422601.

Wallace, J. M., and D. S. Gutzler, 1981: Teleconnections in the Geopotential Height Field during the Northern Hemisphere Winter. *Mon. Weather Rev.*, **109**, 784–812, doi:10.1175/1520-0493(1981)109<0784:TITGHF>2.0.CO;2.

Wang, B., R. Wu, and X. Fu, 2000: Pacific–East Asian Teleconnection: How Does ENSO Affect East Asian Climate? *J. Clim.*, **13**, 1517–1536, doi:10.1175/1520-0442(2000)013<1517:PEATHD>2.0.CO;2.

——, Z. Wu, C.-P. Chang, J. Liu, J. Li, and T. Zhou, 2010: Another Look at Interannual-to-Interdecadal Variations of the East Asian Winter Monsoon: The Northern and Southern Temperature Modes. *J. Clim.*, **23**, 1495–1512, doi:10.1175/2009JCLI3243.1.

Wang, C., 2004: ENSO, Atlantic Climate Variability, and the Walker and Hadley Circulations. *The Hadley Circulation: Present, Past and Future*, 173–202.

Wang, L., R. Huang, L. Gu, W. Chen, and L. Kang, 2009: Interdecadal Variations of the East Asian Winter Monsoon and Their Association with Quasi-Stationary Planetary Wave Activity. *J. Clim.*, **22**, 4860–4872, doi:10.1175/2009JCLI2973.1.

Watanabe, M., and M. Kimoto, 2000: Atmosphere-ocean thermal coupling in the North Atlantic : A positive feedback. *Q. J. R. Meteorol. Soc.*, **126**, 3343–3369, doi:10.1002/qj.49712657017.

——, and F.-F. Jin, 2003: A Moist Linear Baroclinic Model: Coupled Dynamical–Convective Response to El Niño. *J. Clim.*, **16**, 1121–1139, doi:10.1175/1520-0442(2003)16<1121:AMLBMC>2.0.CO;2.

Wheeler, M. C., and H. H. Hendon, 2004: An All-Season Real-Time Multivariate MJO Index: Development of an Index for Monitoring and Prediction. *Mon. Weather Rev.*, **132**, 1917–1932, doi:10.1175/1520-0493(2004)132<1917:AARMMI>2.0.CO;2.

Xie, P., and P. A. Arkin, 1998: Global monthly precipitation estimates from satellite-observed outgoing longwave radiation. *J. Clim.*, **11**, 137–164, doi:10.1175/1520-0442(1998)011<0137:GMPEFS>2.0.CO;2.

Yamazaki, A., M. Honda, and A. Kuwano-Yoshida, 2015: Heavy Snowfall in Kanto and on the Pacific Ocean Side of Northern Japan Associated with Western Pacific Blocking. *Sola*, **11**, 59–64, doi:10.2151/sola.2015-013.

Zhang, Y., K. R. Sperber, and J. S. Boyle, 1997: Climatology and Interannual Variation of the East Asian Winter Monsoon: Results from the 1979–95 NCEP/NCAR Reanalysis. *Mon. Weather Rev.*, **125**, 2605–2619, doi:10.1175/1520-0493(1997)125<2605:CAIVOT>2.0.CO;2.

Zheng, J., Q. Liu, C. Wang, and X.-T. Zheng, 2013: Impact of Heating Anomalies Associated with Rainfall Variations over the Indo-Western Pacific on Asian Atmospheric Circulation in Winter. *Clim. Dyn.*, **40**, 2023–2033, doi:10.1007/s00382-012-1478-x.